REPORT R-435 SEPTEMBER 1969

CSL COORDINATED SCIENCE LABORATORY

A STUDY OF EFFECTS OF THE GAS-SURFACE INTERACTION ON SPINNING CONVEX BODIES WITH APPLICATION TO SATELLITE EXPERIMENTS

GERALD RAY KARR

UNIVERSITY OF ILLINOIS - URBANA, ILLINOIS

A STUDY OF EFFECTS OF THE GAS-SURFACE INTERACTION ON SPINNING CONVEX BODIES WITH APPLICATION TO SATELLITE EXPERIMENTS

BY

Gerald Ray Karr
Coordinated Science Laboratory
University of Illinois
Urbana, Illinois

This work was supported in part by the Joint Services Electronics Program (U.S. Army, U.S. Navy, and U.S. Air Force) under Contract DAAB 07-67-C-0199; and in part by NAS 8-21442.

A STUDY OF EFFECTS OF THE GAS-SURFACE INTERACTION ON SPINNING CONVEX BODIES WITH APPLICATION TO SATELLITE EXPERIMENTS

BY

GERALD RAY KARR
B.S., University of Illinois, 1964
M.S., University of Illinois, 1966

THESIS

Submitted in partial fulfillment of the requirements
for the degree of Doctor of Philsophy in Aeronautical and
Astronautical Engineering
in the Graduate College of the
University of Illinois, 1969

Urbana, Illinois

A STUDY OF EFFECTS OF THE GAS-SURFACE INTERACTION ON SPINNING CONVEX BODIES WITH APPLICATION TO SATELLITE EXPERIMENTS

Gerald Ray Karr, Ph.D.
Department of Aeronautical and Astronautical Engineering
University of Illinois, 1969

Abstract

In rarefied gas flow problems there are two effects which influence the flow; (1) collisions of gas molecules with other gas molecules, and (2) collisions of gas molecules with solid surfaces (the gas-surface interaction). This study deals with free molecular flow in which the effect of gas-gas collision can be neglected and the gas-surface interaction has the dominate influence on the flow. The results of this study have application to satellites since free molecular flow conditions occur at orbital altitudes above 120 km.

Knowledge of the gas-surface interaction is required in order to determine the aerodynamic properties of satellites. At satellite velocities (7-8 km/sec) the interaction of neutral atmospheric gas molecules with the satellite surface occurs at energies in the 1 to 10 ev range. It is just this energy range which has not been satisfactorily duplicated in the laboratory; therefore, at present, laboratory gas-surface interaction data can not be applied directly to the determination of the aerodynamic properties of satellites. It is proposed in this study that satellite experiments be performed to obtain the needed information from measurements of the aerodynamic properties of satellites. In order to interpret the satellite data,

a generalized gas-surface interaction model was developed and used in the analysis of this study.

Gas-surface interaction models such as those of Maxwell, Schamberg, and Nocilla, contain two or more parameters which may be adjusted to cover a certain range of possible gas-surface interactions. Although such specific models may be used to develop the aerodynamic equations of satellites, the validity of these models in this application has not been determined. The results of this study show that the proposed generalized model is necessary in the interpretation of measured satellite aerodynamic properties.

In the past, the interpretation of measured satellite aerodynamic properties to obtain information on the gas-surface interaction and orbital gas density has not been successful for two reasons; (1) the uncertainty in the validity of gas-surface interaction models, and (2) insufficient data to allow a determination of the orbital gas density and at least two gas-surface interaction parameters. The results of this study illustrate strongly the feasibility of performing a satellite experiment in which accurate data could be obtained on the gas density and gas-surface interaction parameters by measuring the drag, spin rate slowdown and spin axis precession rate of a spinning convex satellite.

The results of the study on the aerodynamic properties of spinning convex bodies have exhibited a number of interesting effects associated with the spin of the body and the gas-surface interaction. For example, the drag and lift of a spinning body was found to be greater than that of a non-spinning body. It was also found that there exists a spin induced lateral lift force which is analogous to the Magnus effect but is opposite in direction.

In addition, spin induced aerodynamic torques, perpendicular to the spin axis, are significant on bodies at angles of attack to the flow.

The gas-surface interaction was found to have a strong influence in determining the aerodynamic properties of both spinning and non-spinning bodies. Both analytical and numerical results were obtained for the aerodynamic properties of four basic body shapes (disk, cylinder, cone, and sphere) to study the effects of spin, angle of attack, and the gas-surface interaction.

ACKNOWLEDGMENTS

The author thanks Professor Shee-Mang Yen who, as the principal advisor, has generously contributed his time and wisdom in the preparation of this dissertation and Professor Howard W. Knoebel who, with Professor Yen, was directly responsible for the able direction of this study.

Since June of 1968, this study has been performed under a contract with the NASA George Marshall Space Flight Center. The author is deeply indebted to Mr. James O. Ballance of NASA for his active support of this work.

The author thanks those who have provided encouragement and guidance through discussions; Dr. Kenneth Moe, Dr. James L. Myers, Jr., Dr. Franklin M. Propst, and Dr. Wallace W. Youngblood.

The author thanks Richard Flood who did the computer programming in the numerical studies, Arnold Z. Cohen who gathered information on past satellites and the atmospheric environment, and Nicki Stillings who carefully typed this manuscript.

The author takes pleasure in thanking his wife, Laurel, for her encouragement and her many sacrifices.

TABLE OF CONTENTS

Page

Page

1. INTRODUCTION

In the free molecular flow regime, intermolecular collisions may be neglected and the gas-surface interaction then becomes the dominating influence in this flow regime. For earth satellites, free molecular conditions exist at all altitudes above 100 mi (161 km.).[1] It is therefore essential that the effect of the gas-surface interaction be considered in the determination of the aerodynamic properties of satellites.

At satellite velocities, the gas molecules of the atmosphere impinge on the satellite surface at velocities in the order of 7 to 8 km/sec. Taking into account the molecular weight of the molecules composing the atmosphere, the interaction energy associated with satellite velocities is in the range of 1 to 10 ev. Laboratory experiments using molecular beam techniques have not been successful in duplicating these interaction energies.[2] Therefore, the character of the gas-surface interaction at satellite velocities and thus the effect of the interaction on satellite aerodynamic properties has not been determined. It has been possible to construct models of the gas-surface interaction from physical principles and experimental results obtained for interaction energies less than 1 ev. Such models contain two or more parameters which may be adjusted to include a certain range of possible interaction. It has not been determined, however, how well these models approximate the actual gas-surface interaction that occurs in the satellite environment.

The fact that aerodynamic properties of bodies in a free molecular flow depend on the gas-surface interaction suggests that measurements of

satellite aerodynamic properties could yield information on the gas-surface interaction. However, measurements of satellite aerodynamic drag have been inconclusive in determining information on the gas-surface interaction for two reasons; 1) uncertainties in the satellite environment; primarily, uncertainty in the atmospheric density and 2) uncertainties in the aerodynamic properties of satellites and, thus, in the interpretation of the measurements. Drag measurements really only determine the product of density and drag coefficients since neither is known separately.

The problems with interpreting drag measurements suggest that an additional aerodynamic property of a satellite should be measured, such as the slowdown rate of a spinning satellite, which, when combined with the drag measurement of that satellite, would provide a means of separating the effects of density and drag coefficient or gas-surface interaction. Analyses of this type have been performed on drag and spin rate decay data for paddle-wheel shaped satellites, from which estimates of the density and a gas-surface interaction parameter were obtained.[3,4] These results are, however, subject to uncertainties which are much the same as those associated with drag measurements. First, since the measurements of drag and slowdown rate were a function of at least three unknowns (orbital gas density and two or more gas-surface interaction parameters), a value for at least one of the unknowns had to be assumed in order to obtain estimates of the other two. Secondly, since the validity of any particular model of the gas-surface interaction has not been established, the interpretation of measurements may be made, as in References 2 and 3, using a number of different models.

Since each model used produces a different estimate of density, the experiment is able to determine only a possible range on the density.

The first point made above suggests that additional aerodynamic properties should be measured in order to remove the necessity to make assumptions which can introduce errors in the interpretation of the measurements. There are six aerodynamic properties to be considered corresponding to three components of force and three components of torque acting on a satellite; however, the properties must not only be measurable but must also be independent functions of the quantities to be determined. The free molecular aerodynamic properties (drag, lift, and torque) of non-spinning bodies are known to depend on the angle of attack of the body and the gas-surface interaction (see for example References 5 and 6). For non-spinning satellites, however, the effects of lift and torque properties cannot be easily assessed because the orientation of the satellite with respect to the flow is usually unknown and probably random. Spinning satellites, on the other hand, maintain relatively fixed orientations in space. If the orientation of the spin axis of the satellite is known, it is possible to determine the angle of attack on the satellite with respect to the flow at any position in the orbit. This suggests, then, that the aerodynamic properties of spinning satellites may provide the measurables needed for determining the gas density and gas-surface interaction parameters.

Past studies of the free molecular aerodynamic properties of spinning bodies do not, however, provide a sufficient basis for proposing a satellite experiment such as suggested above. The analysis of aerodynamic torque on spinning satellites is usually made on an approximate basis

considering only the moments of drag forces about the center of mass of the satellite (see for example References 7, 8) which, in general, do not give a complete understanding of the influence of the gas-surface interaction. More exact analyses of the aerodynamic torques have been made in References 9, 10, and 11 for the case of a spinning spherical satellite in which it was found that the aerodynamic torque properties are strongly dependent upon a single parameter of a specific gas-surface interaction model.

The objective of this study is to analyze more fully the influence of the gas-surface interaction on the aerodynamic properties of spinning bodies and to propose satellite experiments to accurately determine the gas density and the gas-surface interaction.

In order to remove uncertainties introduced by a variety of possible gas-surface interaction models that can be used in such a study and satellite experiments (second point made above), a generalized gas-surface interaction model is developed which is designed to cover a wider range of possible gas-surface interactions than models currently being used. The generalized model contains currently accepted models as subclasses and has the additional advantage of being able to incorporate laboratory results and models which may be suggested in the future. The description of this generalized model is given in chapter 2.

In chapter 3, the generalized model is used to develop the equations expressing the aerodynamic properties of spinning and non-spinning bodies in a free molecular flow. The results obtained may be interpreted in terms of any of the gas-surface interaction models contained as subclasses in the general model. The aerodynamic equations are developed in

a general manner which makes them applicable to bodies of various shapes.

In chapter 4, results are obtained for a disk (or flat plate), cylinder, cone, and sphere for arbitrary angles of attack and for both the spinning and non-spinning cases. These results reveal the strong influence of the gas-surface interaction on the aerodynamic properties of spinning bodies.

In chapter 5, the aerodynamic properties of spinning satellites is studied to determine the importance of the gas-surface interaction on the average aerodynamic properties of satellites. These results suggest possibilities for performing satellite experiments. The random tumbling problem is also studied in this chapter.

In chapter 6, satellite experiments are proposed and the feasibility of performing these experiments is investigated by assessing the possible accuracy and the magnitude of measurable quantities needed to determine the unknowns of atmospheric density and gas-surface interaction parameters.

The feasibility of the proposed satellite experiment is enhanced by results obtained in a study performed by the Coordinated Science Laboratory pertaining to the measurement of satellite precession rates which could be caused by a general relativity effect. This study determined that extremely accurate measurements of even small precession rates are possible by using a completely passive optical readout technique utilizing observations of sunlights reflected by the satellite surface.[12,13] On this basis then, it is proposed that for certain satellite shapes there are at least three measurable aerodynamic properties (drag, slowdown torque, and

precession torque) which can be utilized to determine more precisely the atmospheric density and the character of the gas-surface interaction at satellite velocities.

2. A GENERALIZED GAS-SURFACE INTERACTION MODEL

Insufficient information is available at present to warrant choosing a specific gas-surface interaction model to represent the reflection of molecules which impinge a surface at satellite velocities. For this reason, a generalized gas-surface interaction model is developed such that it contains various possible gas-surface interaction models or subclasses including the models of Maxwell, Nocilla[14], and Schamberg[15].

The generalized model will be used in the development of equations to express the aerodynamic properties of spinning bodies in subsequent chapters. The resulting equations have the advantage that they can then be interpreted in terms of any of the gas-surface interaction models contained as subclasses of the general model.

2.1. A Generalized Model for the Interaction

Consider a stream of mono-energetic, uni-directional neutral gas molecules impinging upon a solid surface at an angle of θ with respect to the plane of the surface (see Figure 2.1). Also consider that the molecules are all reflected in a beam which is axial symmetric about an axis which makes an angle θ_j with respect to surface, in the plane formed by the impinging molecules and the surface normal (see Figure 2.1). The subscript, j, on θ_j may take on values of 1,2,3---to represent cases in which the reflection can be modeled as being composed of two or more beams which are axial symmetric about axes which make angles with respect to the surface of θ_1, θ_2, θ_3 - - - - - respectively. The purpose for adding the versatility of

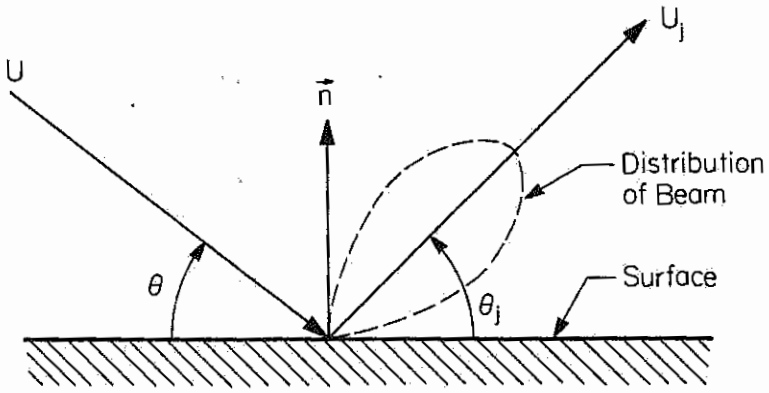

Figure 2.1. Notation used in the generalized model.

of using more than one reflected beam will be illustrated later in this chapter. For the present, however, consider the beam in the θ_j direction.

In order to describe the gas-surface interaction, the following three quantities must be determined about the reflected beam.

1. The velocity.
2. The angle of reflection.
3. The number flux.

The relations of these three quantities with the incident beam properties are described in the following three sections.

2.1.1. Reflected Velocity

In general, the velocity of individual molecules reflected from the surface will be distributed in some arbitrary manner. The distribution of velocities of a large number of reflected molecules could be, for example, Maxwellian, or constant (no distribution), or any one of any numerous possible distributions. For purposes of calculating the force on the surface in free molecular flow, however, the specific distribution of velocities is not important since once the molecules leave the surface they do not again hit the surface, and they do not collide with the impinging molecules.

Only the average velocity of the reflected beam is needed in determining the momentum of reflected molecules and then the force on the surface. Therefore, a vector velocity $\vec{U}_j$ is defined to represent the average velocity of the beam of molecules reflected in the direction θ_j. The velocity $\vec{U}_j$ is also in the direction of θ_j since the beam is assumed to be symmetrical in velocity distribution about the axis at angle θ_j.

In order to relate the magnitude of velocity $\vec{U}_j$ with the magnitude of velocity $\vec{U}$ (velocity of impinging molecules), a parameter α_j is introduced, where

$$U_j = U\sqrt{1-\alpha_j} \tag{2.1}$$

The parameter α_j is defined in this manner to facilitate the reduction of the generalized model parameters to the parameter of other models. Equation 2.1 is equivalent to writing

$$\alpha_j = 1 - \frac{U_j^2}{U^2} \tag{2.2}$$

which is often referred to as the definition of the thermal accommodation coefficient. However, the designation of thermal accommodation coefficient is rather vague and ill defined. The thermal accommodation coefficient, α, is also often defined as

$$\alpha = \frac{T_i - T_r}{T_i - T_w} \tag{2.3}$$

where T_i is the temperature of the incident gas molecules, T_r is the temperature of reflected molecules and T_w is the temperature of the surface (wall). If the temperatures are understood to represent the kinetic temperatures, and if $T_w/T_i \ll 1$ then Equation 2.3 may be written as

$$\alpha \approx 1 - \frac{T_r}{T_i} = 1 - \frac{U_r^2}{U_i^2} \tag{2.4}$$

The right hand side of Equation 2.4 is similar to the definition of α_j in Equation 2.2 except that U_j in Equation 2.2 represents the average velocity in the θ_j direction while the velocity U_r represents the velocity associated

with T_r, the temperature of the reflected molecules. The operation in going from temperature to velocity in Equation 2.4 depends on the distribution function of reflected molecules and also on the definition of temperature. For the purposes of this study, Equation 2.2 will be used without reference to temperature.

2.1.2. Angle of Reflection

The reflection of a beam of molecules from a solid surface was first considered by Maxwell to be analogous to the reflection of light from a surface. He postulated that molecules could be reflected elastically or specularly much as light from a perfect mirror, or the molecules could reflect diffusively as light does from a rough surface (see Figure 2.2). Even though this treatment of the angle of reflection may be elementary, the Maxwell model has found wide applications.

In 1959, R. Schamberg[15] proposed a gas-surface interaction model which allowed for reflections at angles between the limits of specular and diffuse. Schamberg postulated that the angle of reflection should be related to the angle of incidence of the molecular beam. As an example of such a relationship, Schamberg introduced a parameter, υ, defined by

$$\cos \theta_r = (\cos \theta_i)^{\upsilon}; \quad \upsilon \geq 1 \qquad 2.5$$

where θ_r is the angle of the reflected beam of molecules and θ_i is the angle of incidence. In the limits of $\upsilon = 1$ and $\upsilon \to \infty$, the Schamberg model reduces to the cases of specular and diffuse angles of reflection respectively.

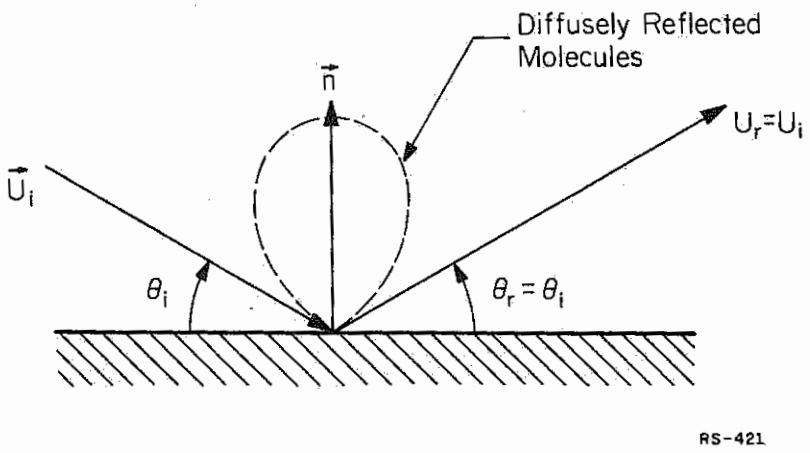

Figure 2.2. Notation used in the Maxwell model.

Although recent experimental results using molecular beam techniques indicate that Equation 2.5 is not in general correct, experimental results do indicate that the angle of reflection is a function of the angle of incidence.(the experimental results will be discussed later in this chapter). In order to include an angle-of-reflection law in the generalized model, consider the functional relationship between the angle of reflection, θ_j, and the angle of incidence, θ, to be in the form of a general polynomial of degree N. That is, let

$$\theta_j = a_j + \sum_{n=1}^{N} (b_j)_n \, \theta^n \qquad 2.6$$

where a_j and $(b_j)_n$: $n = 1,2,\ldots N$ are constant coefficients.

As appropriate experimental results become available, the constants a_j and $(b_j)_n$ can be found by fitting a polynomial to the experimental data. Since appropriate experimental data is not now available, assume, as a first approximation, that the functional relationship for the angle of reflection is linear in θ. That is, let

$$\theta_j = a_j + b_j\theta \qquad 2.7$$

which contains the two unknown constants a_j and b_j. Unless there is a systematic irregularity in the surface, the reflection of a molecule beam which is incident normal to the surface ($\theta = \frac{\pi}{2}$) should also be normal to the surface ($\theta_j = \frac{\pi}{2}$). Using this reasoning, one of the unknown constants in Equation 2.8 can be eliminated to obtain a functional relationship dependent upon only one unknown constant, P_j, where

$$\theta_j = \frac{\pi}{2} P_j + (1-P_j)\, \theta \qquad 2.8$$

This form of the angle-of-reflection law will be used in later chapters to illustrate the effect of angle of reflection on the aerodynamic properties of convex bodies in free molecular flow.

2.1.3. Reflected Number Flux

If a solid surface is neither a source or sink for molecules, the number flux of reflected molecules must equal the number flux of incident molecules. The number flux of incident molecules, $\dot{N}$, is defined as

$$\dot{N} = \frac{\rho}{m} \vec{U}\cdot\vec{n} \qquad 2.9$$

where ρ is the density of the incident gas, $\vec{n}$ is the unit normal to the surface, and $\vec{U}$ is the incident velocity with respect to the surface. If all the molecules were reflected in a single beam, $\dot{N}_{reflected} = \dot{N} = \frac{\rho}{m} \vec{U}\cdot\vec{n}$. For the generalized model, a parameter σ_j, is introduced which relates the number flux reflected in the θ_j beam, $\dot{N}_j$, with the incident number flux. Let

$$\dot{N}_j = \sigma_j \dot{N} = \sigma_j \frac{\rho}{m} \vec{U}\cdot\vec{n} \qquad 2.10$$

For cases when all the incident molecules are reflected in the θ_j direction, $\sigma_j = 1$. For the more general case when the reflection is composed of J symmetric beams having direction $\theta_1, \theta_2, \ldots, \theta_J$,

$$\sum_{j=1}^{J} \sigma_j = 1 \qquad 2.11$$

where J is the number of reflected beams.

2.1.4. Parameters of the Generalized Model

Three separate parameters have been introduced which define the gas-surface interaction in a generalized manner. The average velocity of the reflected molecules is related to the velocity of the incident molecules by the parameter α_j where the magnitude of U_j is given by

$$U_j = U\sqrt{1-\alpha_j} \qquad 2.12$$

The velocity U_j is a vector having direction defined by the angle of reflection θ_j. As a first approximation, θ_j is related to the angle of incidence θ by the parameter P_j given by

$$\theta_j = \frac{\pi}{2} P_j + (1-P_j)\ \theta \qquad 2.13$$

The number flux of molecules reflected in the beam which is symmetrical about the θ_j axis is related to the incident number flux by the parameter σ_j given by

$$m \dot{N}_j = \sigma_j \dot{N} = \sigma_j \rho \vec{U}\cdot\vec{n}$$

where

$$\sum_{j=1}^{J} \sigma_j = 1$$

and where J represents the number of symmetric beams.

2.2. Subclasses of the Generalized Model

For each reflected beam, the parameters σ_j, α_j, and P_j must be specified to determine the force on the surface. By proper choice of these parameters, the generalized model can be reduced to more specific gas-surface

interaction models. This procedure is illustrated in the following three sections for the models of Maxwell, Schamberg, and Nocilla.

2.2.1. Reduction to Maxwell Model

In the Maxwell reflection model, the reflection is divided into two components, specular and diffuse. Define

$$\alpha_d = \text{fraction of incident molecules which are reflected diffusely} \qquad 2.14$$

$$(1-\alpha_d) = \text{fraction of incident molecules which are reflected specularly} \qquad 2.15$$

The velocity of molecules reflected specularly is defined as being equal to the incident velocity and angle of reflection is equal to the angle of incidence (elastic collision with the surface) (see Figure 2.2). For the diffusely reflected component of the reflection consider the velocity of reflection to be related to the incident velocity by the thermal accommodation coefficient α_T where

$$\alpha_T = \frac{T_i - T_r}{T_i - T_w} \qquad 2.16$$

where T_i, T_r, and T_w are defined as in Equation 2.2.

The Maxwell model is obtained from the generalized model, as follows.

First, consider the specular component of reflection and let this be beam j = 1. Then, let

$$\alpha_1 = 0 \text{ or } U_1 = U$$

$$\sigma_1 = (1-\alpha_d) \qquad 2.17$$

$$\theta_1 = \theta \quad \text{or} \quad P_1 = 0$$

Let the diffusely reflected component of reflection be beam j = 2. Then, let

$$\alpha_2 = \alpha_T \text{ or } U_2 = \sqrt{1-\alpha_T}\, U; \frac{Tw}{T_i} << 1$$

$$\sigma_2 = \alpha_d \qquad 2.18$$

$$\theta_2 = \frac{\pi}{2} \quad \text{or} \quad P_2 = 1$$

The force on a surface, due to the impingement and subsequent reflections of the Maxwell type, is then

$$\vec{F} = \rho\, \vec{U}\cdot\vec{n}\, (\vec{U} - \sigma_1\vec{U}_1 - \sigma_2\vec{U}_2)$$

$$= \rho\, \vec{U}\cdot\vec{n}\, (\vec{U} - (1-\alpha_d)\, \vec{U}_1 - \alpha_d\vec{U}_2) \qquad 2.19$$

where U_1 = U having direction θ and $U_2 = \sqrt{1-\alpha_T}\, U$ having direction $\frac{\pi}{2}$.

2.2.2. Reduction to Schamberg Model

The Schamberg model already has much in common with the proposed generalized model in that the reflection is considered as being in a beam which is axially symmetric about an angle which is not necessarily in the specular or diffuse direction. The principle differences between the two models is the manner in which the reflected velocity and the angle of reflection are defined.

In the Schamberg model, a specific form for the distribution of velocity in the reflected beam is given. The velocity of reflected molecules are assumed to be equal in magnitude but distributed in direction and number according to a cosine law within a beam width of angle ϕ_o (see Figure 2.3) given by

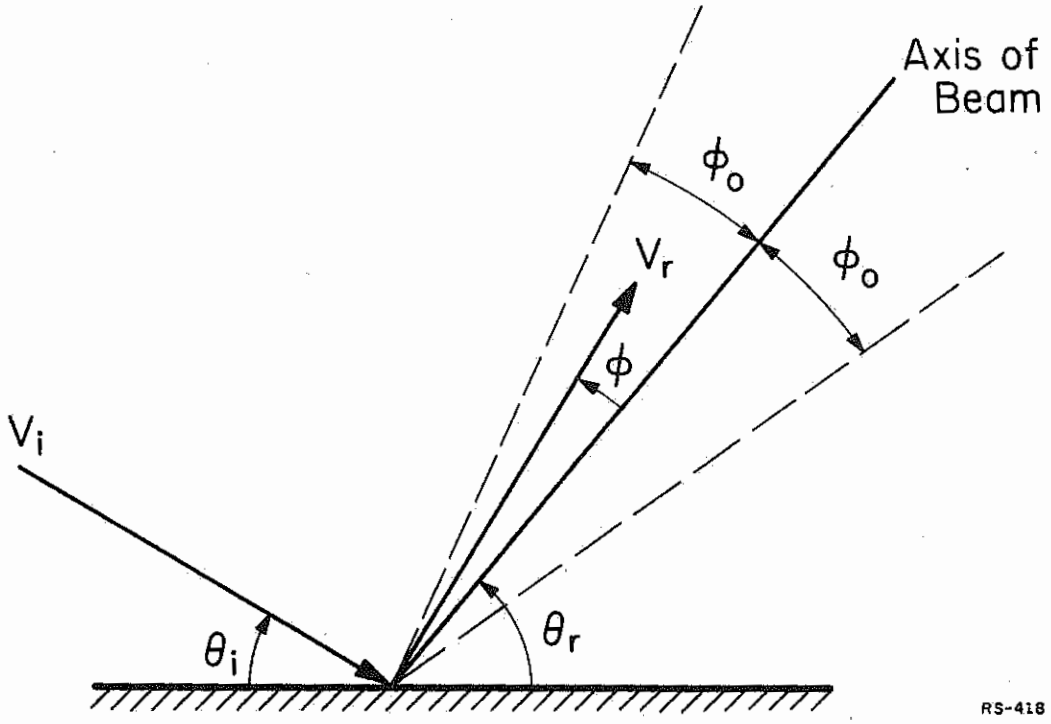

Figure 2.3. Notation used in the Schamberg model.

$$n_r(\phi) = K \cos\left(\frac{\phi}{\phi_o} \cdot \frac{\pi}{2}\right) \qquad 2.20$$

where n_r is the number of re-emitted molecules per unit time whose direction of re-emission (relative to the axis of the beam) lies between ϕ and $(\phi+d\phi)$. The constant K is related to the number flux of reflected molecules and is dependent upon whether the reflected beam is two-dimensional (wedge shape) or three-dimensional (conical shape).

To reduce the generalized model to the Schamberg model, the average velocity of the reflected beam must be found. For a three-dimensional conical beam the average reflected velocity can be determined from expressions derived by Schamberg,

$$U_j = \Phi_3(\phi_o)V_r \qquad 2.21$$

where $\Phi_3(\phi_o)$ is defined in Schamberg's 1959 paper, and V_r is the magnitude of the constant velocity of individual molecules in the reflected beam. The quantity $\Phi_3(\phi_o)$ has a maximum value of one for $\phi_o = 0$ and a minimum value of 2/3 for $\phi_o = \frac{\pi}{2}$. The velocity V_r is related to the incident velocity V_i (or U in the notation being used for the generalized model) by a thermal accommodation coefficient, α, which has been defined in Equation 2.2, i.e.

$$V_r = \sqrt{1-\alpha}\, V_i \qquad 2.22$$

Substituting Equation 2.22 into the expression for U_j in Equation 2.21, the following expression relating U_j to U is obtained.

$$U_j = \sqrt{1-\alpha}\, \Phi_3(\phi_o)\, U \qquad 2.23$$

Therefore, in order to reduce the generalized model to the Schamberg model, the parameter α_j must be defined as

$$\sqrt{1-\alpha_j} = \sqrt{1-\alpha}\ \Phi_3\ (\phi_o) \qquad 2.24$$

The two parameters, α and ϕ_o, of the Schamberg model are then reduced to one parameter α_j.

The angle-of-reflection law proposed by Schamberg is given by

$$\cos\ \theta_j = (\cos\ \theta)^{\upsilon} \qquad 2.25$$

and was discussed briefly in section 2.1.2. A plot of Equation 2.25 for various values of υ is given in Figure 2.4. A rough approximation to variation in θ_j as a function of θ for the Schamberg model can be made by discontinuous linear relationships. For example,

$$\begin{aligned} \theta_j &= a_j + b_j\theta, \text{ for } \theta \leq \theta^* \\ &= c_j + d_j\theta, \text{ for } \theta \geq \theta^* \end{aligned} \qquad 2.26$$

For the Schamberg model Equation 2.25, the θ_j vs θ curves all pass through the (0,0) and $(\frac{\pi}{2},\frac{\pi}{2})$ points. Using this information, $a_j = 0$, $c_j = \frac{\pi}{2}(1-d_j)$. Also, using the fact that at $\theta = \theta^*$ the two lines intersect, Equations 2.26 reduce to

$$\begin{aligned} \theta_j &= \left[\frac{\pi}{2}\frac{(1-d_j)}{\theta^*} + d_j\right]\theta \qquad \text{for } \theta \leq \theta^* \\ &= \frac{\pi}{2}(1-d_j) + d_j\theta \qquad \text{for } \theta \geq \theta^* \end{aligned} \qquad 2.27$$

A one parameter family of discontinuous linear curves can be developed from Equations 2.27 for a choice of a relationship between θ^* and θ. This is illustrated in Figure 2.5 where θ^* was chosen to occur along the line from $(0, \frac{\pi}{2})$ to $(\frac{\pi}{2},0)$. The approximation illustrated in Figure 2.5 retains the essential characteristics of the Schamberg cosine variation.

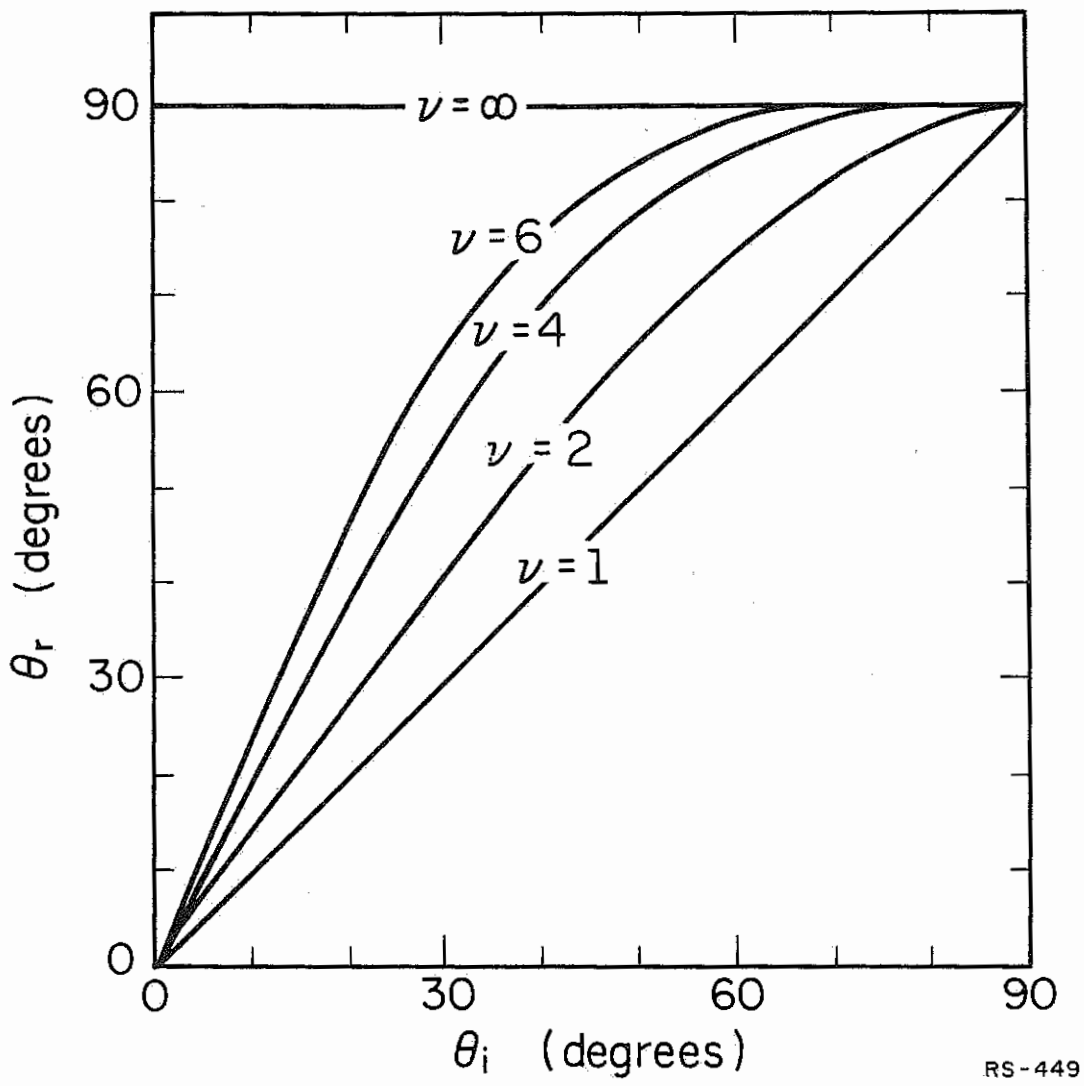

Figure 2.4. Plot of Schamberg's angle-of-reflection law.

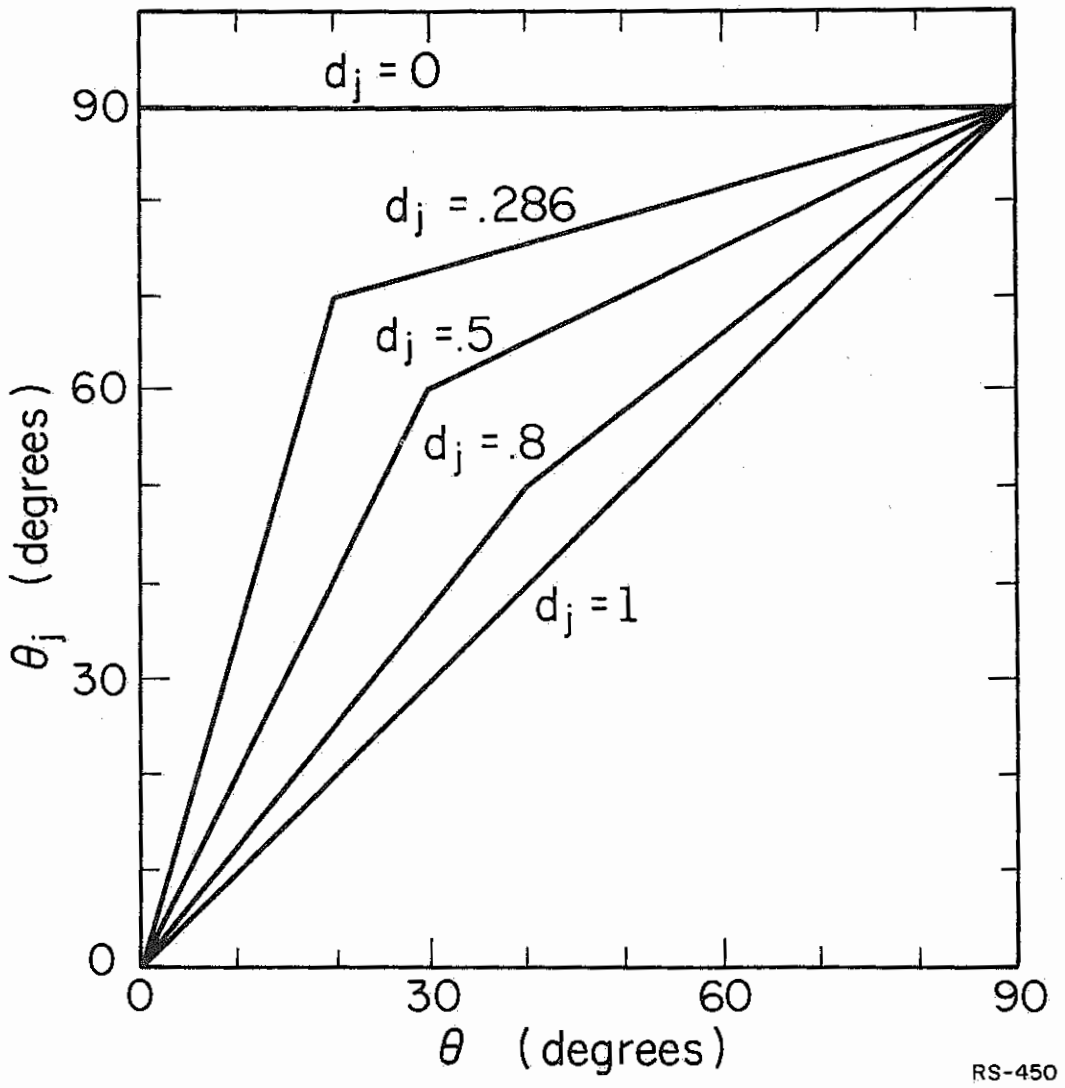

Figure 2.5. Plot of possible angle-of-reflection relationships formed by discontinuous linear curves.

2.2.3. Reduction to Nocilla Model

Nocilla[14] postulated that the distribution of re-emitted molecular velocities be a drifting Maxwellian having a drift velocity of U_r in the direction θ_r. The distribution function of reflected velocities is written

$$f_r(C) = \frac{n_r}{(2\pi RT_r)^{\frac{1}{2}}} \exp\left[-\frac{(C-U_r)^2}{2RT_r}\right] \qquad 2.28$$

where C is the molecular velocity. Since number flux must be conserved at the surface, n_r can be related to the incident number flux. There are, then, three parameters remaining to describe the reflection, U_r, θ_r, and T_r.

Nocilla has shown that the model can be made to closely match the distribution obtained experimentally by Hurlbut[16], for proper choice of the quantities U_r, θ_r and T_r. However, Nocilla doesn't propose an angle-of-reflection law or a relation between the incoming and reflected velocities. Therefore, in order to develop an interaction model using the distribution function proposed by Nocilla, these relationships must be provided.

The Nocilla distribution function for reflected molecules has been applied to the calculation of forces on a solid surface in free molecular flow by Hurlbut and Sherman.[6] Their results can be used to show that the Nocilla model is a subclass of the proposed generalized model.

The force on a surface due to a reflection of the Nocilla type is divided by Hurlbut and Sherman into components in the direction of the incoming beam, D_r, and perpendicular, L_r. (See Figure 2.6).

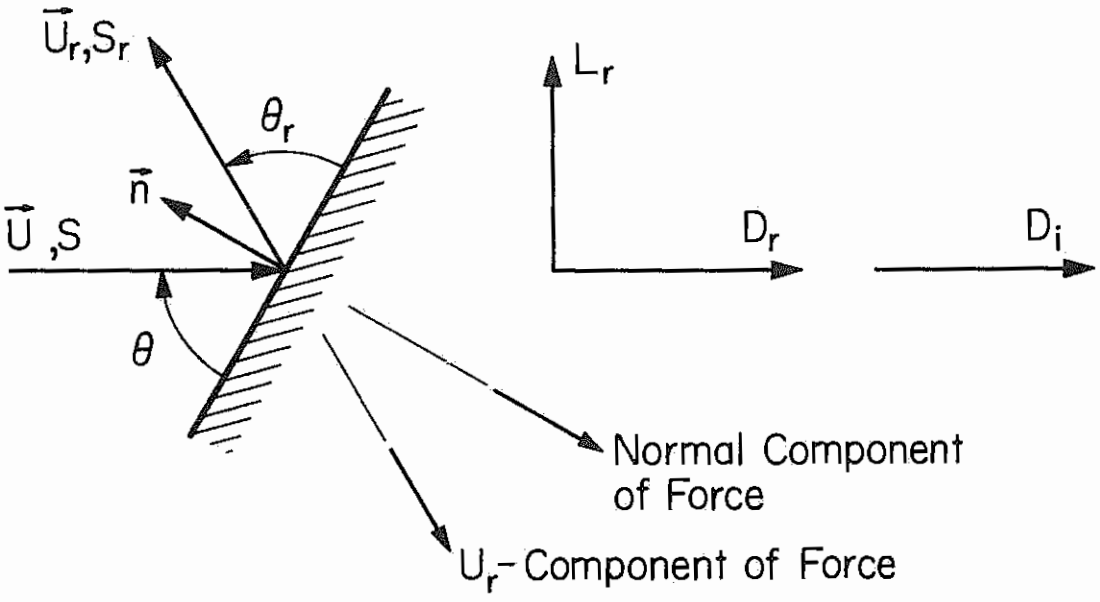

Figure 2.6. Notation used in the Nocilla model.

$$D_r = \frac{n_r m U_r^2}{2\pi^{\frac{1}{2}} S_r^2} \left[\{\sigma_r \chi(\sigma_r) + \frac{1}{2} \pi^{\frac{1}{2}} (1+\text{erf } \sigma_r)\} \sin \theta \right.$$

$$\left. - S_r \cos \theta_r \{\chi(\sigma_r)\} \cos \theta \right] \qquad 2.29$$

$$L_r = \frac{n_r m U_r^2}{2\pi^{\frac{1}{2}} S_r^2} \left[\{\sigma_r \chi(\sigma_r) + \frac{1}{2} \pi^{\frac{1}{2}} (1+\text{erf } \sigma_r)\} \cos \theta \right.$$

$$\left. + S_r \cos \theta_r \{\chi(\sigma_r)\} \sin \theta \right] \qquad 2.30$$

where

$$S_r = U_r/(2RT_r)^{\frac{1}{2}}$$

$$\sigma_r = S_r \sin \theta_r \qquad 2.31$$

$$\chi(\sigma_r) = e^{-\sigma_r^2} + \pi^{\frac{1}{2}} \sigma_r (1+\text{erf } \sigma_r)$$

If the term $\chi(\sigma_r)$ is factored out of Equations 2.29 and 2.30, and if the expression for σ_r in Equations 2.31 is used, D_r and L_r become.

$$D_r = \frac{n_r m U_r^2}{2\pi^{\frac{1}{2}} S_r^2} \chi(\sigma_r) \left[-S_r \cos (\theta + \theta_r) + \frac{\pi^{\frac{1}{2}} (1+\text{erf } \sigma_r)}{2\chi(\sigma_r)} \sin \theta \right]$$

$$L_r = \frac{n_r m U_r^2}{2\pi^{\frac{1}{2}} S_r^2} \chi(\sigma_r) \left[S_r \sin (\theta + \theta_r) + \frac{\pi^{\frac{1}{2}} (1+\text{erf } \sigma_r)}{2\chi(\sigma_r)} \cos \theta \right] \qquad 2.32$$

From these equations, it is apparent that the vector force on the surface due to a reflection of the Nocilla type can be divided into components normal to the surface and in the direction of the velocity U_r. From Equations 2.32

$$\vec{F}_{\text{reflection}} = \frac{n_r m U_r^2}{2\pi^{\frac{1}{2}} S_r^2} \chi(\sigma_r) \left[-S_r \frac{\vec{U}_r}{U_r} + \frac{\frac{1}{2} \pi^{\frac{1}{2}} (1+\text{erf } \sigma_r)\vec{n}}{\chi(\sigma_r)} \right] \qquad 2.33$$

The outgoing number flux $\dot{N}_r$ is given by

$$\dot{N}_r = n_r \left(\frac{k\,T_r}{2\pi m}\right)^{\frac{1}{2}} \chi(\sigma_r) \qquad 2.34$$

Substituting Equation 2.33 into 2.34 and using the conservation of mass flux condition

$$m\dot{N}_r = m\dot{N} = \rho\vec{U}\cdot\vec{n} \qquad 2.35$$

Equation 2.33 reduces to

$$\vec{F}_{reflection} = \rho\ \vec{U}\cdot\vec{n}\left[-\vec{U}_r + G(\sigma_r)\ \vec{n}\right] \qquad 2.36$$

where

$$G(\sigma_r) = \frac{(2RT_r)^{\frac{1}{2}}}{2\chi(\sigma_r)}\ \left[\pi^{\frac{1}{2}}(1+\text{erf}\ \sigma_r\right] \qquad 2.37$$

In terms of the proposed generalized model, a reflection of the Nocilla type can be considered to be composed of two beams, one normal to surface and one in the direction of $\vec{U}_r$. The parameter σ_j is not needed since conservation of mass flux is automatically satisfied by the two beams. Let beam j = 1 be in the $\vec{U}_r$ direction. Since one is free to choose relationships for the U_r and θ_r, let

$$U_r = \sqrt{1-\alpha_r}\ U \text{ and } \theta_r = \frac{\pi}{2}\ P_r + (1-P_r)\ \theta \qquad 2.38$$

Consider beam j = 2 to be normal to the surface. Then

$$U_2 = G(\sigma_r) = \Phi(\sigma_r)c_r \qquad 2.39$$

where

$$c_r = (2RT_r)^{\frac{1}{2}}$$

then from Equation 2.37, define

$$\Phi(\sigma_r) = \frac{\pi^{\frac{1}{2}}}{2} \frac{1+\text{erf } \sigma_r}{\chi(\sigma_r)} \qquad 2.40$$

Assuming the the velocity c_r is related to the incident velocity u by the thermal accommodation coefficient α,

$$c_r = \sqrt{1-\alpha} \quad U \qquad 2.41$$

we can define the parameter α_2 as

$$\sqrt{1-\alpha_2} = \sqrt{1-\alpha}\ \Phi(\sigma_r) \qquad 2.42$$

The reduction of the generalized model to a model using the Nocilla reflected distribution function is now complete. The model obtained still contains three parameters; α_r, P_r, and α_2. This form of model serves to illustrate some interesting characteristics of the Nocilla distribution function. The forces caused by a reflection of the Nocilla type are seen to have the character of a Maxwell reflection model except that, instead of a specular component, a U_r component is employed. Also, similar to the Maxwell model, the magnitude of the U_r component of reflection is seen to determine, except for one parameter, the magnitude of the normal component of reflection. The normal component of reflection is analogous to the diffusion component in the Maxwell model. Figure 2.7 shows a plot of the coefficient of the normal component of the Nocilla distribution function, $\Phi(\sigma_r)$, as a function σ_r. The term σ_r is equal to the product of U_r and sin θ_r divided by c_r. From Figure 2.7, as U_r becomes large compared to c_r, the magnitude of the normal component becomes small. At $\theta_r = 0$, the normal

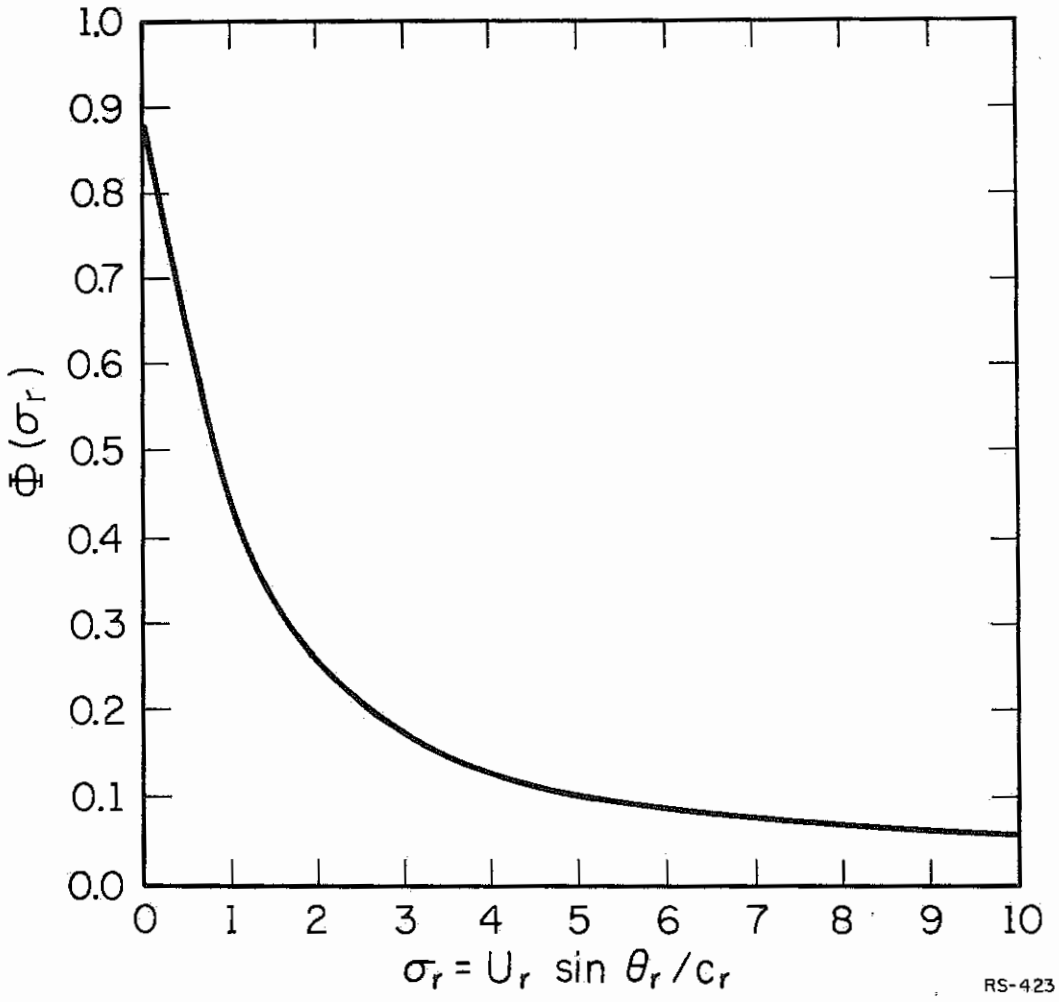

Figure 2.7. Plot of the coefficient of the normal component of force for the Nocilla model as a function of σ_r.

component has a maximum value of .89 c_r. Due to its dependence on sin θ_r, the quantity σ_r can not in general be assumed to always be large. However, under the special conditions of U_r being much greater than c_r and P_r greater than zero (this condition on P_r insures that sin θ_r and therefore σ_r will not be zero), the quantity $\Phi(\sigma_r)$ may be assumed to be small in comparison to the U_r component of reflection. Under these conditions, the Nocilla distribution function resembles the type of reflection described by the generalized model with the average velocity U_j replaced by the velocity U_r of the Nocilla distribution.

2.3. Incorporation of Experimental Results

2.3.1. Current Status of Molecular Beam Experiments

Molecular beam experiments have not as yet been able to obtain results which could be directly applicable to the calculation of forces and torques on a satellite. The major limitation in molecular beam experiments is the inability to produce a neutral molecular beam of sufficient intensity and at a velocity which corresponds to the velocity of impingement of atmospheric molecules on a satellite in near earth orbit. In terms of the energy of interaction, the range of 1 to 10 ev corresponds to that which occurs in a near earth orbit. Interaction energies below 1 ev have been obtained by aerodynamic methods such as expansion of a high pressure gas through a nozzle. On the high energy side of the 1 to 10 ev range (10 ev and above) neutral molecular beams have been obtained by the method of ion acceleration with subsequent neutralization by charge exchange techniques (see for example Reference 2).

Although the energy of interaction is of primary importance in determining the character of the gas-surface interaction, other factors such as the satellite surface conditions and composition of gases incident on the surface are also believed to influence the interaction. The major limitation in duplicating these factors in molecular beam experiments has been that satellite surface condition and atmospheric composition remain uncertain.

As can be concluded from the above discussion, available experimental results are probably not applicable for determining accurately the values of the gas-surface interaction parameters for the calculation of aerodynamics forces on satellites. However, molecular beam experiments outside the 1 to 10 ev range could for example suggest the form of the θ_j vs θ relationship, or, indicate trends in the character of the interaction which could be extrapolated to the 1 to 10 ev range.

2.3.2. Incorporation of Intensity Distribution

The majority of experimental work is aimed toward obtaining information on the distribution function of reflected molecules because all other flow properties can be found from the distribution function. For application to calculating forces on convex satellite shapes, however, less detailed information can be used since the actual form of the distribution function is unimportant. The generalized gas-surface interaction model developed in section 2.1 suggests the type of experimental data which would be most useful for satellite application. For example,

distribution of reflected intensity provides information on the number of beam components (single lobed, J = 1; bi-lobed, J = 2; etc). Also, intensity distributions obtained for various angles of attack to the incident beam reveals characteristics of the θ_j vs θ relation. As an example, the experimental results of θ_r vs θ for high velocity argon beams on heated platimum obtained by Moran, Wachman, and Trilling[17] are plotted in Figure 2.8. These results show that as the beam velocity increases, the parameter P_j (using the first approximation for the θ relationship) approaches zero. These results show a slight departure from a linear relation in θ_r vs θ at low incidence angles. The departure is opposite to that postulated by Schamberg's (see Figure 2.4) cosine powered relationship.

Overspecular ($\theta_j < \theta$) and backscatter ($\theta_j > \frac{\pi}{2}$) results can not be reproduced in the Schamberg or the Maxwell model. Such results are, however, easily incorporated into the generalized model. For example, backscattering results could be approximated by a linear relation by allowing P_j to take on values between 1 and 2. Overspecular results and over-backscatter ($\theta_j > \pi - \theta$) could be approximated by 2nd or 3rd degree polynomials or by discontinuous linear relations. These regions are indicated in Figure 2.9 with examples of the possible angular relationships.

2.3.3. Incorporation of Force Measurements

Force measurements made on flat surfaces at angles of attack to a molecular beam can yield considerable information on the gas-surface interaction and the results are particularly suited for analysis in terms of

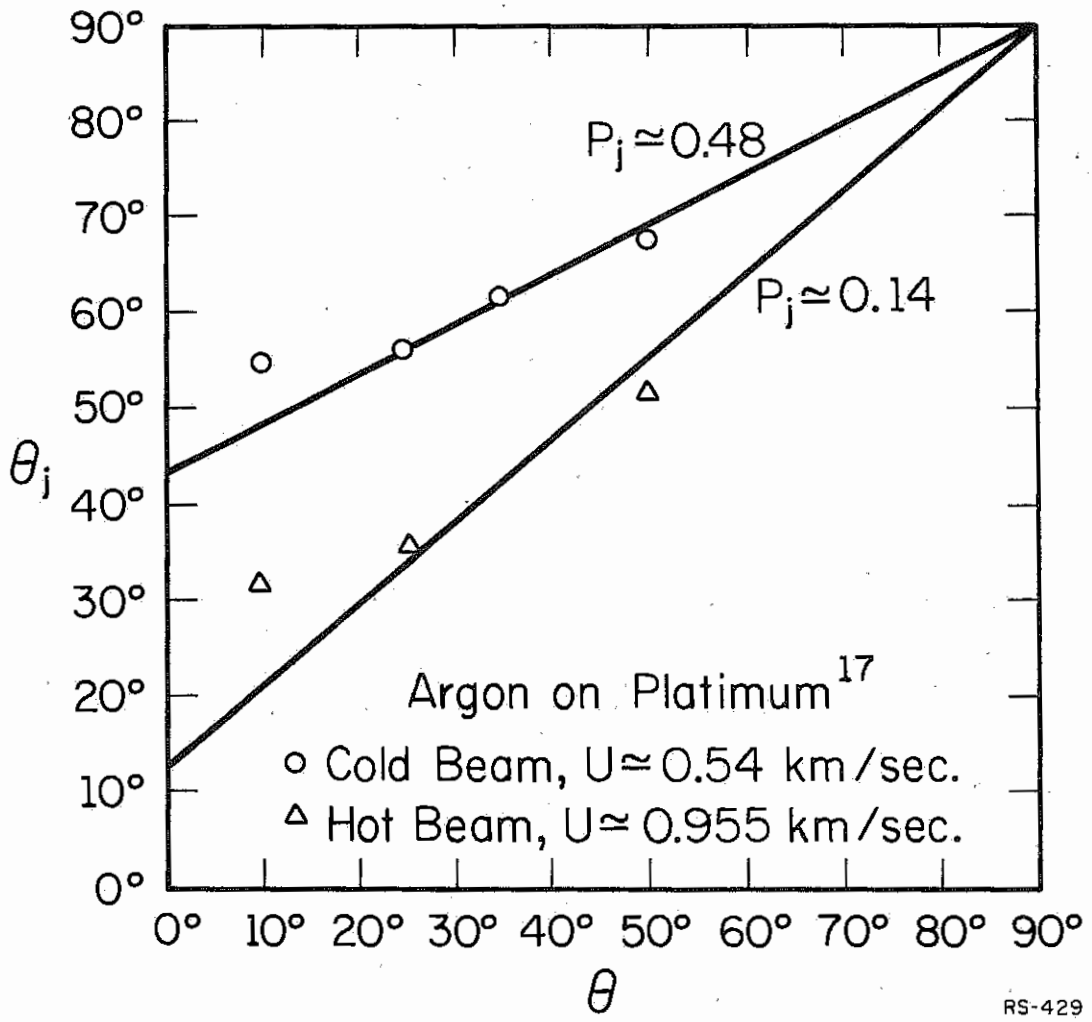

Figure 2.8. Comparison of experimental data[17] with the first approximation to an angle-of-reflection law of the generalized model.

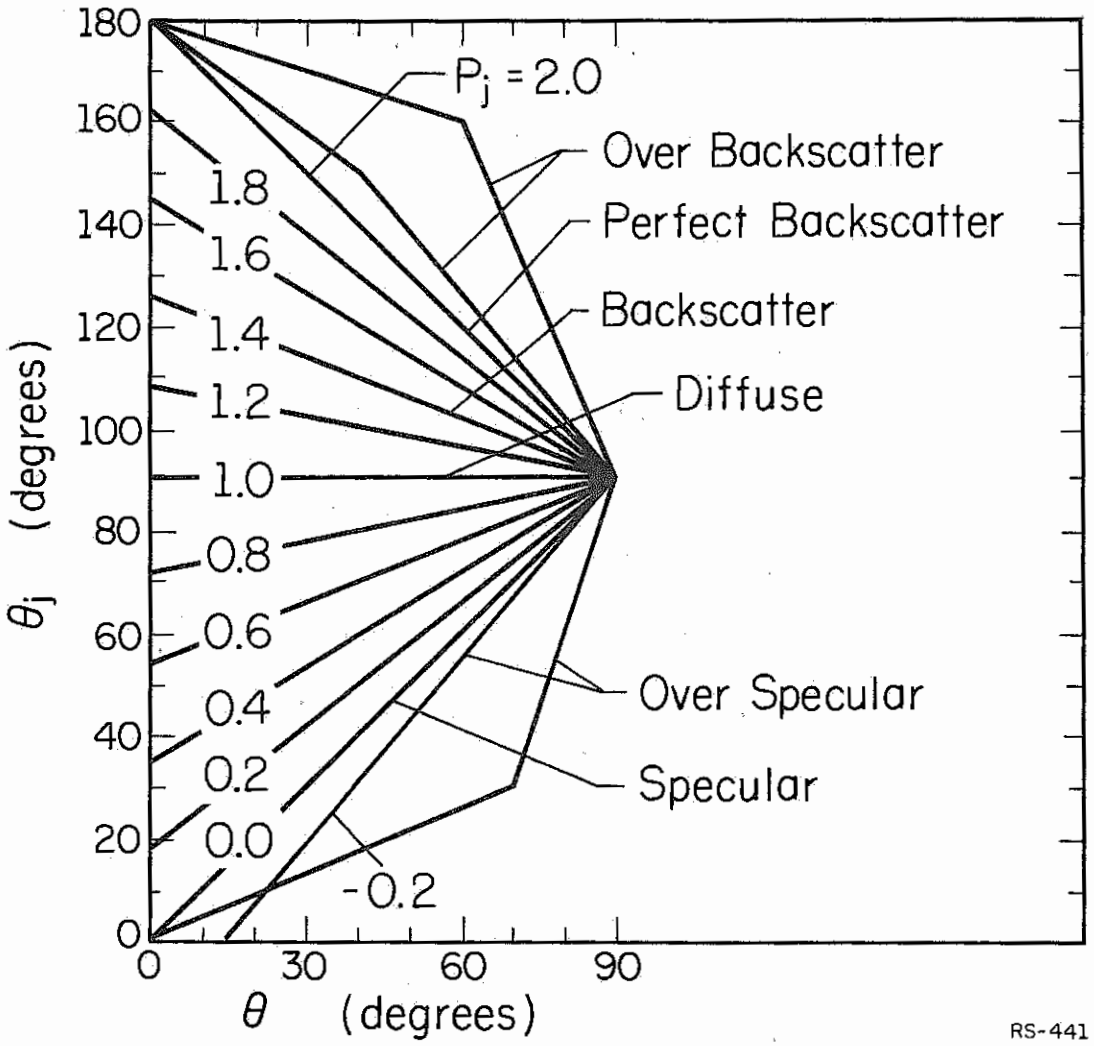

Figure 2.9. The full range of possible angle-of-reflection laws in the generalized model.

the generalized model. Since the force on the surface due to the impingement can be obtained from measured beam velocity and intensity, the force due to the reflection of molecules can be directly obtained. Therefore, the magnitude and direction of the reflection force can be determined to yield information on the θ_j vs θ relationship and also the value of $\sigma_j\sqrt{1-\alpha_j}$. In order to properly analyze force measurements in this manner, however, it is necessary to know the number of beam components which make up the reflection. Experiments set up to measure forces are not usually set up to measure the distribution of intensity which could reveal the number of beam components. In the absence of such information, special measuring techniques can be employed to obtain the desired information from the force measurements. For example, the technique employed by Boring and Humphris[18] to obtain reflected force in the directions normal and tangential to the surface can be extended to obtain measured values of the reflected force at angles between those two limits. The results would reveal the lobal maxima of the beam components and thereby yield information on the θ_j relationship and the quantities $\sigma_j\sqrt{1-\alpha_j}$.

2.4. Significance of the Proposed Model

The generalized gas-surface interaction model developed in this chapter was shown to be reducible to three currently accepted gas-surface interaction models. In addition, the generalized model is found to be applicable to approximating a wide range of possible gas-surface interaction by including the possibilities of over-specular and backscatter reflection.

The generalized model is found to also be useful in the interpretation of laboratory experiment results, as illustrated in Figure 2.8, in order to indicate trends and similarities in laboratory data.

The generalized model described in this chapter has incorporated 1) the effect of the angle of incidence on the angle of reflection and 2) the effect of the incident velocity on the reflected velocity. These are undoubtedly the major factors influencing the gas-surface interaction. Additional factors, however, can readily be incorporated into the generalized model. For example, the velocity of reflection could be considered to be a function of the angle of incidence as well as a function of the incident velocity. This effect is, in fact, incorporated in the results obtained in the reduction of the generalized model to the Nocilla model. The generalized model could also be extended to include the possibility that σ_j and α_j are both functions of U and θ. Although refinements such as these will not be included in the application of the generalized model in the work which follows, they may be incorporated whenever warrented.

The generalized model employs three parameters σ_j, α_j, and P_j for each beam of the reflection. The two parameters σ_j and α_j determine the magnitude of the force due to the reflection and the parameter P_j determines the direction of that force. When using the generalized model, as will be seen in the following chapters, the quantity $\sigma_j\sqrt{1-\alpha_j}$ can be considered as a single parameter in place of both σ_j and α_j. That is, specification of the two quantities $\sigma_j\sqrt{1-\alpha_j}$ and P_j are sufficient for determining the force and torque acting on a convex body in a free molecular flow.

In the analysis of subsequent chapters, the generalized model

will be employed in the development of equations which express the aerodynamic properties of bodies in a free molecular flow.

3. BASIC AERODYNAMICS EQUATIONS

The generalized gas-surface interaction model is applied in this chapter to the development of the equations for expressing force and torque acting on spinning bodies in free molecular flow. The resulting equations have wide application since they can be interpreted in terms of many specific models.

The equations for drag, lift, and torque are obtained in differential form for four body shapes in particular (disk, cylinder, cone, and sphere). The results will be used in the next chapter to study the effects of spin and the gas–surface interaction on the aerodynamic properties of bodies of these shapes.

3.1. Basic Equations of Force and Torque

Consider a surface element, dA, on a spinning body. If the positive normal of that element of surface is $\vec{n}$, the mass flux impinging on the surface is

$$-\rho\,\vec{U}\cdot\vec{n}\,dA$$

where ρ is the density of the free stream gas and $\vec{U}$ is the vector velocity of the incident flow relative to the surface. The velocity U is assumed to be much higher than the thermal motion of the free stream gas so that random fluctuations in the velocity can be neglected (hypothermal assumption). The mass flux is a positive number since the quantity $(\vec{U}\cdot\vec{n})$ must always be negative in order for molecules to hit the surface. The vector force on the surface due to the impingement of molecules is given by

$$(d\vec{F})_{incident} = \vec{U}(-\rho\ \vec{U}\cdot\vec{n}\ dA) \qquad 3.2$$

where the notation $d\vec{F}$ is used to denote the force on the surface area dA.

Using the notation introduced in the preceding chapter for the generalized model, the vector force due to the reflection of molecules is given by

$$(d\vec{F})_{reflection} = -\sigma_j\ \vec{U}_j\ (-\rho\vec{U}\cdot\vec{n}\ dA) \qquad 3.3$$

where the minus sign is required because the vector velocity $\vec{U}_j$ must be in the direction away from the surface. For cases in which the reflection is composed of more than one beam component, the force due to the reflection is given by

$$(d\vec{F})_{reflection} = -(\sigma_1\vec{U}_1 + \sigma_2\vec{U}_2 + \cdots + \sigma_J\vec{U}_J)\ (-\rho\vec{U}\cdot\vec{n})\ dA \qquad 3.4$$

where J is the number of beams making up the reflection. Since the repeated subscripts can be used to imply the summation, Equation 3.3 will be used in the development of equations which follow.

The total vector force on the element of surface is the sum of force due to impingement and force due to reflection given by

$$d\vec{F} = -(\vec{U} - \sigma_j\vec{U}_j)\ \rho\ \vec{U}\cdot\vec{n}\ dA \qquad 3.5$$

Consider the element of surface dA to be at a point defined by the radius vector, $\vec{R}$, from the center of a coordinate system attached to the body. The vector torque, $d\vec{T}$, about the center of the coordinate system caused by the impingement and reflection of molecules on the element of surface dA is then

$$d\vec{T} = -\vec{R}x\ (\vec{U} - \sigma_j \vec{U}_j)\ \rho\ \vec{U}\cdot\vec{n}\ dA \qquad 3.6$$

Equations 3.5 and 3.6 form the basic equations necessary for determining the force and torque on a convex body in free molecular flow. These equations are not applicable to concave body shapes which allow molecules reflected from one part of the body surface to impinge again on the body.

3.2. Aerodynamics Equations for a Class of Spinning Body Shapes

For spinning bodies, the velocity of impinging molecules with respect to the surface elements depends upon the spin rate and position of the surface element with respect to the spin axis. Let U_∞ be the free stream velocity and let the spin rate of the body be defined by a spin vector, $\vec{\Omega}$. The vector velocity of impinging molecules with respect to any point on the surface exposed to the flow is then given by

$$\vec{U} = \vec{U}_\infty - \vec{\Omega}\times\vec{R} \qquad 3.7$$

where $\vec{R}$ is the radius vector from the center of a coordinate system attached to the body (see Figure 3.1).

The reflected velocity vector, $\vec{U}_j$, is also dependent upon position on the surface and spin rate since the magnitude and direction of $\vec{U}_j$ is related to the magnitude and direction of the incident velocity $\vec{U}$ through the parameters introduced in the generalized model. For a given body shape (within the class of convex shapes) the velocity vector U_j can be written in terms of the vectors $\vec{U}$, $\vec{n}$, $\vec{\Omega}$, and $\vec{R}$ and the appropriate gas-surface interaction parameters. For example, consider the class of body shapes which

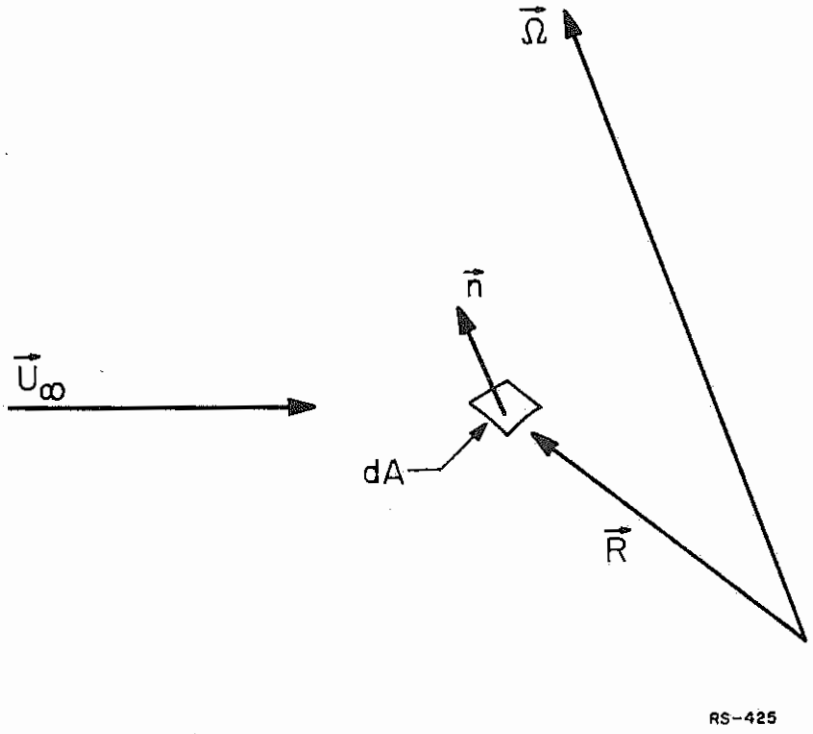

Figure 3.1. Vector position of surface element in the flow.

have circular cross section at any point along the spin-axis. For this class of body shapes, a local unit tangent vector, $\vec{t}$, can be defined as

$$\vec{t} = \frac{\vec{\Omega}\times\vec{R}}{|\vec{\Omega}\times\vec{R}|} \qquad 3.8$$

where $|\vec{\Omega}\times\vec{R}|$ represents the magnitude of the vector quantity $\vec{\Omega}\times\vec{R}$.

Since $\vec{n}$ is the local unit normal vector to the surface element dA, a third unit vector, $\vec{m}$, can be defined to form a triad.

$$\vec{m} = \vec{n} \times \frac{(\vec{\Omega}\times\vec{R})}{|\vec{\Omega}\times\vec{R}|} \qquad 3.9$$

The unit vector $\vec{m}$ is also locally tangent to the surface. Consider now that the incident velocity vector, $\vec{U}$, has component U_n, U_t, U_m in the directions of $\vec{n},\vec{t},\vec{m}$, respectively. That is, let

$$\vec{U} = U_t\,\vec{t} + U_m\,\vec{m} + U_n\,\vec{n} \qquad 3.10$$

Also, let $\vec{U}_j$ be defined in this coordinate system as

$$\vec{U}_j = (U_j)_t\,\vec{t} + (U_j)_m\,\vec{m} + (U_j)_n\,\vec{n} \qquad 3.11$$

If the angle θ represents the angle of incidence with respect to the surface plane (see Figure 3.2), the components of $\vec{U}$ are given by

$$\begin{aligned} U_t &= U\cos\theta\cos\gamma \\ U_m &= U\cos\theta\sin\gamma \\ U_n &= -U\sin\theta \end{aligned} \qquad 3.12$$

where U is the magnitude of the incident velocity and γ is the azimuth angle of incidence defined in Figure 3.2.

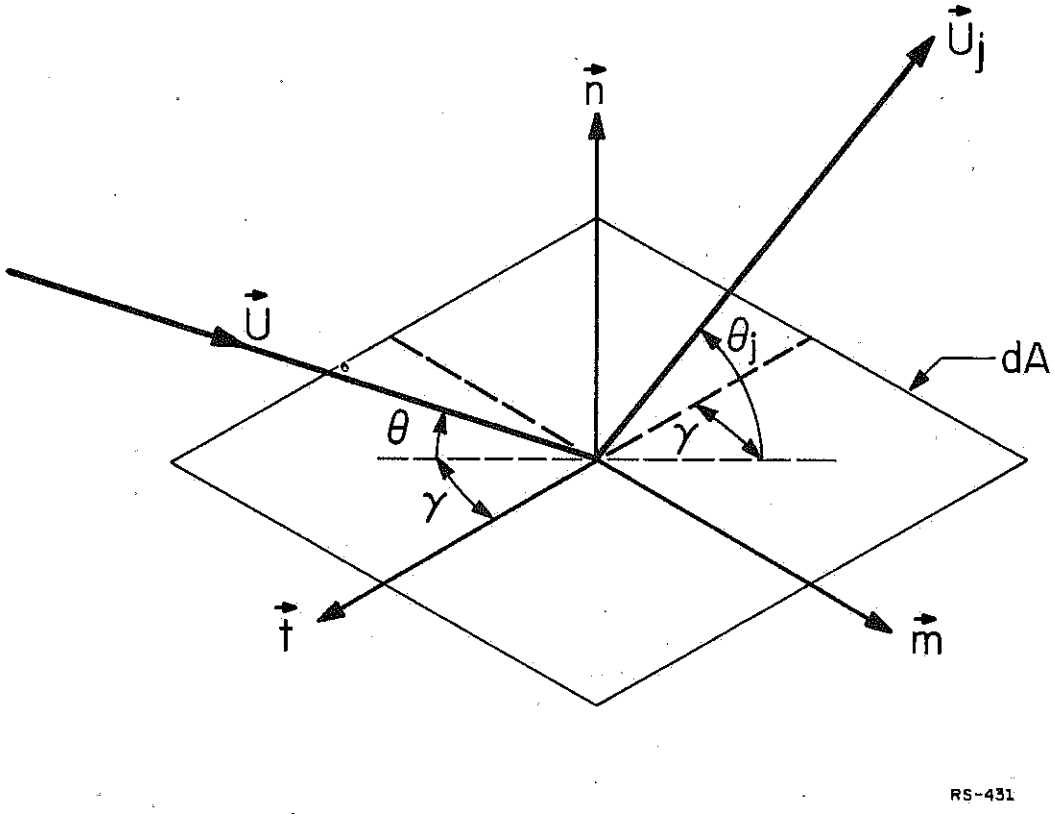

Figure 3.2. Local coordinate system on the surface element.

Since the reflection is in the plane of $\vec{U}$ and $\vec{n}$, the components of U_j can be written in terms of θ_j and γ.

$$\begin{aligned} (U_j)_t &= -U_j \cos\theta_j \cos\gamma \\ (U_j)_m &= -U_j \cos\theta_j \sin\gamma \\ (U_j)_n &= -U_j \sin\theta_j \end{aligned} \qquad 3.13$$

where U_j is the magnitude of the reflected velocity, $\vec{U}_j$. The quantity U_j is related to the quantity U by the expression given in chapter 2. That is,

$$U_j = \sqrt{1-\alpha_j}\, U \qquad 3.14$$

The angle γ is found in terms of the vector $\vec{U}$, by the following identities

$$\begin{aligned} U\cos\gamma &= \frac{\vec{U}\cdot\vec{t}}{\cos\theta} \\ U\sin\gamma &= \frac{\vec{U}\cdot\vec{m}}{\cos\theta} \\ U &= \frac{-\vec{U}\cdot\vec{n}}{\sin\theta} \end{aligned} \qquad 3.15$$

Using Equations 3.15 and 3.14 in Equations 3.13, Equation 3.11 becomes

$$\vec{U}_j = \sqrt{1-\alpha_j}\left[\frac{\cos\theta_j}{\cos\theta}(\vec{U}\cdot\vec{t})\,\vec{t} + \frac{\cos\theta_j}{\cos\theta}(\vec{U}\cdot\vec{m})\,\vec{m} - \frac{\sin\theta_j}{\sin\theta}(\vec{U}\cdot\vec{n})\,\vec{n}\right] \qquad 3.16$$

Using the definitions of $\vec{t}$ given in Equation 3.8 and $\vec{m}$ given in Equation 3.9, Equation 3.16 reduces to the following form

$$\begin{aligned} \vec{U}_j = \sqrt{1-\alpha_j}\Bigg\{&\frac{\cos\theta_j}{\cos\theta}\left[\vec{U}\cdot\vec{\Omega}\times\vec{R}\right]\vec{\Omega}\times\vec{R}\;\left(\left|\vec{\Omega}\times\vec{R}\right|\right)^{-2} \\ &+ \frac{\cos\theta_j}{\cos\theta}\left[\vec{U}_\infty\cdot\vec{n}\times(\vec{\Omega}\times\vec{R})\right]\vec{n}\times(\vec{\Omega}\times\vec{R})\;\left(\left|\vec{\Omega}\times\vec{R}\right|\right)^{-2} \\ &- \frac{\sin\theta_j}{\sin\theta}\left[\vec{U}\cdot\vec{n}\right]\vec{n}\Bigg\} \end{aligned} \qquad 3.17$$

Equation 3.17 is valid for any body shape which is both convex and has circular cross sections at any point along the spin axis. For shapes of this class, the vector $\vec{\Omega}\times\vec{R}$ is always perpendicular to the unit normal vector $\vec{n}$. Therefore, using Equation 3.7, the following can be obtained

$$\vec{U}\cdot\vec{n} = (\vec{U}_\infty - \vec{\Omega}\times\vec{R})\cdot\vec{n} = \vec{U}_\infty\cdot\vec{n} \tag{3.18}$$

Substituting Equations 3.18, 3.17, and 3.7 into Equation 3.5, the vector force on an element of surface of a spinning body having circular cross-sections about the spin axis becomes

$$d\vec{F} = -\rho(\vec{U}_\infty\cdot\vec{n})dA\left\{\vec{U}_\infty - \vec{\Omega}\times\vec{R} + C_j(|\vec{\Omega}\times\vec{R}|)^{-2}\left[\vec{U}_\infty\cdot(\vec{\Omega}\times\vec{R}) - (|\vec{\Omega}\times\vec{R}|)^2\right]\vec{\Omega}\times\vec{R}\right.$$
$$\left. + C_j(|\vec{\Omega}\times\vec{R}|)^{-2}\left[\vec{U}_\infty\cdot\vec{n}\times(\vec{\Omega}\times\vec{R})\right]\vec{n}\times(\vec{\Omega}\times\vec{R}) - S_j\left[\vec{U}_\infty\cdot\vec{n}\right]\vec{n}\right\} \tag{3.19}$$

where

$$C_j = \sigma_j\sqrt{1-\alpha_j}\ \frac{\cos\theta_j}{\cos\theta} \tag{3.20}$$

$$\text{and } S_j = \sigma_j\sqrt{1-\alpha_j}\ \frac{\sin\theta_j}{\sin\theta} \tag{3.21}$$

The equation for torque can be obtained directly from Equation 3.19 by taking the cross product with the vector $\vec{R}$.

In the above analysis the force and torque acting on a spinning body are expressed in terms of the parameters of the generalized gas-surface interaction model. For a given body shape in the class of shapes for which Equation 3.19 is valid, the vectors $\vec{U}_\infty$, $\vec{\Omega}$, $\vec{R}$, and $\vec{n}$ are known. In the following sections, the force and torque equations will be developed for four basic body shapes (the disk, cylinder, cone, and sphere) which will

illustrate the application of Equation 3.19. The results will be analyzed in the following chapter for specific values of the generalized gas-surface interaction parameters.

3.2.1. Coordinate Systems

Two coordinate systems will be used in the development of equations for the disk, cylinder, cone, and sphere. The two coordinate systems which are the same for each case are defined as follows.

Consider first a coordinate system (x,y,z) which is attached to the free stream velocity vector, $\vec{U}_\infty$. The positive y axis will always be defined to be in the positive $\vec{U}_\infty$ direction. Consider now a body having a spin vector $\vec{\Omega}$. Let a coordinate system (x_s,y_s,z_s) be defined in which the z_s axis is always in the direction of the spin vector $\vec{\Omega}$. Furthermore, consider the z_s axis to be initially inclined at an angle θ_s with respect to the z axis of the x,y,z coordinate systems and in the x-z plane. Also consider the x_s axis to be initially collinear with the x axis. The coordinate systems are shown in Figure 3.3.

The x_s,y_s, and z_s coordinate system associated with the body is <u>not</u> a co-rotating system with the body. Only the z_s axis is rigidly attached to the spinning body by always being in the direction of the spin rate vector $\vec{\Omega}$. The x_s and y_s axis remain fixed in inertial space as the body rotates, if no torques act on the body. If the body is acted on by external torques, the x_s and y_s axis will rotate as a function of the precession rate caused by the external torque. For cases in which the free stream velocity vector is

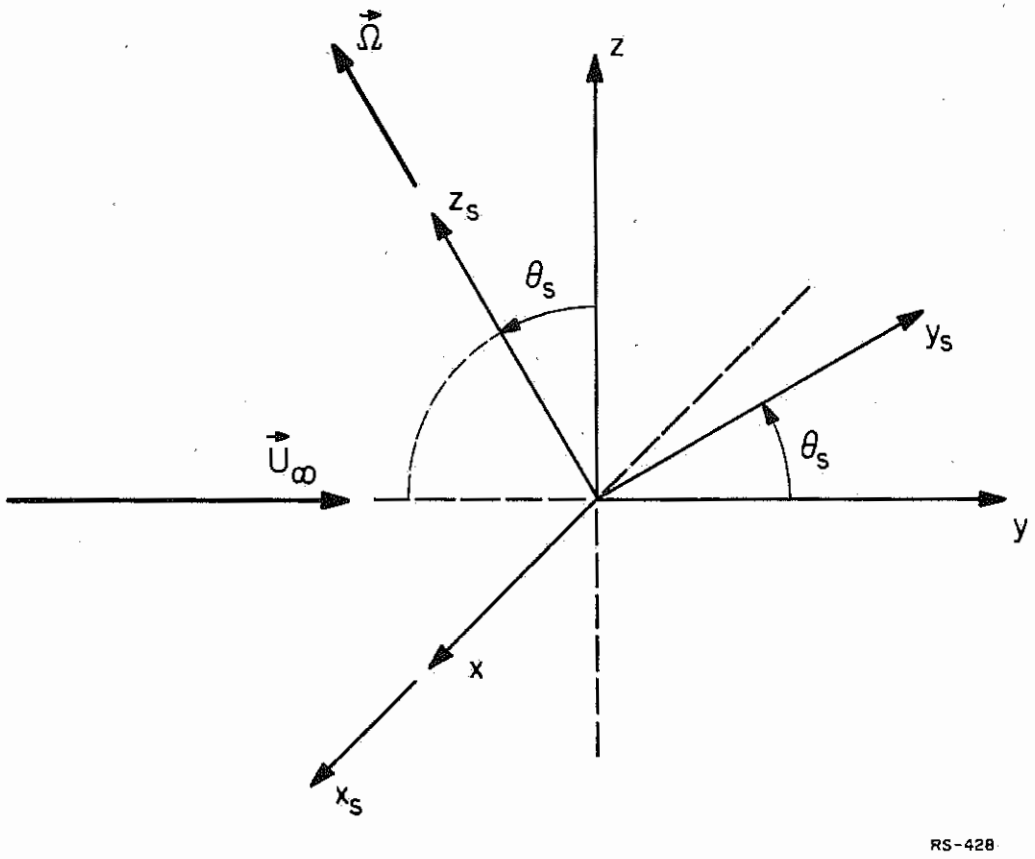

Figure 3.3. Orientation of body coordinate system with respect to system attached to the flow.

fixed in inertial space, the (x,y,z) system is an inertial system and the two coordinate systems are similar to those which would be set up for the classical top problem.[19] The case for which $\vec{U}_\infty$ rotates in inertial space (such as for a body in orbit) is taken into consideration in a later chapter by referring the results obtained using the coordinated systems defined above, by a coordinate transformation, to a true inertial reference.

The component of force in the y direction will be referred to as the drag component while the x and z components of force will be termed $(\text{lift})_x$ and $(\text{lift})_z$. In terms of the components of force on an element of surface, the vector force is given by

$$d\vec{F} = d(\text{lift})_x \, i + d(\text{drag}) \, j + d(\text{lift})_z \, k \qquad 3.22$$

where i,j,k are the unit vectors along the positive x,y,z axis. The differential notation is used to denote the vector force on the element of area, dA.

The vector torque is divided into components along the x_s,y_s, z_s axis. The component of torque along the z_s axis is termed slow-down torque, T_s. The x_s and y_s components of torque are perpendicular to the spin axis and are denoted by T_{i_s} and t_{j_s}. The vector torque $d\vec{T}$ is then given by

$$d\vec{T} = d(T_{i_s}) \, i_s + d(T_{j_s}) \, j_s + d(T_{k_s}) \, k_s \qquad 3.23$$

where i_s,j_s,k_s are the unit vectors along the positive x_s,y_s,z_s axis.

The surface element dA of the body is at a point defined by the radius vector $\vec{R}$ from the center of the coordinate systems. In the

subsequent development, cylindrical coordinates about the z_s axis are employed in which an angle ξ is defined as measured from the positive x_s axis to the projection of $\vec{R}$ onto the x_s-y_s plane (see Figure 3.4).

3.2.2. Spinning Disk at Angles of Attack

A disk spinning about the surface normal is in the class of body shapes for which Equation 3.19 is valid. Consider a circular disk of radius r_d with spin vector $\vec{\Omega}$ normal to the surface at the center of the disk. Figure 3.5 shows the disk with the centers of the coordinate systems, defined above, at the center of the disk. The following vectors are required to find the force and torque components acting on the disk. Referring to Figures 3.3, 3.4, and 3.5

$$\begin{aligned} \vec{U}_\infty &= U_\infty j = U_\infty \cos\theta_s j_s - U_\infty \sin\theta_s k_s \\ \vec{\Omega} &= \Omega\, k_s \\ \vec{R} &= r\cos\xi\, i_s + r\sin\xi\, j_s \\ \vec{n} &= k_s \end{aligned} \qquad 3.24$$

where r is the distance from the center of the disk to the surface element dA where dA is given by

$$dA = rdrd\xi \qquad 3.25$$

The angle θ must now be determined for use in C_j given by Equation 3.20 and S_j given by Equation 3.21. Since

$$\vec{U}\cdot\vec{n} = U\sin\theta \qquad 3.26$$

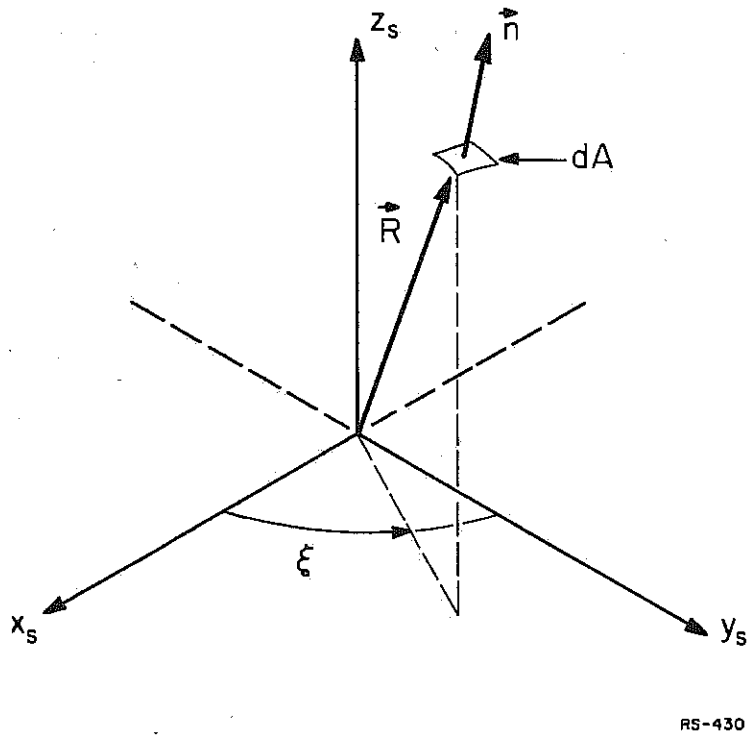

Figure 3.4. Orientation of surface element in the body coordinate system.

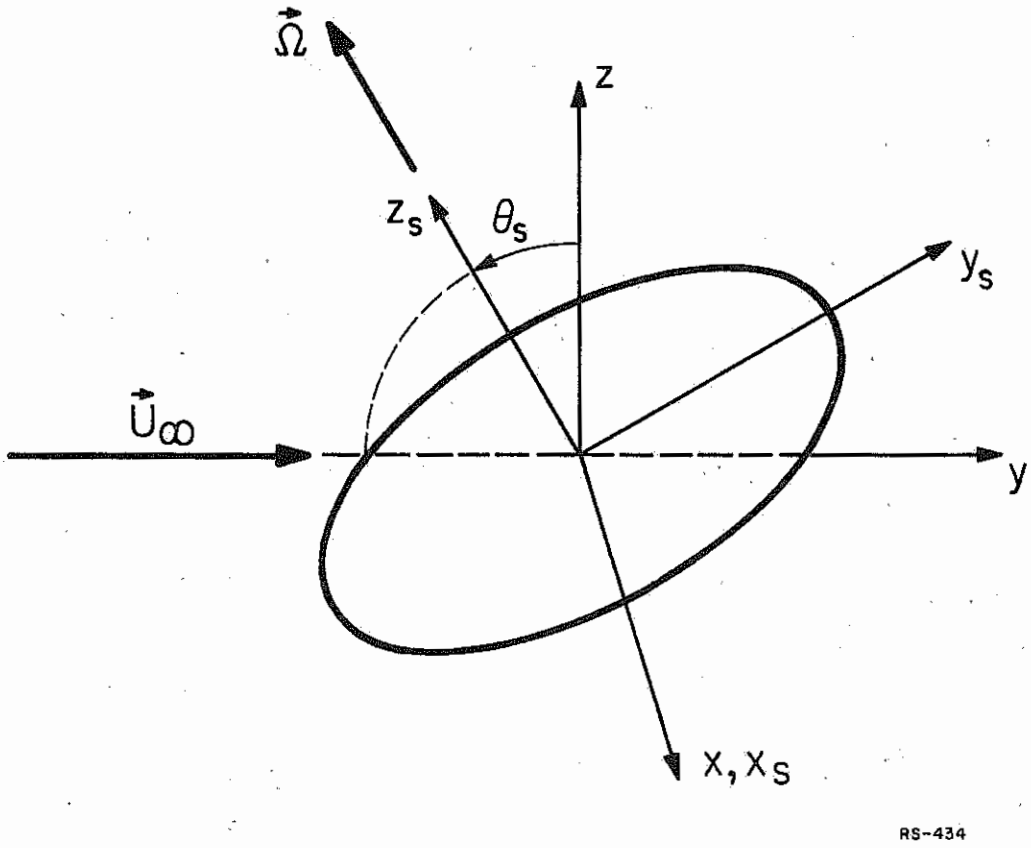

Figure 3.5. Spinning disk at angle of attack.

$$\theta = \sin^{-1}\left[\frac{\vec{U}\cdot\vec{n}}{U}\right] = \sin^{-1}\left[\frac{\vec{U}_\infty\cdot\vec{n}}{U}\right] \qquad 3.27$$

Using Equation 3.24, θ becomes

$$\theta = \sin^{-1}\left[\frac{U_\infty \sin\theta_s}{(U_\infty^2 + r^2\Omega^2 - 2U_\infty r\Omega \cos\xi \cos\theta_s)^{\frac{1}{2}}}\right] \qquad 3.28$$

Define a non-dimensional quantity, K_d, as the ratio of the peripheral speed of the disk to the free stream velocity, U_∞. That is, let

$$K_d = \frac{r_d\Omega}{U_\infty} \qquad 3.29$$

where r_d is the radius of the disk. Define, also, a non-dimensional variable r' as the ratio of the variable r to r_d. That is, let

$$r' = \frac{r}{r_d} \qquad 3.30$$

Using Equations 3.29 and 3.30 in Equation 3.28, θ becomes

$$\theta = \sin^{-1}\left[\frac{\sin\theta_s}{(1+K_d^2(r')^2 - 2K_d r' \cos\xi \cos\xi)^{\frac{1}{2}}}\right] \qquad 3.31$$

Substituting Equations 3.24, 3.25, and 3.30 into Equation 3.19 for $d\vec{F}$ and taking components along the x,y,z axis, the following results are obtained

$$d(\text{drag}) = D_d\, dr'\, d\xi \left[r'(1-C_j) - K_d(r')^2 \cos\theta_s \cos\xi\,(1-C_j) + r' \sin^2\theta_s\,(C_j + S_j)\right] \qquad 3.32$$

$$d(\text{lift}_z) = D_d\, dr'\, d\xi \left[-K_d(r')^3 \cos\xi \sin\theta_s\,(1-C_j) - r' \sin\theta_s \cos\theta_s\,(C_j + S_j)\right] \qquad 3.33$$

$$d(\text{lift}_x) = D_d \, dr' \, d\xi \, [K_d (r')^2 \sin \xi \, (1-C_j)] \qquad 3.34$$

where

$$D_d = \rho U_\infty^2 \sin \theta_s \, r_d^2$$

$$C_j = \sigma_j \sqrt{1-\alpha_j} \, \frac{\cos \theta_j}{\cos \theta}$$

$$S_j = \sigma_j \sqrt{1-\alpha_j} \, \frac{\sin \theta_j}{\sin \theta}$$

and where θ is defined by Equation 3.31

Similarly, the components of torque are obtained, given by

$$d(T_{i_s}) = D_d \, r_d \, dr' \, d\xi \, [-(r')^2 \sin \xi \sin \theta_s \, (1+S_j)] \qquad 3.35$$

$$d(T_{j_s}) = D_d \, r_d \, dr' \, d\xi \, [(r')^2 \cos \xi \cos \theta_s \, (1+S_j)] \qquad 3.36$$

$$d(T_{k_s}) = D_d \, r_d \, dr' \, d\xi \, [(r')^2 \cos \xi \cos \theta_s \, (1-C_j) - K_d (r')^3 (1-C_j)] \qquad 3.37$$

where D_d, C_j, S_j, and θ are as defined above.

Equations 3.31 through 3.37 are the basic equations expressing the force and torque on a spinning or non-spinning disk. In chapter 4, these equations will be evaluated for specific cases of the gas-surface interaction model.

3.2.3. Spinning Cylinder at Angles of Attack

The orientation of the spinning cylinder with respect to the x,y,z and x_s,y_s,z_s coordinate systems is shown in Figure 3.6. The cylinder of length L is spinning about the axis of the cylinder. The center of the coordinate system is placed at the geometric center of the cylinder. The

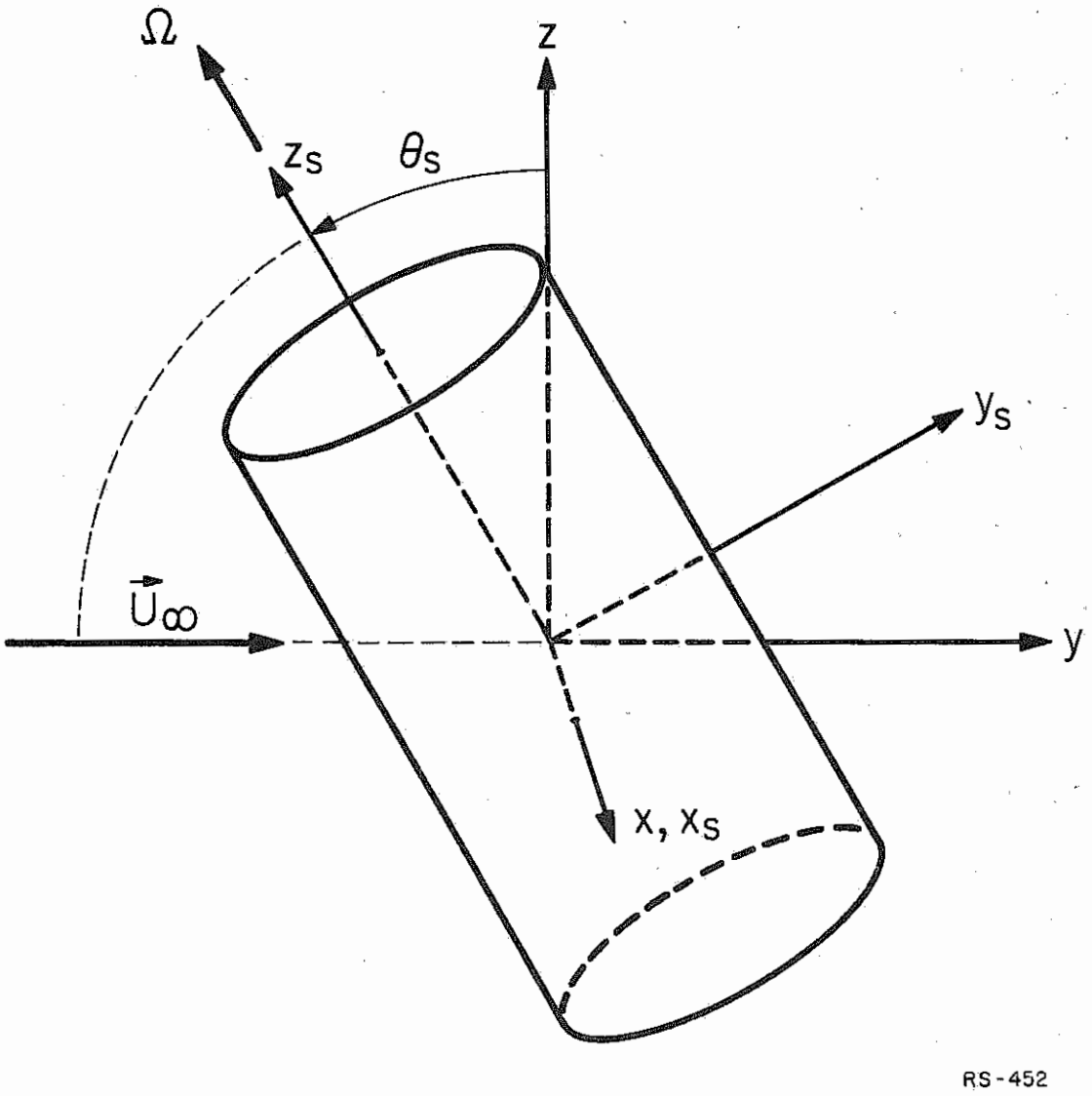

Figure 3.6. Spinning cylinder at angle of attack.

following vectors are defined

$$\vec{U}_\infty = U_\infty \cos\theta_s j_s - U_\infty \sin\theta_s k_s$$

$$\vec{\Omega} = \Omega k_s$$

$$\vec{R} = r_{cy} \cos\xi\, i_s + r_{cy} \sin\xi\, j_s + \ell k_s \qquad 3.38$$

$$\vec{n} = \cos\xi\, i_s + \sin\xi\, j_s$$

where r_{cy} is the radius of the cylinder and ℓ is the variable of integration along the axis of the cylinder. The element of surface dA is given by

$$dA = r_{cy}\, d\xi\, d\ell \qquad 3.39$$

From Equations 3.38, the angle θ is found to be

$$\theta = \sin^{-1} \frac{-\cos\theta_s \sin\xi}{(1+K_{cy}^2 - 2K_{cy}\cos\xi\cos\theta_s)^{\frac{1}{2}}} \qquad 3.40$$

where the non-dimensional spin-rate parameter K_{cy} is defined as

$$K_{cy} = \frac{r_{cy}\,\Omega}{U_\infty} \qquad 3.41$$

The variable of integration ℓ appears only in Equation 3.39 above. The equations for the cylinder can then immediately be integrated with respect to ℓ from $-\frac{L}{2}$ to $+\frac{L}{2}$. The variable ξ still remains, however. Letting

$$D_{cy} = \rho U_\infty^2\, r_{cy}\, L \cos\theta_s,$$

The resulting basic equations for the cylinder are found to be

$$d(\text{drag}) = D_{cy}\, d\xi\Big[-\sin\xi\,(1-C_j) + K_{cy}\cos\theta_s \sin\xi\cos\xi\,(1-C_j) - \cos^2\theta_s \sin^3\xi\,(C_j + S_j)\Big] \quad 3.42$$

$$d(\text{lift})_z = D_{cy}\, d\xi\Big[K_{cy}\sin\theta_s\cos\xi\sin\xi\,(1-C_j) - \cos\theta_s \sin\theta_s \sin^3\xi\,(C_j + S_j)\Big] \quad 3.43$$

$$d(\text{lift})_x = D_{cy}\, d\xi\Big[-K_{cy}\sin^2\xi\,(1-C_j) - \cos\theta_s\cos\xi\sin^2\xi\,(C_j + S_j)\Big] \quad 3.44$$

$$d(T_{js}) = D_{cy}\, r_{cy}\, d\xi\Big[\sin\theta_s \sin^2\xi\,(1-C_j)\Big] \quad 3.45$$

$$d(T_{j_s}) = D_{cy}\, r_{cy}\, d\xi\Big[\sin\theta_s\cos\xi\sin\xi\,(1-C_j)\Big] \quad 3.46$$

$$d(T_{ks}) = D_{cy}\, r_{cy}\, d\xi\Big[K_{cy}\sin\xi\,(1-C_j) + \cos\theta_s\cos\xi\sin\xi\,(1-C_j)\Big] \quad 3.47$$

where C_j and S_j are as defined previously.

The surface of the cylinder exposed to the flow is from $\xi = \pi$ to 2π at all angles of attack except $\theta_s = \frac{\pi}{2}$ and $-\frac{\pi}{2}$ where none of the surface is in the flow. Equations 3.42 - 3.47 are the basic expressions for force and torque on a spinning or non-spinning cylinder. These equations will be evaluated in chapter 4 for specific cases of the reflection model.

3.2.4. Spinning Cone at Angles of Attack

A cone having half angle δ, height H_c, and base radius r_c, is shown oriented in the x,y,z and x_s,y_s,z_s, coordinate systems in Figure 3.7. The center of the coordinate system is at the center of the base of the

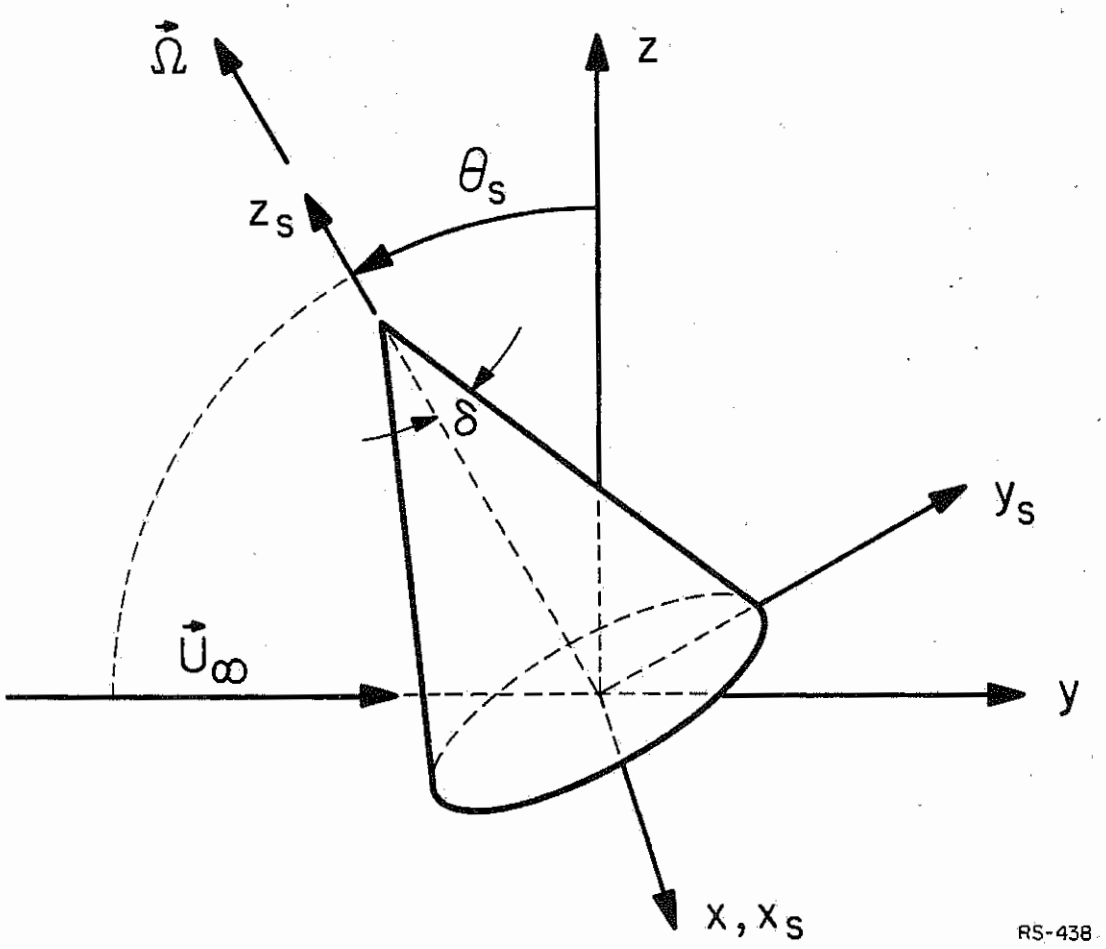

Figure 3.7. Spinning cone at angle of attack.

cone. The cone is spinning about the axis of the cone. The following vectors are defined

$$\vec{U}_\infty = U_\infty \cos \theta_s \, j_s - U_\infty \sin \theta_s \, k_s$$

$$\vec{\Omega} = k_s$$

$$\vec{R} = f(\ell) \cos \xi \, i_s + f(\ell) \sin \xi \, j_s + \ell \, k_s$$

$$\vec{n} = \cos \xi \cos \delta \, i_s + \sin \xi \cos \delta \, j_s + \sin \delta \, k_s \qquad 3.48$$

where ℓ is the variable of integration along the axis of the cone and $f(\ell)$ is the radial distance of the surface dA from the axis of the cone. The distance $f(\ell)$ is given by

$$f(\ell) = \frac{H_c - \ell}{H_c} \, r_c$$

The element of surface dA is given by

$$dA = \frac{f(\ell)}{\cos \delta} \, d\xi \, d\ell$$

The angle θ is found, using Equation 3.48, to be given by

$$\sin \theta = \frac{\sin \theta_s \sin \delta - \cos \theta_s \sin \xi \cos \delta}{(1 + (\ell')^2 K_c^{\,2} - 2\ell' K_c \cos \xi \cos \theta_s)^{\frac{1}{2}}} \qquad 3.49$$

where K_c is the non-dimensional spin rate parameter defined as

$$K_c = \frac{r_c \, \Omega}{U_\infty}$$

and ℓ' is a non-dimensional variable defined as

$$\ell' = 1 - \frac{\ell}{H_c}$$

Letting

$$D_c = \rho U_\infty^2 \frac{r_c^2}{\sin \delta}$$

The basic equations for the cone become

$$d(\text{drag}) = D_c \, d\xi \, d\ell' \left[-\ell' \chi (1 - C_j) + \chi K_c (\ell')^2 \cos \xi \cos \theta_s (1 - C_j) - \chi^3 \ell' (C_j + S_j) \right] \quad 3.50$$

$$d(\text{lift})_z = D_c \, d\xi \, d\ell' \left[\chi K_c (\ell')^2 \cos \xi \sin \theta_s (1 - C_j) - \chi^2 \ell' (\sin \delta \cos \theta_s + \sin \xi \cos \delta \sin \theta_s)(C_j + S_j) \right] \quad 3.51$$

$$d(\text{lift})_x = D_c \, d\xi \, d\ell' \left[-\chi K_c (\ell')^2 \sin \xi (1 - C_j) - \chi^2 \cos \xi \cos \delta \, \ell' (C_j + S_j) \right] \quad 3.52$$

$$d(T_{i_s}) = D_c r_c \, d\xi \, d\ell' \left[\chi (\ell')^2 \sin \theta_s \sin \xi (1 - C_j) + \chi \ell' (1 - \ell') \cot \delta \cos \theta_s (1 - C_j) - \chi K_c (\ell')^2 (1 - \ell') \cot \delta \cos \xi (1 - C_j) + \chi^2 \{ -(\ell')^2 \sin \delta \sin \xi + \ell' (1 - \ell') \cot \delta \sin \xi \cos \delta \} (C_j + S_j) \right] \quad 3.53$$

$$d(T_{j_s}) = D_c r_c \, d\xi \, d\ell' \left[-\chi K_c (\ell')^2 (1 - \ell') \cot \delta \sin \xi (1 - C_j) - \chi (\ell')^2 \sin \theta_s \cos \xi (1 - C_j) - \chi^2 \ell' (1 - \ell') \cot \delta \cos \xi \cos \delta (C_j + S_j) + \chi^2 (\ell')^2 \sin \delta \cos \xi (C_j + S_j) \right] \quad 3.54$$

$$d(T_{k_s}) = D_c r_c \, d\xi \, d\ell' \left[(\chi K_c (\ell')^3 - \chi(\ell')^2 \cos\theta_s \cos\xi)(1-C_j) \right] \quad 3.55$$

where

$$\chi = \cos\theta_s \sin\xi \cos\delta - \sin\theta_s \sin\delta \quad 3.56$$

The surface of the cone exposed to the flow is a function of the angles θ_s and δ. At $\theta_s = \frac{\pi}{2}$, for example, the entire conical surface is exposed to the flow ($\xi = 0 \rightarrow 2\pi$). In fact, for all values of θ_s between $\frac{\pi}{2}$ and $\frac{\pi}{2} - \delta$, the entire conical surface is exposed to the flow. At angles of θ_s between $\left(-\frac{\pi}{2} + \delta\right)$, decreasing amounts of the conical surface is exposed to the flow. The shadow boundary for the flow on the surface is always a straight line and can be found in terms of the variable, ξ, by finding where $\vec{U}\cdot\vec{n} = 0$. Define the angle, β, to be the value of ξ at the shadow boundary. Then,

$$\beta = \sin^{-1}(\tan\theta_s \tan\delta) \quad 3.57$$

From Equation 3.57, the following three categories of surface exposure are defined.

Case I: $\tan\theta_s \tan\delta = 1$

Entire conical surface ($\xi = 0 \rightarrow 2\pi$) is exposed to the flow.

Case II: $-1 \leq \tan\theta_s \tan\delta \leq 1$

Only part of the conical surface

$$\xi = (\pi - \beta) \rightarrow (2\pi + \beta)$$

is exposed to the flow.

Case III: $\tan\theta_s \tan\delta \leq -1$

No part of the conical surface is exposed to the flow. (The base of the cone having not been included in the basic equations for the cone).

3.2.5. Spinning Sphere at Angles of Attack

A sphere of radius r_s is shown oriented with respect to the x,y,z and x_s, y_s, z_s coordinate systems in Figure 3.8. The spin axis is along a diameter of the sphere at an angle $(\frac{\pi}{2}-\theta_s)$ with respect to the free stream velocity. Cylindrical coordinates are used to describe the position of the surface element dA. With ℓ denoting the variable length along the spin axis, dA is given by

$$dA = r_s \, d\xi \, d\ell$$

The following vectors are defined

$$\vec{U}_\infty = U_\infty \cos\theta_s \, j_s - U_\infty \sin\theta_s \, k_s$$

$$\vec{\Omega} = \Omega \, k_s$$

$$\vec{R} = r(\ell) \cos\xi \, i_s + r(\ell) \sin\xi \, j_s + \ell k_s \qquad 3.58$$

$$\vec{n} = \frac{r(\ell)}{r_s} \cos\xi \, i_s + \frac{r(\ell)}{r_s} \sin\xi \, j_s + \frac{\ell}{r_s} k_s$$

where $r(\ell)$ is the radial distance from the spin axis at the point ℓ to the element of surface dA

$$r(\ell) = \left(r_s^2 - \ell^2\right)^{\frac{1}{2}} \qquad 3.59$$

The angle θ is obtained from Equations 3.58 as

$$\sin\theta = \frac{\ell' \sin\theta_s - \ell_s \sin\xi \cos\theta_s}{\left(1+\ell_s^2 K_s^2 - 2K_s \ell_s \cos\xi \cos\theta_s\right)^{\frac{1}{2}}} \qquad 3.60$$

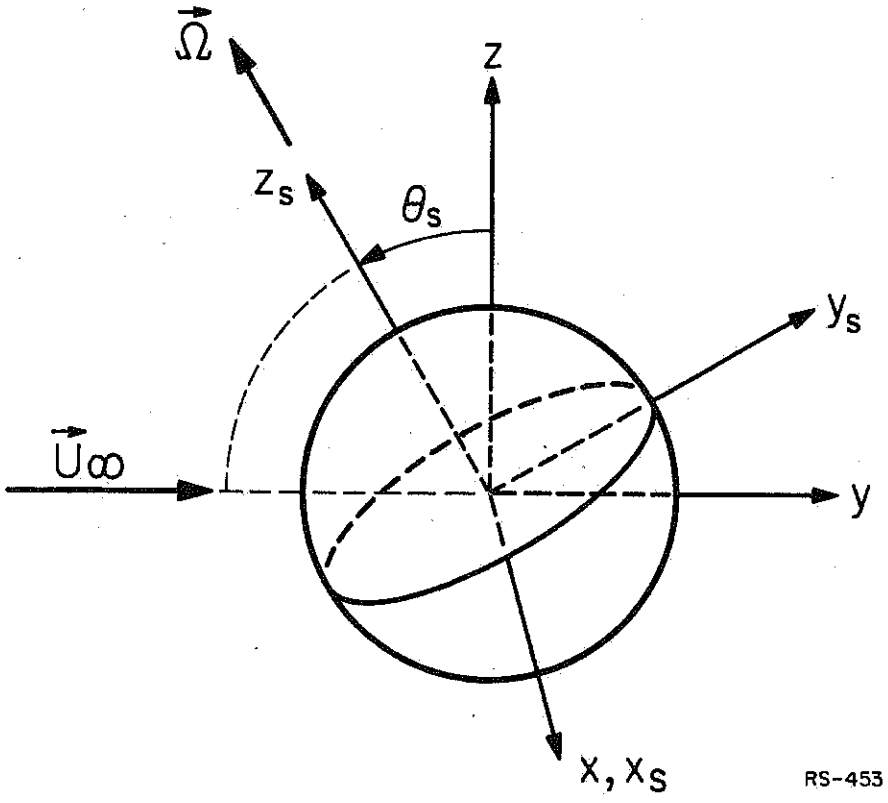

Figure 3.8. Spinning sphere at angle of attack.

where K_s is the non-dimensional spin-rate parameter defined as

$$K_s = \frac{r_s \Omega}{U_\infty}$$

and ℓ' is a non-dimensional variable of integration defined as

$$\ell' = \frac{\ell}{r_s}$$

and

$$\ell_s = [1-(\ell')^2]^{\frac{1}{2}}$$

Letting

$$D_s = \rho\, U_\infty^{\,2}\, r_s^{\,2}$$

The basic equation for the sphere becomes

$$d(\text{drag}) = D_s\, d\xi\, d\ell' \,[\chi_s\, (-1 + K_s\, \ell_s \cos\xi \cos\theta_s)(1-C_j) - \chi_s^{\,3}\, (C_j+S_j)] \qquad 3.61$$

$$d(\text{lift}_z) = D_s\, d\xi\, d\ell' \,[\chi_s k_s \ell_s \cos\xi \sin\theta_s\, (1-C_j) - \chi_s^{\,2}\, (\ell' \cos\theta_s + \ell_s \sin\xi \cos\theta_s)\, (C_j+S_j)] \qquad 3.62$$

$$d(\text{lift}_x) = D_s\, d\xi\, d\ell' \,[-\chi_s\, k_s\, \ell_s \sin\xi\, (1-C_j) - \chi_s^{\,2}\, \ell_s \cos\xi\, (C_j+S_j)] \qquad 3.63$$

$$d(T_{i_s}) = D_s\, r_s\, d\xi\, d\ell' \,[\ell_s \sin\theta_s \sin\xi - K_s\, \ell'\ell_s \cos\xi + \ell' \cos\theta_s]\, \chi_s\, (1-C_j) \qquad 3.64$$

$$d(T_{j_s}) = D_s\, r_s\, d\xi\, d\ell' \left[-\ell_s' \sin\theta_s \cos\xi - K_s\, \ell' \ell_s \sin\xi\right] \chi_s\, (1-C_j) \quad 3.65$$

$$d(T_{k_s}) = D_s\, r_s\, d\xi\, d\ell' \left[K_s\, \ell_s^2 - \ell_s \cos\xi \cos\theta_s\right] \chi_s\, (1-C_j) \quad 3.66$$

where

$$\chi_s = \ell_s \cos\theta_s \sin\xi - \ell' \sin\theta_s$$

The shadow line of the flow on the surface of the sphere is a curve in the ℓ' - ξ plane. At a constant ℓ', the shadow limits in terms of ξ can be found by finding where $\vec{U}\cdot\vec{n} = 0$. Define the angle β_s to be the value of ξ at the shadow boundary. Then, β_s is given by

$$\beta_s = \sin^{-1}\left(\tan\theta_s \frac{\ell'}{\ell_s}\right)$$

For arbitrary values of θ_s, the shadow determines three regions of exposure along the spin axis. Referring to Figure 3.9

$$\underline{\text{Region I}}: \quad \tan\theta_s \frac{\ell'}{\ell_s} \geq 1$$

In this region the surface from $\xi = 0$ to $\xi = 2\pi$ is exposed to the flow

$$\underline{\text{Region II}}: \quad -1 \leq \tan\theta_s \frac{\ell'}{\ell_s} \leq 1$$

In this region the shadow limits are, at any point, ℓ', from $\xi = \pi - \beta_s$ to $\xi = 2\pi + \beta_s$.

$$\underline{\text{Region III}}: \quad \tan\theta_s \frac{\ell'}{\ell_s} \leq -1$$

This region of the sphere is not exposed to the flow.

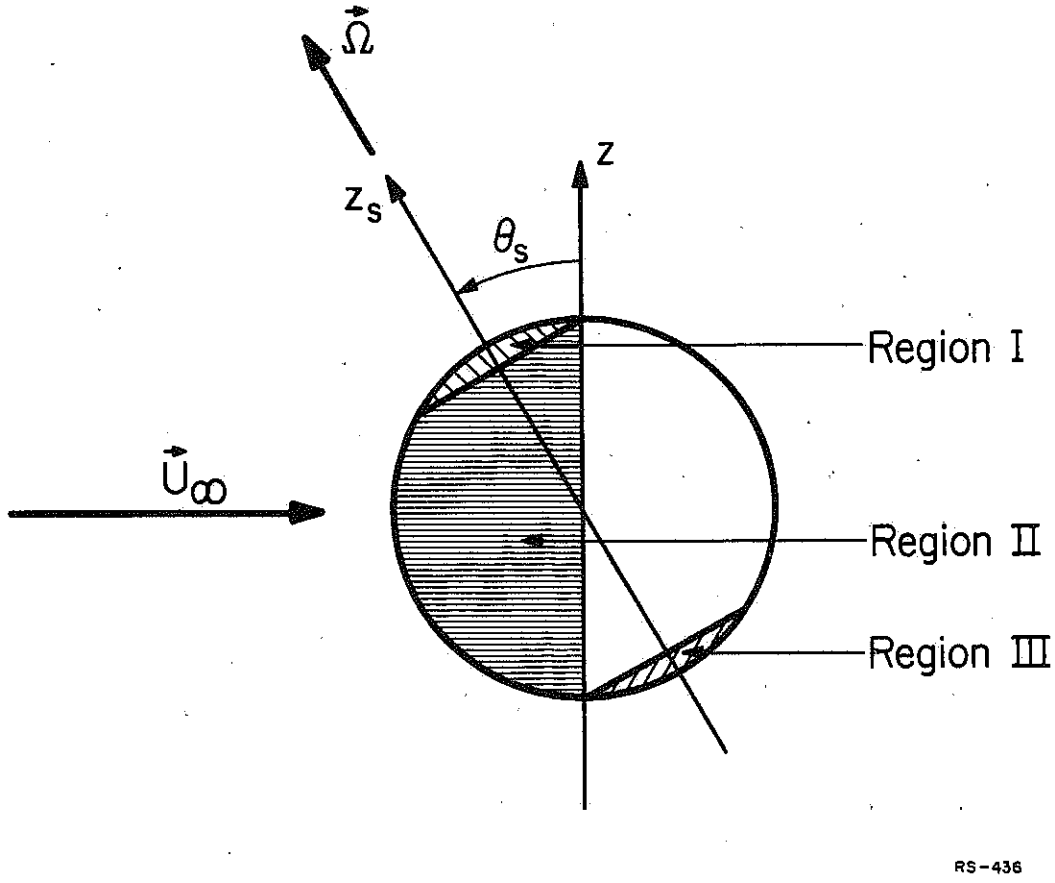

Figure 3.9. Regions of sphere surface exposed to the flow.

3.3. Applications

The equations which have been obtained for the four basic shapes of the disk, cylinder, cone, and sphere are applicable to a wide variety of problems. In the next chapters these equations will be used to evaluate the effects of spin rate and the gas surface interaction on the dynamic properties of these shapes in free molecular flow. The application of the equations to other problems is discussed as follows.

Many satellite shapes can be simulated by a combination of the four basic shapes of the disk, cylinder, cone, and sphere. If the satellite is of convex shape, the basic equations developed in this chapter can be applied directly. Since the equations are in differential form, they are equally applicable to bodies composed of segments of the sphere (such as spherical caps), cone frustrums and segments of the cylinder and disk.

Surface properties affect the character of the gas-surface interaction. Many satellites are composed of surfaces which have widely differing surface properties such as solar cells versus painted surfaces and varying surface temperature or roughness. Problems of this type can be studied using the equations developed in this chapter by assigning different values to the parameters of the gas-surface interaction model for a specific region of the surface.

4. AERODYNAMIC PROPERTIES OF SELECTED SHAPES

In this chapter aerodynamic properties of selected shapes are evaluated from the expressions developed in chapter 3. For the special case of the Maxwell model, results are obtained to illustrate the effects of spin on the aerodynamic properties of the four basic shapes of disk, cylinder, cone, and sphere. Analytical results are also obtained in terms of the generalized model parameters for drag of the four body shapes with zero spin.

In general, the aerodynamic properties must be evaluated by using numerical methods. The numerical techniques employed in this study are outlined in this chapter and results obtained for various values of the generalized model parameters are presented. These results are compared with those obtained for the special case of the Maxwell model.

In the next chapter, the results obtained for the cone and disk are applied to the problem of a satellite in near earth orbit.

4.1. Special Case of the Maxwell Model

The reduction of the generalized gas-surface interaction model parameters to the parameters of the Maxwell model was demonstrated in section 2.3.1. Those results can be applied to determining in terms of the Maxwell model parameters the quantities C_j and S_j which appear in the basic aerodynamic equations developed in chapter 3. For specular reflection,

$$C_j = \sigma_j\sqrt{1-\alpha_j}\ \frac{\cos\theta_j}{\cos\theta} = 1 - \alpha_d$$
$$S_j = \sigma_j\sqrt{1-\alpha_j}\ \frac{\sin\theta_j}{\sin\theta} = 1 - \alpha_d \qquad 4.1$$

For diffuse reflection,

$$C_j = 0$$

$$S_j = \alpha_d\sqrt{1-\alpha_T}\ \frac{1}{\sin\theta}$$

Combining diffuse and specular reflection, the values of C_j and S_j in terms of the parameters of the Maxwell model become

$$(C_j)_m = 1 - \alpha_d$$

$$(S_j)_m = 1 - \alpha_d + \alpha_d\sqrt{1-\alpha_T}\ \frac{1}{\sin\theta} \qquad 4.2$$

In the basic aerodynamic equations, the following functions of C_j and S_j occur repeatedly. In terms of the Maxwell model parameters, these functions are given as

$$1 - (C_j)_m = \alpha_d$$

$$(C_j)_m + (S_j)_m = 2(1-\alpha_d) + \alpha_d\sqrt{1-\alpha_T}\ \frac{1}{\sin\theta} \qquad 4.3$$

$$1 + (S_j)_m = 2 - \alpha_d + \alpha_d\sqrt{1-\alpha_T}\ \frac{1}{\sin\theta}$$

The equations for the disk, cylinder and cone could be integrated analytically except for the terms containing $(\sin\theta)^{-1}$ which appear in Equations 4.3.

The angle of incidence of the flow, θ, is a function of the spin-rate and position of the surface element dA as discussed in chapter 3. For the four body shapes studies, the expressions found in chapter 3 for $\sin\theta$ for each shape are all of the following form

$$\sin \theta = A \left[1 + K^2 d^2 - 2Kd \cos \xi \cos \theta_s\right]^{-\frac{1}{2}} \qquad 4.4$$

where Table 4.1 gives the values for A, K, and d for the four shapes studied in chapter 3. The terms K and d are non-dimensional where d represents, except of the case of the cylinder, a variable of integration which may have a maximum value of one or less. The spin rate parameter K is the ratio of the maximum peripheral velocity of the body to the free stream velocity U_∞. For satellite applications, K is always less than one as can be determined from the values for K given in Table 4.2 for a number of past satellites.

Since $K < 1$ and $d \leq 1$ for satellite applications,

$$(K^2 d^2 - 2Kd \cos \theta_s \cos \xi)^2 < 1 \qquad 4.5$$

and $(\sin \theta)^{-1}$ can be expanded in a binomial series as an approximation to the dependence of θ on spin rate and surface position. The result of the expansion is

$$(\sin \theta)^{-1} \approx \frac{1}{A} \left[1 - Kd \cos \theta_s \cos \xi + \frac{1}{2} (Kd)^2 (1 - \cos^2 \theta_s \cos^2 \xi) + O(Kd)^3\right] \qquad 4.6$$

where terms of order $(Kd)^3$ and higher are not to be retained. Substituting Equation 4.6 into Equation 4.2 for C_j and S_j of the Maxwell model, the following results are obtained

$$\begin{aligned} (C_j)_m &= 1 - \alpha_d \\ (S_j)_m &= 1 - \alpha_d + \alpha_d \sqrt{1-\alpha_T}\, A^{-1} \left[1 - Kd \cos \theta_s \cos \xi + \tfrac{1}{2} (Kd)^2 (1 - \cos^2 \theta_s \cos^2 \xi)\right] \end{aligned} \qquad 4.7$$

Equations 4.7 will now be substituted into the basic aerodynamics equations

Table 4.1.

Definitions of A, K, and d obtained from the results of chapter 3

Body Shape	A	K	d
disk	$\sin \theta_s$	$K_d = \frac{r_d \Omega}{U_\infty}$	$r' = \frac{r}{r_d}$
cylinder	$-\cos \theta_s \sin \xi$	$K_{cy} = \frac{r_{cy} \Omega}{U_\infty}$	1
cone	$\sin \theta_s \sin \delta - \cos \theta_s \sin \xi \cos \delta$	$K_c = \frac{r_c \Omega}{U_\infty}$	$\ell' = 1 - \frac{\ell}{H_c}$
sphere	$\ell' \sin \theta_s - \ell_s \sin \xi \cos \theta_s$	$K_s = \frac{r_s \Omega}{U_\infty}$	$\ell_s = (1 - \frac{\ell^2}{r_s^2})^{\frac{1}{2}}$

Table 4.2.

Values of the spin rate parameter, K, for a number of past satellites

Satellite	Orbit Altitude[20] perigee - apogee (mi)	Spin rate[20] (rpm)	K (10^{-3})
ESRO 2A	215 - 680	35	.350 - .519
ESRO 2B	205 - 677	35	.151 - .223
IDSCS 19-26	20,940 - 21,068	150	2.29
ERS 16	110 - 2,260	10	.0197 - .0301
ERS 18 and OV5-1	5,357 - 69,316	10	.0306 - .238
OSO 3	336 - 354	30	.230
Explorer 32	173 - 1,629	30	.169 - .227
ESSA 1	432 - 521	10	.074 - .079
ESSA 2	843 - 885	10.9	.084 - .086
ESSA 4	822 - 894	10	.078
ESSA 6	876 - 925	10	.078

obtained in chapter 3. For the disk, cylinder, and cone, analytical results can be obtained. The equations of chapter 3 expressing force and torque on a spinning sphere are not integrable in closed form when Equations 4.7 are employed; however, the torque on a spinning sphere has been obtained analytically in terms of the Maxwell model parameters by using the techniques employed in Reference 9. The results from Reference 9 for the sphere will be given along with the results for drag of a non-spinning sphere which can be obtained analytically from the equations given in chapter 3.

The results will be presented in terms of coefficients of drag, lift, and torque, which are defined as follows.

$$\text{Drag coefficient} = C_D = \frac{\text{Drag}}{\frac{1}{2}\rho U_\infty^2 \bar{A}}$$

$$\text{Lift coefficient} = C_L = \frac{\text{Lift}}{\frac{1}{2}\rho U_\infty^2 \bar{A}}$$

$$\text{Torque coefficient} = C_T = \frac{\text{Torque}}{\frac{1}{2}\rho U_\infty^2 \bar{A}\, \bar{r}}$$

where $\bar{A}$ is a reference area associated with the particular shape being studied. In addition, a reference radius $\bar{r}$ is introduced in the expressions for coefficients of torque.

4.1.1. Spinning Disk Properties in Terms of The Maxwell Model Parameters

Substituting Equations 4.7 for the Maxwell model into Equations 3.32 through 3.37 for the spinning disk at angles of attack and integrating over r' and ξ (0 to 1 for r' and 0 to 2π for ξ) the following results are

obtained for the case of the spinning disk, ($\bar{A} = \pi r_d^2$, $\bar{r} = r_d$))

$$C_D = 2 \sin\theta_s \{2 \sin^2\theta_s + \alpha_d (1 - 2 \sin^2\theta_s) + \alpha_d\sqrt{1-\alpha_T} \sin\theta_s [1 + \frac{K_d^2}{8} (1 + \sin^2\theta_s)]\} \quad 4.8$$

$$C_{L_z} = 2 \sin\theta_s \{-2 \sin\theta_s \cos\theta_s + 2 \alpha_d \sin\theta_s \cos\theta_s - \alpha_d\sqrt{1-\alpha_T} \cos\theta_s [1 + \frac{K_d^2}{8} (1 + \sin^2\theta_s)]\} \quad 4.9$$

$$C_{L_x} = 0 \quad 4.10$$

$$C_{T_{i_s}} = 0 \quad 4.11$$

$$C_{T_{j_s}} = - (\alpha_d\sqrt{1-\alpha_T} K_d \sin\theta_s \cos\theta_s)/2 \quad 4.12$$

$$C_{T_{k_s}} = - \alpha_d K_d \sin\theta_s \quad 4.13$$

A spinning disk is found to have drag and $(\text{lift})_z$ coefficients which are higher than a disk with zero spin rate. This increase in drag is proportional to K_d^2 which would be small for satellites.

Besides the expected slowdown torque, a spin induced precession torque about the y_s-axis is obtained which is directly proportioned to K_d. The precession torque arises because diffusely reflected modules are reflected at a velocity relative to the surface which is higher on one half of the disk when the disk has angles of attack other than $\frac{\pi}{2}$ and zero.

4.1.2. Spinning Cylinder Properties in Terms of Maxwell Model Parameters

The coefficients of drag, lift and torque for the spinning

cylinder at angles of attack are obtained by first substituting Equations 4.7 for the Maxwell model into Equation 3.42 through 3.47 for the cylinder. These equations are then integrated over the surface area exposed to the flow with respect to ξ from π to 2π. Letting $\bar{A} = 2\, r_{cy}\, L$ and $\bar{r} = r_{cy}$ the coefficient of drag, lift, and torque for the spinning cylinder at angles of attack are found to be

$$C_D = \cos\theta_s \left\{\frac{8}{3}\cos^2\theta_s + \alpha_d \frac{8}{3}\left(3/4 - \cos^2\theta_s\right) + \frac{\pi}{2}\alpha_d\sqrt{1-\alpha_T}\cos\theta_s\left[1 + \frac{K_{cy}^2}{8}\left(4 - \cos^2\theta_s\right)\right]\right\} \quad 4.14$$

$$C_{L_z} = \cos\theta_s \left\{\frac{8}{3}\cos\theta_s \sin\theta_s - \alpha_d \frac{8}{3}\cos\theta_s \sin\theta_s + \frac{\pi}{2}\alpha_d\sqrt{1-\alpha_T}\sin\theta_s\left[1 + \frac{K_{cy}^2}{8}\left(4 - \cos^2\theta_s\right)\right]\right\} \quad 4.15$$

$$C_{L_x} = \cos\theta_s\, K_{cy}\left[-\frac{\pi}{2}\alpha_d + \frac{2}{3}\alpha_d\sqrt{1-\alpha_T}\cos\theta_s\right] \quad 4.16$$

$$C_{T_{i_s}} = \frac{\pi}{2}\alpha_d \sin\theta_s \cos\theta_s \quad 4.17$$

$$C_{T_{i_s}} = 0 \quad 4.18$$

$$C_{T_{k_s}} = -2\, K_{cy}\, \alpha_d \cos\theta_s \quad 4.19$$

The results obtained for the cylinder exhibit the same influence of spin rate on drag, lift and slowdown torque as those of the disk. Unlike the spinning disk, the spinning cylinder experiences a spin induced lift in the negative x direction which is directly proportional to the spin rate parameter K_{cy}. This spin induced lateral force on the cylinder is analogous

to a similar effect called the Magnus force which occurs on spinning cylinders in continuous flow (see Reference 21). In free molecular flow, the lateral force is found, however, to be in the direction opposite that of the analogous Magnus force.

The finite value of torque perpendicular to the spin axis obtained in Equation 4.17 is due entirely to geometry and is not spin induced as was found for the disk. The center of the surface area exposed to the flow is not at the geometric center of the cylinder but is a function of the angle of attack. If end contributions were included in the development of equations, $C_{T_{i_s}}$ would be zero.

4.1.3. Spinning Cone Properties in Terms of Maxwell Model Parameters

The coefficients of drag, lift, and torque for the spinning cone at angles of attack are obtained by substituting Equations 4.7 for the Maxwell model into Equations 3.30 through 3.56 for the cone. These equations can be integrated in general form by incorporating the angle β and integrating over the surface area exposed to the flow with respect to ℓ' from 0 to 1 and ξ from $(\pi - \beta)$ to $(2\pi + \beta)$. Letting $\bar{A} = \pi r_c^2$ and $\bar{r} = r_c$ the coefficient of drag, lift, and torque for the spinning cone at angles of attack are found to be

$$C_D = R_2 + \alpha_d \left[\frac{2}{\pi} \cos\theta_s \cot\delta \cos\beta + \frac{\pi+2\beta}{\pi} \sin\theta_s - R_2\right] + \alpha_d\sqrt{1-\alpha_T} \left[R_3 + \frac{K_c^2}{4}(R_3 - R_8 \cos^2\theta_s)\right] \qquad 4.20$$

$$C_{L_z} = -(1 - \alpha_d)\ (2R_3 \sin\delta \cos\theta_s + 2R_1 \cot\delta \sin\theta_s)$$
$$+ \alpha_d\sqrt{1-\alpha_T}\left[R_4 \cos\theta_s + R_5 \cot\delta \sin\theta_s\right.$$
$$+ \frac{K_c^2}{4}\left\{R_4 \cos\theta_s + R_5 \cos\delta \sin\theta_s\right.$$
$$\left.\left. - \cos^2\theta_s (R_7 + R_6)\right\}\right] \qquad 4.21$$

$$C_{L_x} = -K_c \frac{1}{3}\left[\alpha_d\ (\cos\theta_s \cot\delta \frac{\pi+2\beta-\sin 2\beta}{\pi} + \frac{4}{\pi}\sin\theta_s \cos\beta)\right.$$
$$\left. + 2\ \alpha_d\sqrt{1-\alpha_T}\ R_7 \cos\theta_s \cot\delta\right] \qquad 4.22$$

$$C_{T_{i_s}} = 2\ R_1 \frac{1-3\sin^2\delta}{3\sin^2\delta}$$
$$+ \alpha_d \frac{1}{3}\left[\frac{4}{\pi}\sin^2\theta_s \cos\beta - \frac{1}{\pi}\cos\theta_s \sin\theta_s \cot\delta \sin 2\beta\right.$$
$$\left. - \frac{2}{\pi}\cot^2\delta \cos^2\theta_s \cos\beta - 2R_1 \frac{1-3\sin^2\delta}{\sin^2\delta}\right]$$
$$- \alpha_d\sqrt{1-\alpha_T}\left[R_5\left(\frac{1-3\sin^2\delta}{3\sin^2\delta}\right)\right.$$
$$\left. + \frac{K_c^2}{4}\ (R_5 - \cos^2\theta_s\ R_6)\left(\frac{1-5\sin^2\delta}{5\sin^2 d}\right)\right] \qquad 4.23$$

$$C_{T_{j_s}} = -\frac{K_c}{12}\left[\alpha_d(\cot^2\delta \cos\theta_s \frac{\pi+2\beta\ -\ \sin 2\beta}{2\pi} + \frac{4}{\pi}\cot\delta \sin\theta_s \cos\beta)\right.$$
$$\left. + \alpha_d\sqrt{1-\alpha_T}\ 2R_7 \cos\theta_s \frac{1-4\sin^2\delta}{\sin^2\delta}\right] \qquad 4.24$$

$$C_{T_{K_s}} = -K_c\ \alpha_d\ (\frac{1}{\pi}\cos\theta_s \cot\delta \cos\beta + \frac{\pi+2\beta}{2\pi}\sin\theta_s) \qquad 4.25$$

The functions R_1, R_2, ---- R_8 used in Equations 4.20 through 4.25

are defined as follows.

$$R_1 = -\frac{2}{3\pi}\cos^2\theta_s\cos^2\delta\cos\beta\,(\sin^2\beta+2) - \frac{2}{\pi}\sin^2\theta_s\sin^2\delta\cos\beta - \sin\theta_s\cos\theta_s\sin\delta\cos\delta\,\frac{\pi+2\beta-\sin2\beta}{\pi}$$

$$R_2 = \frac{4}{3\pi}\cos^3\theta_s\cos^2\delta\cot\delta\cos\beta\,(\sin^2\beta+2) + 2\sin^3\theta_s\sin^2\delta\,\frac{\pi+2\beta}{\pi} + 3\sin\theta_s\cos^2\theta_s\cos^2\delta\,\frac{\pi+2\beta-\sin2\beta}{\pi} + \frac{12}{\pi}\sin^2\theta_s\cos\theta_s\sin\delta\cos\delta\cos\beta$$

$$R_3 = \cos^2\theta_s\cos\delta\cot\delta\,\frac{\pi+2\beta-\sin2\beta}{2\pi} + \frac{4}{\pi}\sin\theta_s\cos\theta_s\cos\delta\cos\beta + \sin^2\theta_s\sin\delta\,\frac{\pi+2\beta}{\pi}$$

$$R_4 = -\frac{2}{\pi}\cos\theta_s\cos\delta\cos\beta - \sin\theta_s\sin\delta\,\frac{\pi+2\beta}{\pi}$$

$$R_5 = \cos\theta_s\cos\delta\,\frac{\pi+2\beta-\sin2\beta}{2\pi} + \frac{2}{\pi}\sin\theta_s\sin\delta\cos\beta$$

$$R_6 = \cos\theta_s\cos\delta\,\frac{2\pi+4\beta-\sin4\beta}{16\pi} + \frac{2}{3\pi}\sin\theta_s\sin\delta\cos^3\beta$$

$$R_7 = -\frac{2}{3\pi}\cos\theta_s\cos\delta\cos^3\beta - \sin\theta_s\sin\delta\,\frac{\pi+2\beta+\sin2\beta}{2\pi}$$

$$R_8 = \cos^2\theta_s\cot\delta\cos\delta\,\frac{2\pi+4\beta-\sin4\beta}{16\pi} + \frac{4}{3\pi}\sin\theta_s\cos\theta_s\cos\delta\cos^3\beta + \sin^2\theta_s\sin\delta\,\frac{\pi+2\beta+\sin2\beta}{2\pi}$$

In Equations 4.20 through 4.25, the value of the angle β depends upon the angles θ_s and δ in accordance with the three cases of surface exposure defined in the last chapter for the cone. Using those definitions the following ranges of β are defined.

$$\begin{aligned} &\text{Case I:} && \tan\theta_s \tan\delta \geq 1 \\ &&& \beta = \frac{\pi}{2} \\ &\text{Case II:} && -1 \leq \tan\theta_s \tan\delta \leq 1 \\ &&& \beta = \sin^{-1}(\tan\theta_s \tan\delta) \\ &\text{Case III:} && \tan\theta_s \tan\delta \leq -1 \\ &&& \beta = -\frac{\pi}{2} \end{aligned} \qquad 4.26$$

For case III, the coefficients of drag, lift, and torque all become zero because the conical surface is shaded from the flow.

The cone equations are found to be similar in form to those obtained for the cylinder and disk. As in the case of the spinning cylinder, a spin induced lateral force is experienced by the spinning cone at angles of attack. The spin induced lateral force is found to be directly proportional to the spin rate parameter K_c.

The cone is found to also experience a spin induced torque, perpendicular to the spin-axis, about the y_s axis of the cone. The component of torque about the x_s axis is not spin induced but is instead due to the moment of the drag and $(\text{lift})_z$ forces about the center of the coordinate systems.

4.1.4. Spinning Sphere Properties in Terms of the Maxwell Model Parameters

The sphere equations given in the last chapter must in general be

evaluated by numerical techniques for all cases of the gas-surface interaction model. The equations given in chapter 3 are particularly useful when applied to shapes such as spinning spherical caps, and hemispheres. For the special case of a complete sphere, analytical solutions for the torque components are given in Reference 9. The results of Reference 9 will be given here and are the same as would be obtained by numerically solving Equations 3.61 through 3.66.

Letting $\bar{A} = \pi r_s^2$ and $\bar{r} = r_s$, the coefficients of torque on the sphere are as obtained in Reference 9,

$$C_{T_{i_s}} = 0 \qquad 4.27$$

$$C_{T_{j_s}} = (K_s \alpha_d \sin \theta_s \cos \theta_s)/2 \qquad 4.28$$

$$C_{T_{k_s}} = - K_s \alpha_d (2 + \cos^2 \theta_s)/2 \qquad 4.29$$

The coefficient of drag for a non-spinning sphere, in terms of the Maxwell model parameters, can be obtained analytically from the equations given in chapter 3. Letting $\bar{A} = \pi r_s^2$,

$$C_D = 2 + \frac{4}{3} \alpha_d \sqrt{1-\alpha_T}; \qquad K_s = 0 \qquad 4.30$$

The coefficients of drag and lift for the spinning sphere must be obtained by numerical integration techniques and are therefore not available in analytic form.

4.2. Solutions in Terms of the Generalized Model Parameters

4.2.1. Analytical Results (Zero Spin)

For the special case of zero spin rate, the equations of chapter 3 can be integrated in closed form for certain cases of angle of attack. These results are given in the following sections.

4.2.1.1. Drag and Lift of Flat Plate at Angles of Attack

The angle θ for the disk (Equation 3.31) becomes θ_s for the case when $K_d = 0$. Therefore,

$$C_j = \sigma_j \sqrt{1-\alpha_j} \; \frac{\cos\left(\frac{\pi}{2} P_j + (1-P_j)\,\theta_s\right)}{\cos \theta_s} \qquad 4.31$$

and

$$S_j = \sigma_j \sqrt{1-\alpha_j} \; \frac{\sin\left(\frac{\pi}{2} P_j + (1-P_j)\,\theta_s\right)}{\sin \theta_s} \qquad 4.32$$

which are independent of r' and ξ.

Substituting Equations 4.31 and 4.32 into Equations 3.32 through 3.37 for the disk with $K_d = 0$, the following results are obtained after integration over r' from 0 to 1 and ξ from 0 to 2π. Letting $\bar{A} = \pi r_d^2$

$$C_D = 2 \sin \theta_s - 2\sigma_j \sqrt{1-\alpha_j} \sin \theta_s \cos\left[\frac{\pi}{2} P_j + (2-P_j)\,\theta_s\right] \qquad 4.33$$

$$C_{L_z} = -2\,\sigma_j \sqrt{1-\alpha_j} \sin \theta_s \sin\left[\frac{\pi}{2} P_j + (2-P_j)\,\theta_s\right] \qquad 4.34$$

$$C_{L_x} = C_{T_{i_s}} = C_{T_{j_s}} = C_{T_{k_s}} = 0 \qquad 4.35$$

These equations can be shown to reduce to Equations 4.8 through 4.13 obtained for the disk in terms of the Maxwell model parameters by letting $K_d = 0$ and substituting the appropriate terms for σ_j, α_j, and P_j. Since the repeated subscripts imply the summation over the J beam components, Equation 4.34 for example could be written

$$C_{L_z} = -2 \sin \theta_s \sum_{j=1}^{J} \{\sigma_j \sqrt{1-\alpha_j} \sin (\theta_j + \theta_s)\}$$

where $\sum_{j=1}^{J} \sigma_j = 1$.

In Equations 4.33 and 4.34, the first approximation to θ_j has been utilizied.

4.2.1.2 Drag of Cylinder with Axis Perpendicular to Flow

In the cylinder equations of chapter 3, the angle θ, given by Equations 3.40, becomes if $K_{cy} = 0$,

$$\sin \theta = - \cos \theta_s \sin \xi \qquad 4.36$$

For the case when the axis of the cylinder is perpendicular to the flow ($\theta_s = 0$), $\sin \theta$ becomes

$$\sin \theta = - \sin \xi$$

For ξ between π and $3\pi/2$,

$$\cos \theta = - \cos \xi$$

Therefore, C_j and S_j become, for ξ between π and $3\pi/2$,

$$C_j = -\sigma_j \sqrt{1-\alpha_j} \frac{\cos \left[\frac{\pi}{2} P_j + (1-P_j)(-\pi + \xi)\right]}{\cos \xi} \qquad 4.37$$

$$S_j = -\sigma_j \sqrt{1-\alpha_j} \frac{\sin \left[\frac{\pi}{2} P_j + (1-P_j)(-\pi + \xi)\right]}{\sin \xi} \qquad 4.38$$

The coefficient of drag for this special case of the cylinder is found by taking twice the value obtained by integrating over ξ from π to $3\pi/2$. Letting $\bar{A} = 2 r_{cy} L$, the drag coefficient of a cylinder is given by

$$C_D = 2 + 2\sigma_j \sqrt{1-\alpha_j} \left[\frac{\cos \frac{\pi}{2} P_j}{(1-P_j)(3-P_j)}\right] \qquad P_j \neq 1, 3 \qquad 4.39$$

for $P_j = 1$, the expression in the bracket should be $\frac{\pi}{4}$. A value of $P_j = 3$ can not be meaningfully applied to the cylinder problem unless a discontinuous linear relationship is chosen for the angle-of-reflection law. Equation 4.39 is valid only for values of P_j between 0 and 2. Equation 4.39 can be shown to reduce to Equation 4.14 for the Maxwell model by substituting the appropriate values for σ_j, α_j, and P_j. The other coefficients are all zero for this special case of a non-spinning cylinder at $\theta_s = 0$.

4.2.1.3. Drag of Cone with Axis Parallel to Flow

For a non-spinning cone, $K_c = 0$, the expression for sin θ reduces to

$$\sin \theta = \sin \theta_s \sin \delta - \cos \theta_s \sin \xi \cos \delta$$

If $\theta_s = \frac{\pi}{2}$, the axis of the cone is parallel to the flow and the above equation for sin θ reduces to

$$\sin \theta = \sin \theta_s \sin \delta = \sin \delta$$

or

$$\theta = \delta$$

Therefore, θ is found to be independent of the variables of integration ℓ' and ξ. For $\theta_s = \frac{\pi}{2}$ the angle β is equal to a constant of $\frac{\pi}{2}$. Since the term χ in Equation 3.50 is also independent of ℓ' and ξ, Equations 3.50 can be integrated in closed form over ℓ' from 0 to 1 and ξ from 0 to 2π. Letting $A = \pi r_c^2$ the following equation for the coefficient of drag of the cone is obtained,

$$C_D = 2 - 2 \sigma_j \sqrt{1-\alpha_j} \cos \left[\frac{\pi}{2} P_j + (2-P_j) \delta \right] \qquad 4.40$$

The cone equation is found to have a form similar to that obtained for the flat plate at angle of attack.

4.2.1.4. Sphere Drag

The drag coefficient of a non-spinning sphere can be obtained from Equation 3.6.1 by letting $K_s = 0$ and $\theta_s = \frac{\pi}{2}$. Then, sin θ becomes

$$\sin \theta = \ell'$$

the next step is to now change variables of integration so that

$$\sin \nu = \ell'$$

$$\text{or } \nu = \theta$$

Substituting this into the expressions for C_j and S_j and then integrating Equation 3.61 over ξ from 0 to 2π and ν from 0 to $\frac{\pi}{2}$ and letting $\bar{A} = \pi r_s^2$, the following result is obtained

$$C_D = 2 + \sigma_j\sqrt{1-\alpha_j}\left[\frac{4(1-\cos\frac{\pi}{2}P_j)}{P_j(4-P_j)}\right];\ P_j \neq 0,\ 4 \qquad 4.41$$

where for $P_j = 0$ the bracketed term should be zero. As in the results obtained for the cylinder, Equation 4.41 for the sphere drag is valid only for values of P_j between 0 and 2. A value of P_j of 4 could only occur if a discontinuous linear relationship were chosen for the angle-of-reflection law and in that case the equation obtained would not be the same as Equation 4.41.

4.2.2. Numerical Methods

For cases other than those given in previous sections, the expressions derived in chapter 3 for aerodynamic properties contain integrals which must be evaluated numerically. In choosing a numerical technique, practical consideration must be given to the computation time required to

obtain results of suitable accuracy which in turn is dependent upon the computer being used to perform the computations. The numerical evaluation of the expressions of chapter 3 were made on a Control Data 1604 computer with an on-line video display system from which graphical results were obtained. The numerical techniques employed are described in the following.

4.2.2.1. Single Variable of Integration

Results requiring integration over one variable, such as those of the cylinder, were obtained by using the Gaussian integration formula over and arbitrary interval which is given by

$$\int_a^b f(y)\ dy = \frac{b-a}{2} \sum_{i=1}^{n} \omega_i\ f(y_i)$$

where

$$y_i = \left(\frac{b-a}{2}\right) x_i + \frac{b+a}{2}$$

The weights, ω_i, and abscissans, x_i, were obtained from Reference 22. The twenty point formula, n = 20, was used in all cases. From tests, it was found that at least five place accuracy was obtained by using this formula.

4.2.2.2. Double Integration

Results for the disk and cone require integration over two variables. For these cases, the region of integration was divided into squares of equal dimensions, h. (This is possible for the disk and cone since the region of integration is always rectangular.) For each square, a nine point double integration formula was used given by

$$\frac{1}{4h^2} \int_S \int f(x,y)\ dxdy = \sum_{i=1}^{9} \omega_i\ f(x_i,y_i) + R$$

From Reference 22, the abscissas (x_i, y_i) and weights ω_i are given as

(x_i, y_i)	ω_i
$(0,0)$	$16/81$
$(\pm\sqrt{\frac{3}{5}}\,h, \pm\sqrt{\frac{3}{5}}\,h)$	$25/324$
$(0, \pm\sqrt{\frac{3}{5}}\,h)$	$10/81$
$(\pm\sqrt{\frac{3}{5}}\,h, 0)$	$10/81$

where $R = O(h^6)$.

Tests showed that results of at least 5 place accuracy could be obtained in using this formula by dividing the region of integration into about 100 squares.

The above double integration formula was not applied to the sphere because the region of integration defined by the shadow boundary in the sphere is curved and cannot in general be divided accurately into squares. Numerical results for the sphere were not obtained in this study.

4.2.2.3. Graphical Display of Results

In order to evaluate the expressions given in Chapter 3 at various values of the quanities P_j, θ_s, K and, for the cone, δ, a numerical integration must be performed for each case separately. Graphical results of the variation in an aerodynamic property as a function of these quantities were obtained by evaluating the equations at six or more separate values of the quantity of interest and then using a six point Lagrange interpolation formula to plot the curve. For the case of the cylinder, for example, 288

separate numerical integrations were evaluated and stored on magnetic tape corresponding to six values for each of the quantities P_j and θ_s and eight values of K_{cy}. Graphs of any of the aerodynamic properties as a function of any of the three quantities can be generated by obtaining the appropriate values from storage and using the interpolation formula to obtain values along the curve. Graphs are displayed on a T.V. screen from which pictures may be obtained. Numerical results are also obtained.

4.3. Discussion of Results

The analytical solutions obtained in this chapter illustrate that the gas-surface interaction strongly influences the aerodynamic properties of both non-spinning and spinning bodies. For non-spinning bodies, the drag coefficient is the principal aerodynamic property of interest. Figures 4.1 through 4.8 are plots of some of the analytical results obtained on drag coefficient as a function of the gas surface interaction.

Figures 4.1 and 4.2 are plots of C_D given in Equations 4.8 and 4.33 for the flat plate versus angle of attack for various values of the parameter α_d of the Maxwell model and of P_j of the generalized model respectfully. The parameters α_T and α_j were set equal to .5 and $\sigma_j = 1$, and the spin rate parameter K_d is zero. These two plots illustrate the effect of the gas-surface interaction on determining aerodynamic properties. The effect of backscatter reflections is illustrated in Figure 4.2 by the curves for values of P_j between 1 and 2 and is seen to increase the drag coefficient values at all angles of attack.

Figures 4.3 and 4.4 are plots of C_D given in Equations 4.14 and

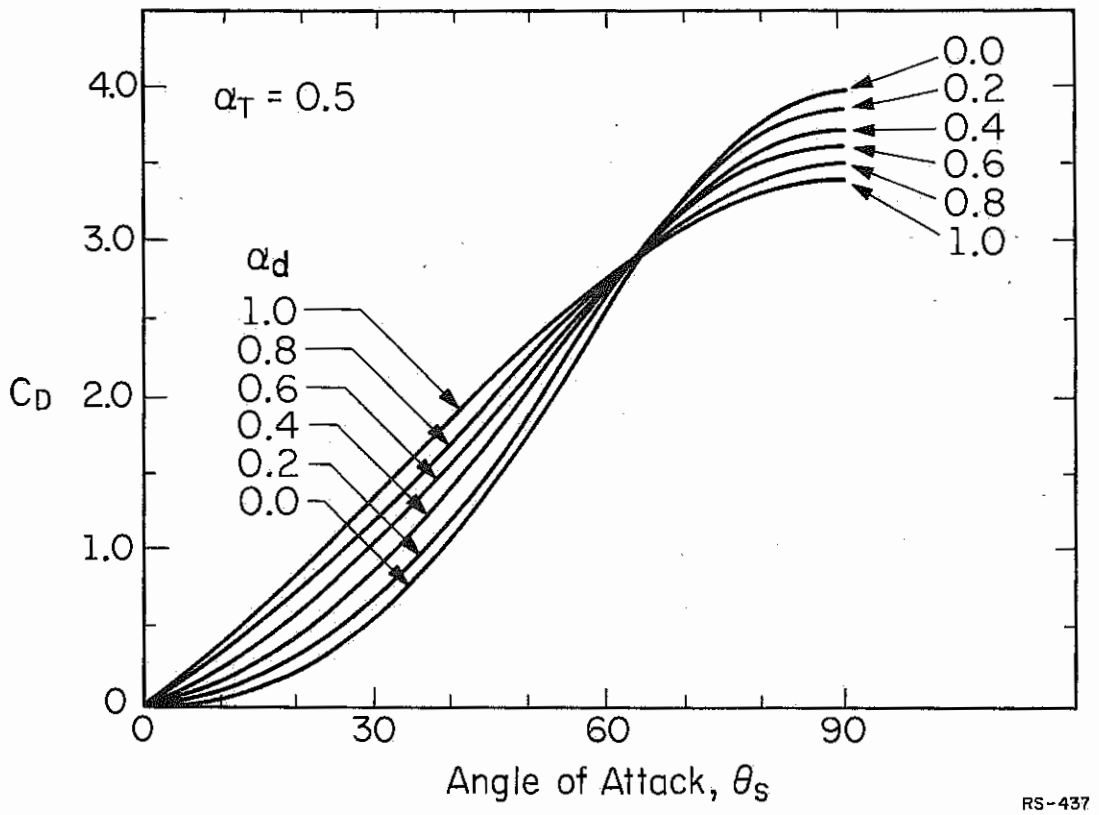

Figure 4.1. Drag coefficient of a non-spinning disk at angles of attack varying the Maxwell model parameter α_d.

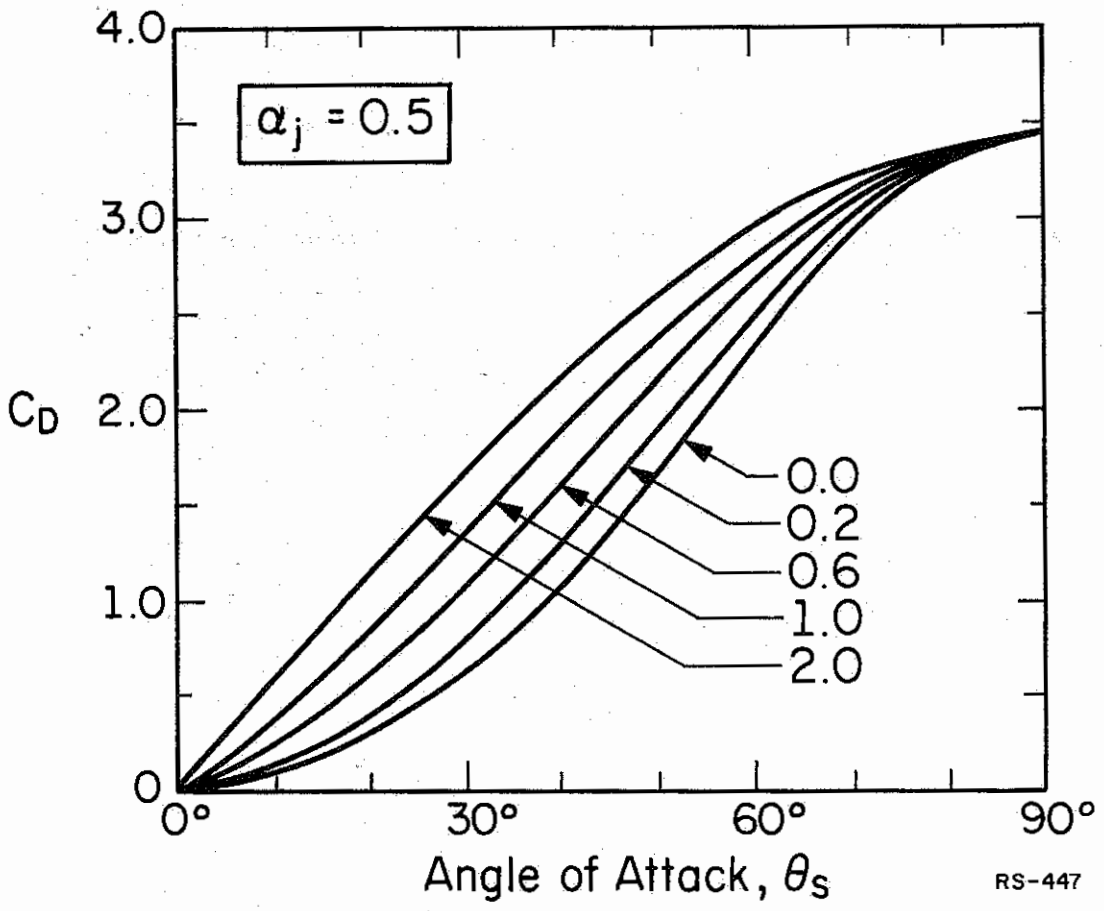

Figure 4.2. Drag coefficient of a non-spinning disk at angles of attack varying the generalized model parameter P_j.

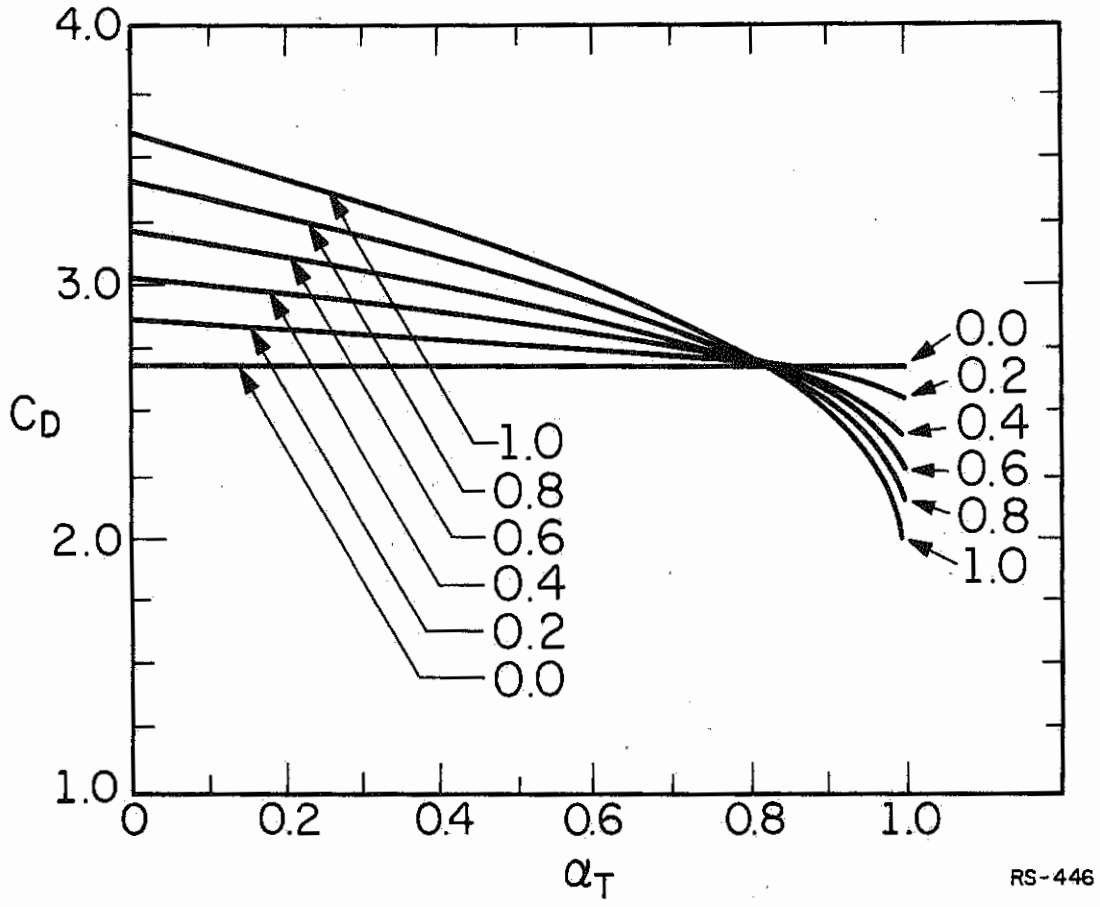

Figure 4.3. Drag coefficient of a non-spinning cylinder, with axis of cylinder perpendicular to the flow, as a function of the Maxwell model parameters.

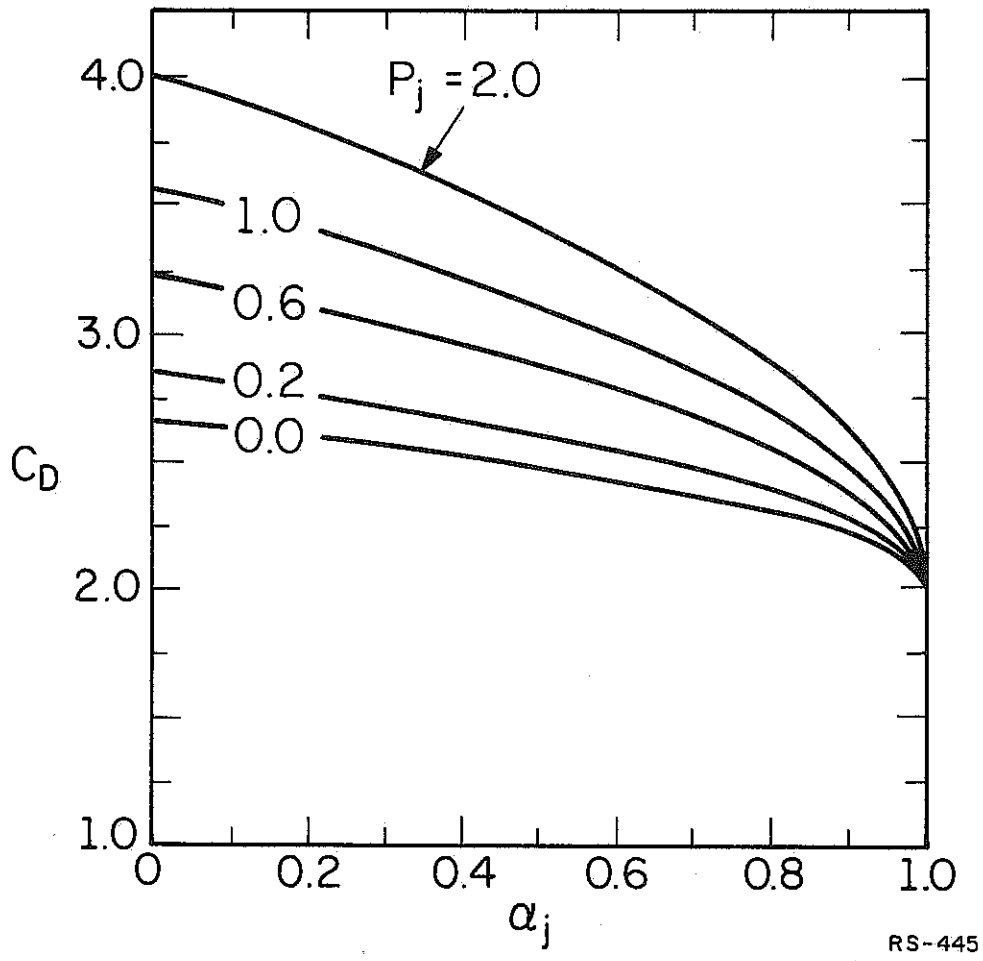

Figure 4.4. Drag coefficient of a non-spinning cylinder, with axis of cylinder perpendicular to the flow, as a function of the generalized model parameters.

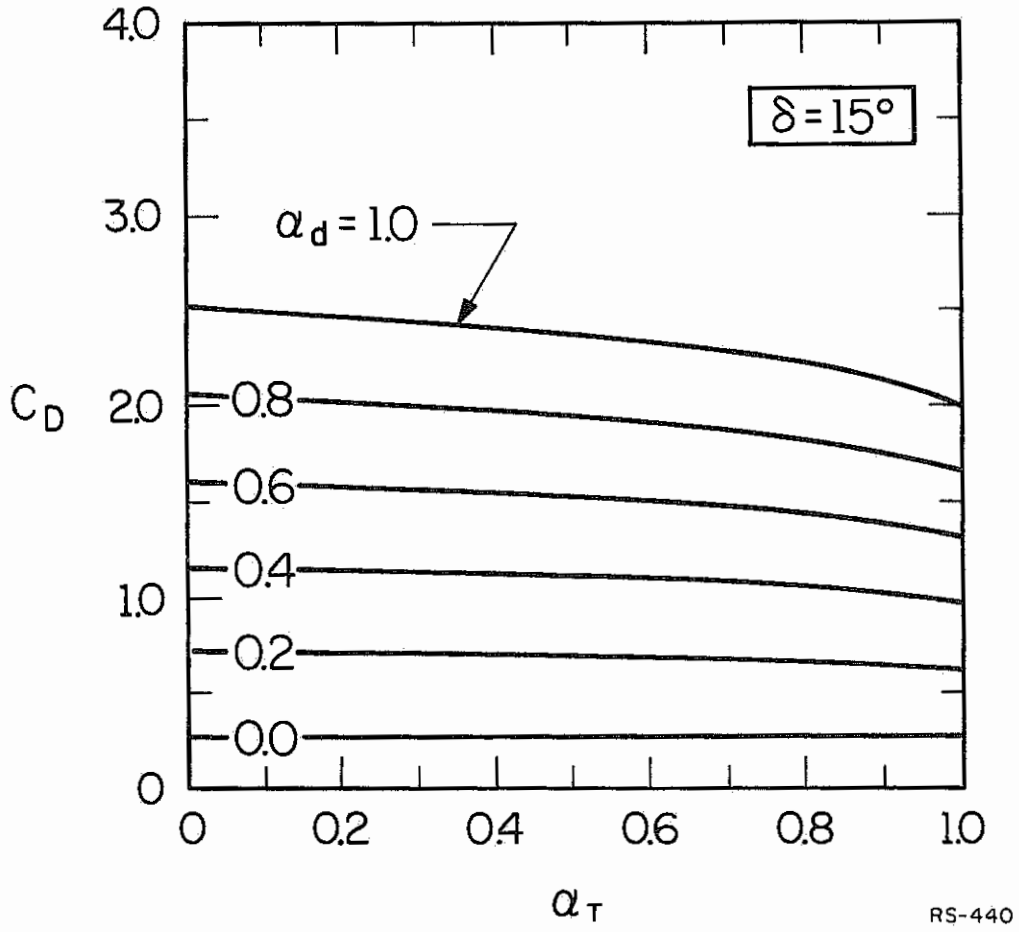

Figure 4.5. Drag coefficient of a non-spinning cone, with axis of the cone parallel to the flow, as a function of the Maxwell model parameters.

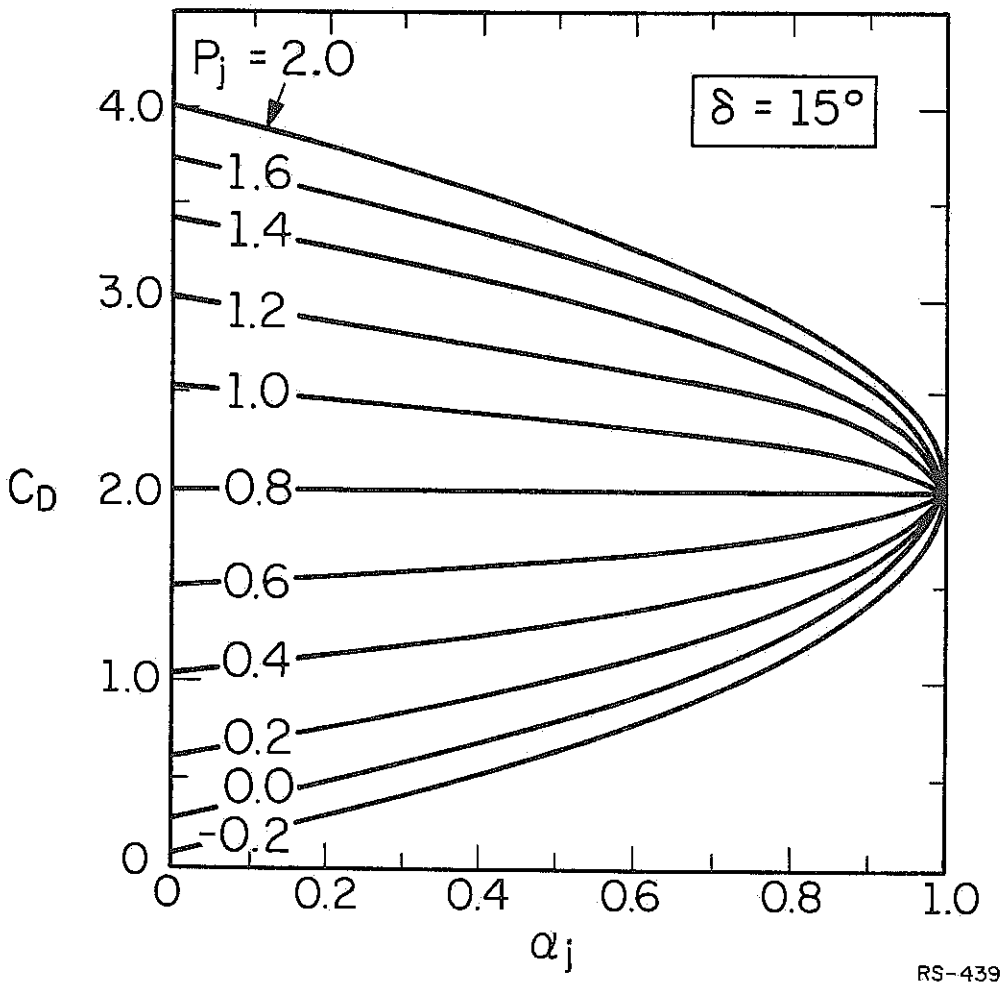

Figure 4.6. Drag coefficient of a non-spinning cone, with axis parallel to the flow, as a function of the generalized model parameters.

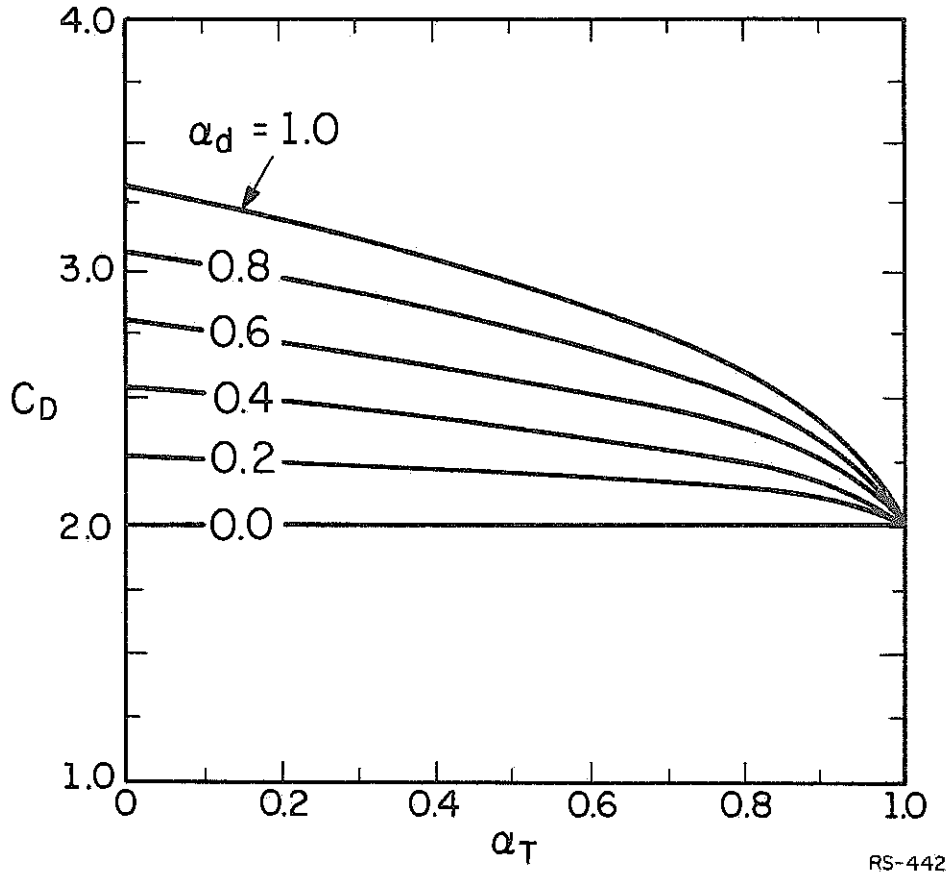

Figure 4.7. Drag coefficient of a non-spinning sphere as a function of the Maxwell model parameters.

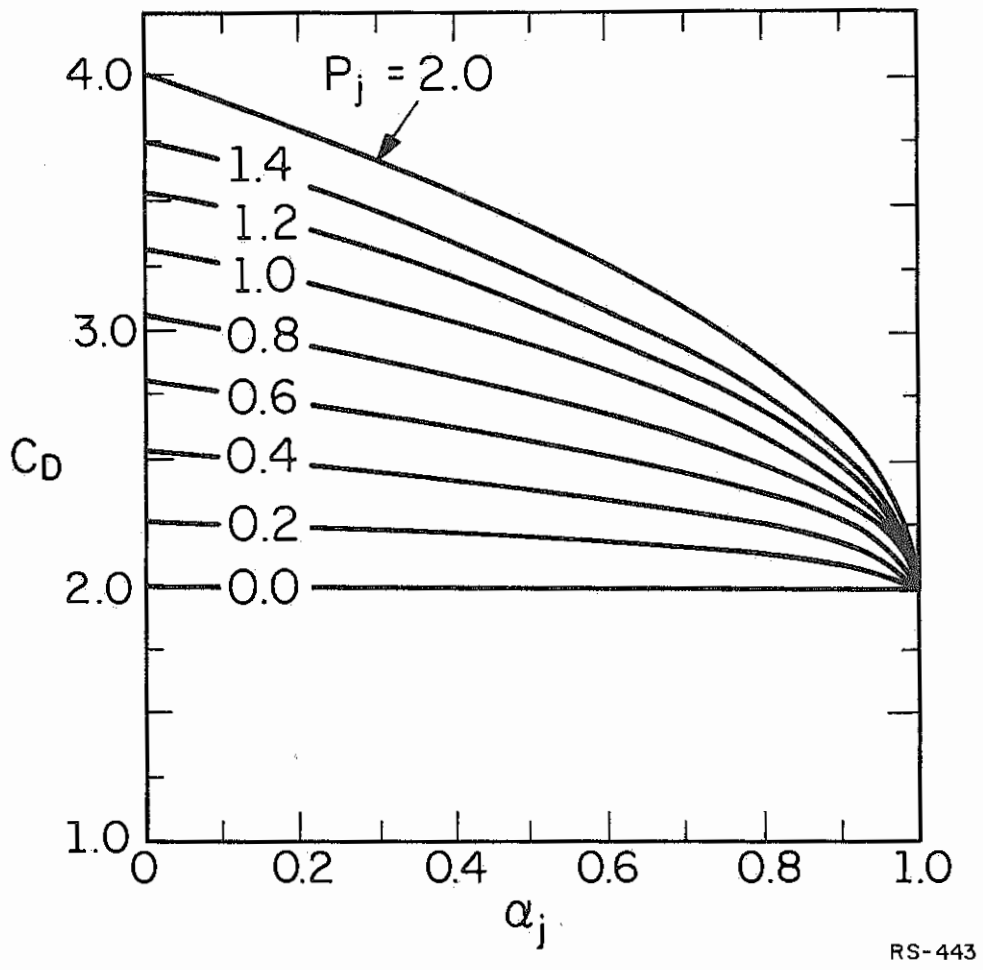

Figure 4.8. Drag coefficient of a non-spinning sphere as a function of the generalized model parameters.

4.39 for the non-spinning cylinder ($K_{cy} = 0$) with the axis of the cylinder perpendicular to the flow. Figure 4.3 gives the drag coefficient, using the Maxwell model, plotted versus α_T for various values of α_d. Figure 4.4 is a plot of C_D versus α_j for various values of P_j which are the parameters of the generalized model. For values of P_j between zero and one, the range in drag coefficient is the same for both models. For values of P_j greater than one, however, the generalized model gives higher values of C_D than does the Maxwell model.

Figures 4.5 and 4.6 are plots of C_D given in Equations 4.20 and 4.40 for the non-spinning cone ($K_c = 0$) with the axis of the cone parallel to the flow. The half angle of the cone for these plots if 15^o. Figure 4.5 gives the drag coefficient versus α_T for various values of α_d which are the parameters of the Maxwell model. Figure 4.6 is a plot, also of the drag coefficient, versus α_j for various values of P_j which are the parameters of the generalized model. In Figure 4.6, the effect of backscatter and over-specular reflections are both illustrated. The curve for $P_j = -.2$ shows that over-specular reflections give values of C_D less than 2. In general, over-specular reflections decrease the drag coefficient while backscatter increases the drag coefficient.

Figures 4.7 and 4.8 are plots of C_D given in Equations 4.30 and 4.41 for the non-spinning sphere. Unlike the previous plots, the two plots of sphere drag coefficients are very similar for the two cases of gas-surface interaction models. Figure 4.8 illustrates again that backscatter causes increased values of drag coefficient. The results shown in Figure 4.7 using the Maxwell model are different than results given by Cook[23] which are

similar to those given in Figure 4.7 except that the magnitudes of drag coefficients are different in the two plots for the same values of α_d and α_T. For example, at $\alpha_d = 1$ and $\alpha_T = 0$, Reference 23 gives a value of C_D for the sphere of about 2.89. Figure 4.7 (Equation 4.30) gives, however, a value of 10/3 for C_D of the sphere at $\alpha_d = 1$ and $\alpha_T = 0$. The difference between the two results is because the results in Reference 23 were obtained from Reference 15 in which Schamberg obtained the equation of C_D for the Maxwell model for a certain choice of parameters in his model. In reducing the Schamberg model to the Maxwell case, the distribution of velocities proposed by Schamberg were still retained which, as discussed in chapter 2, introduces a factor of 2/3 in the coefficient of $\sqrt{1-\alpha_T}$.

The effects of spin on the aerodynamic properties is well illustrated, for the Maxwell model, by the analytical results given in section 4.1 of this chapter. In general, the results show, for the case of the Maxwell model

1. As the spin rate increases, drag and $(\text{lift})_z$ increases. The increase is proportional to K^2.
2. A spin induced lift force in the lateral direction, $(\text{lift})_x$, occurs for elongated bodies at angles of attack. The lateral force is directly proportional to the spin rate parameter, K.
3. Spin induced torques perpendicular to the spin axis are experienced by all the shapes at angles of attack, except the cylinder.

4. The slowdown torque on a spinning body is directly proportional to K. Also, for the four shapes studied, the slowdown torque is directly proportional to α_d and independent of α_T.

The effects of spin described above were also found, in general, for the case of the generalized model. The results for the case of the generalized model were obtained by numerically evaluating the expressions given in chapter 3.

The numerical results showed that drag and $(\text{lift})_z$ increased with increased values of K and the increase was roughly proportional to K^2. The numerical results also showed that a spin-induced lateral force was experienced by the spinning cylinder and cone which is roughly proportional to K. As for the case of the Maxwell model, no lateral force was found to occur for the spinning disk. The numerical results for torque perpendicular to the spin axis also showed the same dependence on spin as indicated by the analytical results obtained in terms of the Maxwell model parameters.

Numerical results obtained for slowdown torque on a cylinder in terms of generalized model parameters are given in Figure 4.9. These results show that the slowdown torque is a function of both α_j and P_j. For the case of the Maxwell model the slowdown torque is dependent on only one of the model parameters, α_d. The numerical results for the slowdown torque of a spinning disk were similar to those obtained for the cylinder.

4.4. Conclusions

Two conclusions are evident from the results obtained in this

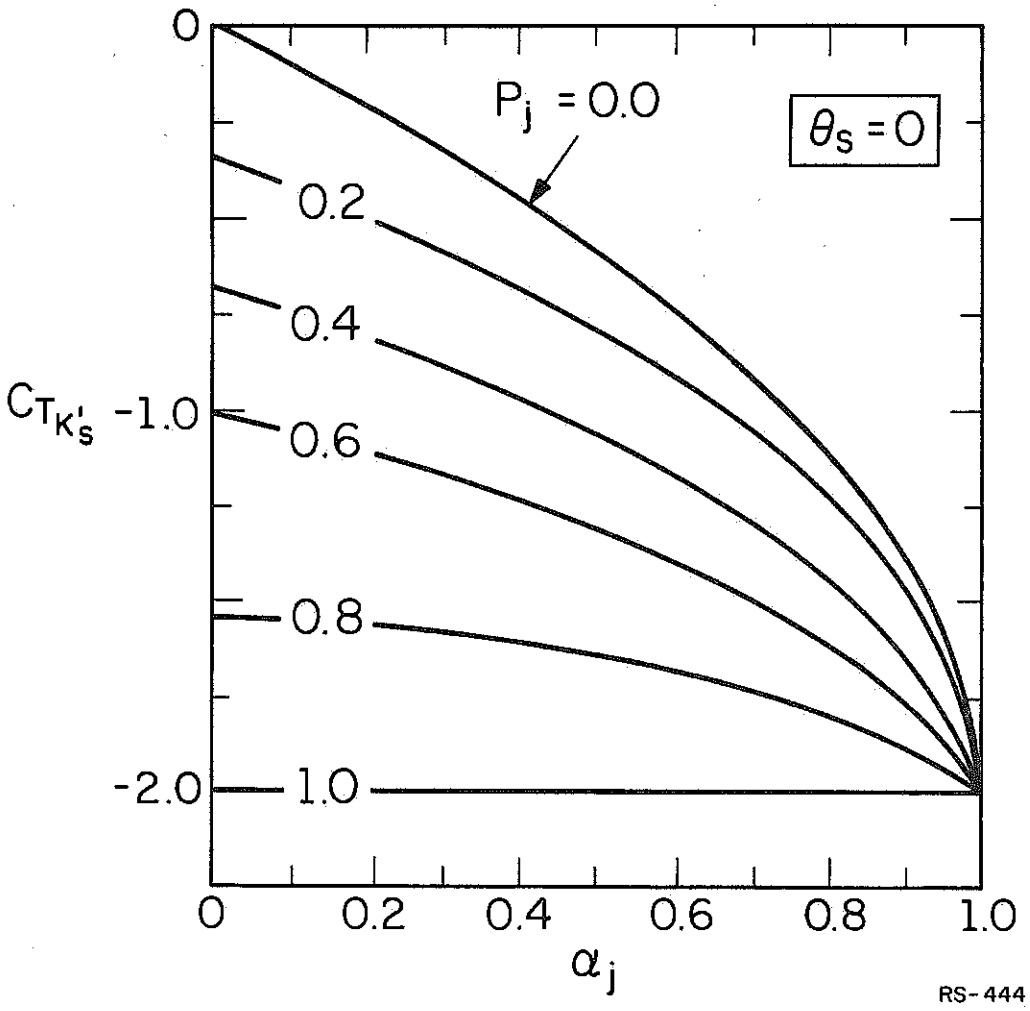

Figure 4.9. Coefficient of slow down torque on a spinning cylinder at zero angle of attack as a function of the generalized model parameters.

chapter. First, the aerodynamic properties of both non-spinning and spinning bodies is strongly affected by the gas surface interaction. Secondly, different shapes have functionally different dependence on the gas-surface interaction parameters of a particular model.

These two conclusions suggest that gas-surface interaction experiments could be performed in which measured aerodynamic properties of various shapes could be utilized to obtain information on the gas-surface interaction. Since the spin induced torque and $(\text{lift})_x$ properties are also strongly dependent upon the gas-surface interaction, considerable information on the gas-surface interaction could be obtained by making measurements of these aerodynamic properties of spinning bodies as a function of angle of attack.

The possible experiments suggested by the results of this chapter would be difficult, if not impossible, using current laboratory methods. It is, therefore, proposed that the aerodynamic properties of spinning satellites be utilized to obtain information on the gas-surface interaction. The high velocity, largely neutral, free molecular gas flow generated by a satellite's motion through the atmosphere are almost ideal experimental conditions for performing gas-surface interaction experiments. The remainder of this study is directed toward determining the feasibility of performing the satellite experiment suggested by the results of this chapter. Toward this end, the aerodynamic properties of spinning satellites are obtained in the next chapter.

5. AERODYNAMIC PROPERTIES OF SATELLITES

In chapter 4 the aerodynamic properties of bodies in a free molecular flow were determined for the case when the flow is stationary with respect to the body. In this chapter the aerodynamic properties of satellites is investigated for when the gas flow is no longer fixed in direction.

The instantaneous aerodynamic properties of a satellite can be found at any part in its orbit by a suitable coordinate transformation of the equations obtained in the preceding chapter. Since measurements of satellite aerodynamic properties are not usually made on an instantaneous basis, the average aerodynamic properties of a satellite over one orbit is investigated to determine how these average properties depend upon the gas-surface interaction.

The results of this chapter will be used in chapter 6 to study the feasibility of performing a satellite experiment to measure gas-surface interaction parameters. The equations and procedures developed in this chapter can also be applied to the problem of a tumbling non-spinning satellite. This application is illustrated by obtaining the average drag coefficient for a tumbling non-spinning disk as a function of the parameters of the Maxwell gas-surface interaction model.

5.1. Coordinate Transformation

In the equations developed in the preceding chapters, the aerodynamic properties of the various shapes were referred to a coordinate

system which was assumed fixed in inertial space and attached to the free stream velocity, $\vec{U}_\infty$. For a satellite in orbit about the earth, the coordinate system attached to $\vec{U}_\infty$ rotates in inertial space as the satellite travels in its orbit. Since the torques acting on the satellite must be referred to a non-rotating coordinate system, a new reference frame which is attached to the orbital plane of the satellite is chosen. For the purposes of illustrating the aerodynamic properties of satellites and the feasibility of the proposed satellite experiment, the orbit is assumed to be circular and have fixed orientation in inertial space*. The atmospheric density is also assumed to be constant over the orbit.

The initial orientation of the satellite spin vector in the orbital reference frame (x_o, y_o, z_o), is shown in Figure 5.1. The x_o-y_o plane is in the orbital plane of the satellite and z_o is the normal to the orbital plane. The free stream velocity vector, $\vec{U}_\infty$, rotates in the x_o-y_o plane at a constant rate, $\dot{\alpha}$, equal to the angular velocity of the satellite's orbit. For convenience, the satellite spin vector, $\vec{\Omega}$, is chosen to be initially in the x_o-z_o plane at an angle λ from the normal to the orbit, z_o.

With the above definitions, spherical trigometry can be used to find the angle θ_s in terms of the two angles λ and α. This expression is given by

$$\theta_s = \sin^{-1} (\cos \alpha \sin \lambda) \qquad 5.1$$

where θ_s is the angle between z and $\vec{\Omega}$. (The notation and definition of θ_s

*In general, the orbital plane is not an inertial frame of reference since the non-spherical distribution of the earth's mass can cause the orbital plane of a satellite to rotate in inertial space. This effect and other perturbing effects of the space environment are not included in this study.

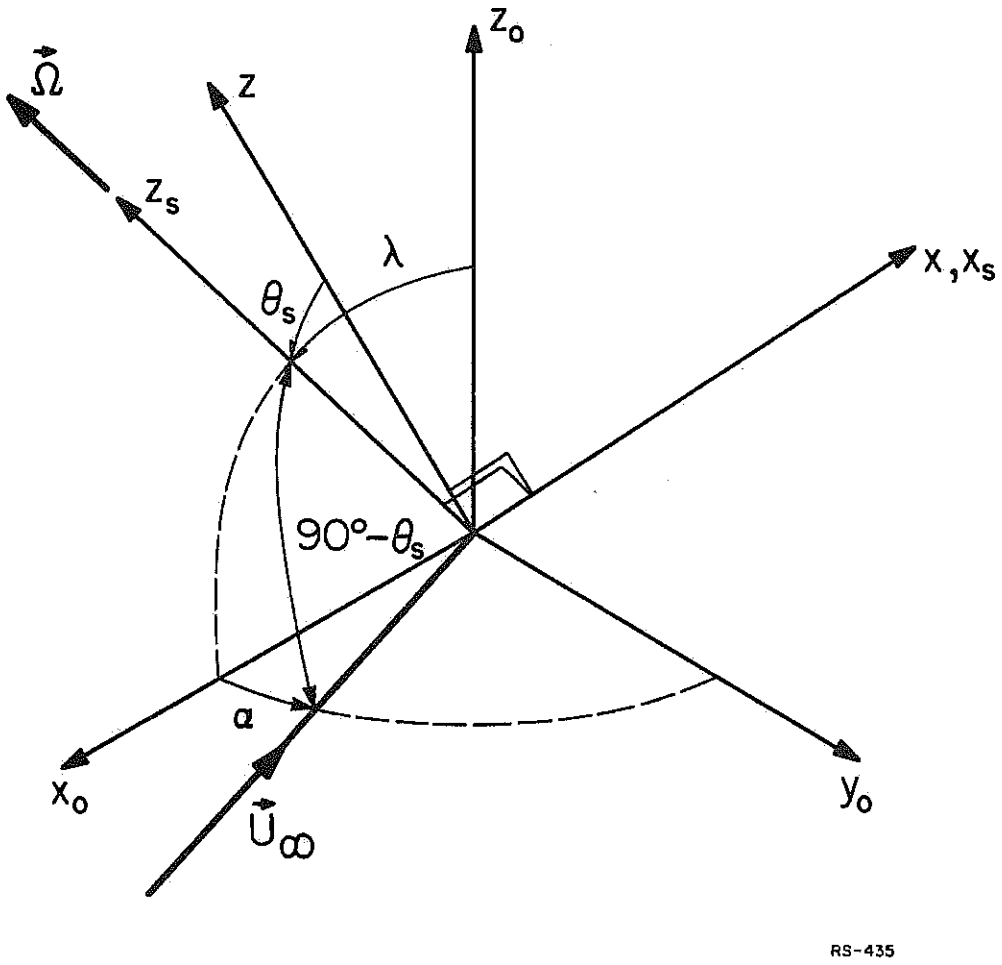

Figure 5.1. Notation and coordinate systems.

used in Equation 5.1 is consistent with that used in the equations of preceding chapters.)

5.2. Instantaneous Aerodynamic Properties of Satellite

By substituting the expression for θ, given by Equation 5.1, into the equations of the preceding chapters, the aerodynamic properties of a satellite can be determined at any position, α, in the orbit. For later applications, it is desirable to divide the instantaneous force and torque on the satellite into components associated with the x_o, y_o, z_o coordinate system.

5.2.1. Components of Force

The force acting on the satellite at any position α in the orbit is divided into a drag component in the direction of $\vec{U}_\infty$ and two components of lift, normal to $\vec{U}_\infty$. For force, a coordinate system x_s, y_s, z_s is defined which is associated with the x_o, y_o, z_o system as shown in Figure 5.2. The y_f-axis is in the direction of positive $\vec{U}_\infty$ and is therefore in the x_o-y_o plane. The z-axis is in the same direction as the z_o-axis and the x-axis then completes the triad. The force on the satellite is then divided into components of (drag) in the direction y_f; $(\text{lift})x_f$, which is in the plane of the orbit; and $(\text{lift})x_f$, which is normal to the orbital plane.

The components of force defined in the preceding chapters $(\text{drag})_y$, $(\text{lift})_x$, and $(\text{lift})_z$ are referred to the x_f, y_f, z_f system by performing the proper coordinate transformations and using Equation 5.1. The results are

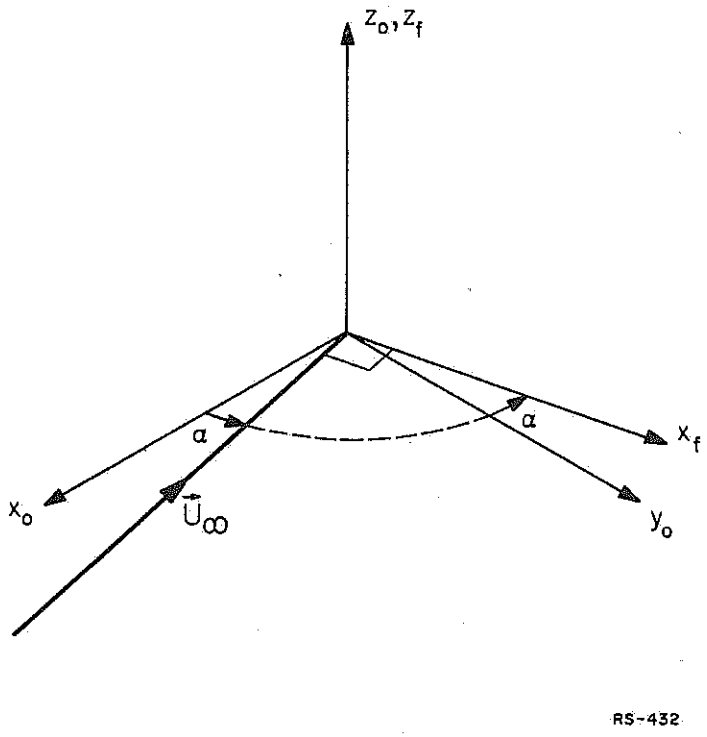

Figure 5.2. Coordinate system for force components.

$$F = \left[(\text{lift})_x \frac{\cos \lambda}{\cos \theta_s} - (\text{lift})_z \frac{\sin \alpha \sin \lambda}{\cos \theta_s}\right] i_f + \left[\text{drag}\right] j_f$$

$$+ \left[(\text{lift})_x \frac{\sin \alpha \sin \lambda}{\cos \theta_s} + (\text{lift})_z \frac{\cos \lambda}{\cos \theta_s}\right] k_f \qquad 5.2$$

where i_f, j_f, k_f are unit vectors in the x_f, y_f, z_f system and where

$$\cos \theta_s = \left(1 - \cos^2 \alpha \sin^2 \lambda\right)^{\frac{1}{2}}$$

Aerodynamic drag and lift forces are known to affect the elements of a satellite orbit. In terms of the components of force given in Equation 5.2, the principal effect of drag and $(\text{lift})_{x_f}$ (component of force in the i_f direction and in the plane of the orbit) is to cause the semi-major axis of the orbit to decay and cause the eccentricity of the orbit to decrease to zero (see for example References 24, 25, and 26). The third component of force, $(\text{lift})_{z_f}$ is normal to orbital plane in the direction k_f. This force causes a torque on the orbit and has the effect of causing the orbital plane to precess in inertial space which is analogous to a gyroscope precessing under the action of an external torque.

A complete study of the perturbating effects of drag and lift must necessarily include also other perturbating forces of the space environment such as solar radiation pressure and gravity gradient forces. Such a study is beyond the scope of the present work. For the purpose of the present study, consider the torque on a circular orbit caused by the $(\text{lift})_{z_f}$ component of force. The radius vector, r_o, from the center of the earth to the satellite is given by

$$\vec{r}_o = r_o \sin \alpha \, i_o - r_o \cos \alpha \, j_o \qquad 5.3$$

The torque on the orbit is then given by

$$\vec{T}_o = \vec{r}_o \times (\text{lift})_{z_f} k_f \qquad 5.4$$

Since $k_f = k_o$

$$\vec{T}_o = -r_o \cos\alpha\, (\text{lift})_{z_f} i_o - r_o \sin\alpha\, (\text{lift})_{z_f} j_o \qquad 5.5$$

Define the coefficient of torque on-the-orbit to be given by

$$C_{T_o} = T_o / \tfrac{1}{2} \rho U_\infty^2 \bar{A} r_o \qquad 5.6$$

where $\bar{A}$ is the reference area of the satellite.

Using Equations 5.5, 5.6, and the k_f component of forces given in Equation 5.2, the coefficients of torque on-the-orbit about the x_o and y_o axis, respectively, become

$$(C_{T_o})_{x_o} = \frac{-\cos\alpha \sin\alpha \sin\lambda}{\cos\theta_s} C_{L_x} - \frac{\cos\alpha \cos\lambda}{\cos\theta_s} C_{L_z} \qquad 5.7$$

$$(C_{T_o})_{y_o} = \frac{-\sin^2\alpha \sin\lambda}{\cos\theta_s} C_{L_x} - \frac{\sin\alpha \cos\lambda}{\cos\theta_s} C_{L_z}$$

5.2.2. Components of Torque Acting on Satellites

The torque acting on the satellite at any position α in its orbit is divided into a slowdown component in the direction of $\vec{\Omega}$, and two components of torque perpendicular to $\vec{\Omega}$. For satellite torque, a coordinate system x_o', y_o', k_o' is defined which is associated with the x_o, y_o, z_o system as shown in Figure 5.3. The z_s'-axis is in the direction of $\vec{\Omega}$ and is therefore in the x_o-y_o plane. The x_s'-axis is in the same direction as the y_o-axis. The y_s'-axis then completes the triad. The components of torque on the satellite are then denoted by a slowdown component, $T_{k_s'}$, in the direction $\vec{\Omega}$; a $T_{x_s'}$ component of torque in the plane of the orbit and in the direction

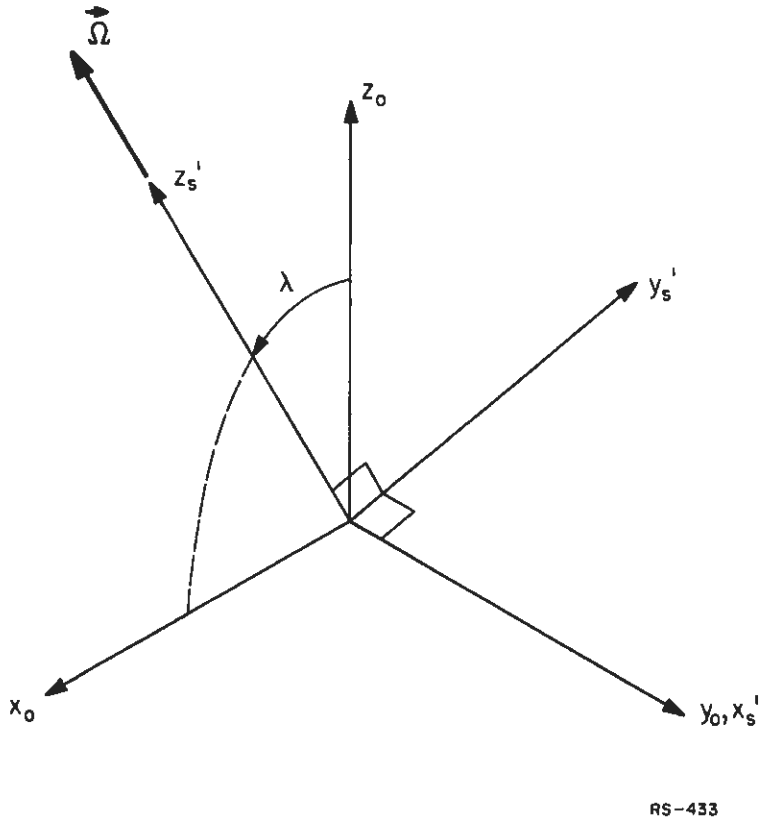

Figure 5.3. Coordinate system for torque components.

x_s; and a T_{j_s}, component which is out-of-the-plane of the orbit by the angle λ. The components of torque perpendicular to $\vec{\Omega}$ cause precession which also has components out-of-the plane and in-the-plane of the orbit.

The components of torque defined in the preceding chapters (T_{i_s}, T_{j_s}, and T_{k_s}) are referred to the x_s', y_s', z_s' system by performing the proper coordinate transformation and using Equation 5.1. The results are

$$\vec{T} = \left[T_{i_s} \frac{\cos\alpha \cos\lambda}{\cos\theta_s} - T_{j_s} \frac{\sin\alpha}{\cos\theta_s}\right] i_s' + \left[T_{i_s} \frac{\sin\alpha}{\cos\theta_s} + T_{j_s} \frac{\cos\alpha \cos\lambda}{\cos\theta_s}\right] j_s' + \left[T_{k_s}\right] k_s' \qquad 5.9$$

This equation and the equation of the previous section allow the results of chapter 4 to be used to find the instantaneous aerodynamic properties of a satellite at any point α in its orbit.

5.3. Average Aerodynamic Properties of Satellites

The average aerodynamic properties of a body is defined by the equation

$$\bar{C} = \frac{1}{T'} \int_0^{T'} C \, dt \qquad 5.10$$

where C represents the aerodynamic property being averaged and T' is the time interval over which the average is taken. As a satellite travels through its orbit, the velocity vector $\vec{U}_\infty$ rotates in the x_o-y_o plane. The position of the velocity vector is determined by the angle α at a given time t. For the purposes of the present study, consider the case of

a satellite in near-earth circular orbit. If the altitude loss due to the action of aerodynamic drag is assumed to be small, the angular velocity of the satellite's orbit can be approximated by a constant determined by the average radius of the orbit for a single pass about the earth. Similarly, an average circular velocity equal to the free stream velocity U_∞ and an average atmospheric density ρ can be approximated by constants.

For a constant angular velocity $\dot{\alpha} = \omega$, Equation 5.4 can then be changed to an integral of the angle α over 2π for one complete orbit. The equation for the average aerodynamic properties of a satellite over one complete orbit is then given by

$$\bar{C} = \frac{1}{2\pi} \int_0^{2\pi} C \, d\alpha \qquad 5.11$$

Equations 5.2, 5.7, 5.8 and 5.9 can then be substituted into Equation 5.11, with the appropriate equations from the preceding chapter, to determine the average properties of satellites.

5.3.1. Spinning Disk

In general, the evaluation of Equation 5.11 involves the use of numerical techniques. For the case of the properties of the spinning disk in terms of the Maxwell model parameters, however, Equation 5.11 can be evaluated analytically. The procedure is to first substitute Equations 4.8 through 4.13 for the disk into the equations for the instantaneous aerodyanmic properties given by Equations 5.2, 5.7, 5.8 and 5.9. Equation 5.1 is used to replace θ_s in terms of α and λ. These results are then substituted into Equation 5.11 and integrated to find the average properties

over one orbit. Two cases are considered: 1) spinning disk with one side exposed to the flow and 2) spinning disk with both sides exposed to the flow. The results of the first case can be applied to problems such as a spinning cylinder or spinning cone in which the ends of the cylinder and base of the cone can be represented as spinning disks.

5.3.1.1. Spinning Disk with One Side Exposed to the Flow

Following the procedure outlined above, the results for the average properter of a spinning disk with one side exposed to flow are

$$\bar{C}_D = \frac{8}{3\pi} \sin^3 \lambda + \alpha_d \left(\frac{2}{\pi} \sin \lambda - \frac{8}{3\pi} \sin^3 \lambda\right) + \alpha_d \sqrt{1-\alpha_T} \left[\frac{1}{2} \sin^2 \lambda + K_d^2 \left(\frac{1}{16} \sin^2 \lambda + \frac{3}{64} \sin^4 \lambda\right)\right] \quad 5.12$$

$$\bar{C}_{T_{i_s'}} = 0 \quad 5.13$$

$$\bar{C}_{T_{j_s'}} = -\frac{1}{8} \alpha_d \sqrt{1-\alpha_T} K_d \sin \lambda \cos \lambda \quad 5.14$$

$$\bar{C}_{T_{k_s'}} = -2 \alpha_d K_d \sin \lambda \quad 5.15$$

$$(\overline{C_{T_o}})_{x_o} = -\frac{8}{3\pi} (1-\alpha_d) \sin^2 \lambda \cos \lambda - \alpha_d \sqrt{1-\alpha_T} K_d^2 \left(\frac{1}{16} \sin \lambda \cos \lambda + \frac{3}{64} \sin^3 \lambda \cos \lambda\right) \quad 5.16$$

$$(\overline{C_{T_o}})_{y_o} = 0 \quad 5.17$$

5.3.1.2. Spinning Disk with Both Sides Exposed to the Flow

The procedure to be followed for the case of the disk with both sides exposed to the flow is the same as above except that, when the flow

is on the "back-side" of the disk, appropriate changes in signs must be made on Equations 4.8 through 4.13 to account for the fact that the spin rate vector $\vec{\Omega}$ is in the opposite direction. The results are

$$\bar{C}_D = \frac{16}{3\pi} \sin^3 \lambda + \alpha_d \left(\frac{4}{\pi} \sin \lambda - \frac{16}{3\pi} \sin^3 \lambda\right) + \alpha_d \sqrt{1-\alpha_T} \left[\sin^2 \lambda + K_d^2 \left(\frac{1}{8} \sin^2 \lambda + \frac{3}{32} \sin^4 \lambda\right)\right] \quad 5.18$$

$$\bar{C}_{T_{i_s'}} = 0 \quad 5.19$$

$$\bar{C}_{T_{j_s'}} = 0 \quad 5.20$$

$$\bar{C}_{T_{k_s'}} = -4 \alpha_d K_d \sin \lambda \quad 5.21$$

$$(\bar{C}_{T_o})_{x_o} = -\frac{16}{3\pi} (1-\alpha_d) \sin^2 \lambda \cos \lambda - \alpha_d \sqrt{1-\alpha_T} K_d^2 \left(\frac{1}{8} \sin \lambda \cos \lambda + \frac{3}{32} \sin^3 \lambda \cos \lambda\right) \quad 5.22$$

$$(\bar{C}_{T_o})_{y_o} = 0 \quad 5.23$$

For the case of both sides of the disk exposed, the torque perpendicular to the spin axis of the satellite is found to average to zero over one orbit. The average drag and torque on-the-orbit about the x_o axis is found to double as would be expected.

5.3.2. Spinning Spherical Satellite

The average coefficients of torque on a spinning spherical satellite can be obtained in terms of the parameters of the Maxwell model from Equations 4.27 through 4.29. The results are

$$\bar{C}_{T_{i_s'}} = 0 \qquad 5.24$$

$$\bar{C}_{T_{j_s'}} = \frac{1}{4} K_s \alpha_d \sin \lambda \cos \lambda \qquad 5.25$$

$$\bar{C}_{T_{k_s'}} = -\frac{1}{4} K_s \alpha_d (6 - \sin^2 \lambda) \qquad 5.26$$

Unlike for the case of the disk, the average, over one orbit, of torque perpendicular to the spin axis, $\bar{C}_{T_{j_s'}}$, is found to be finite for the case of a spherical satellite.

5.3.3. Spinning Cone-Disk Composite Satellite

Consider a satellite composed of a cone spinning about the axis of the cone and a flat base represented by a spinning disk. For convenience, consider the center of mass of the satellite to be at the center of the base of the cone. For purposes of illustration the gas-surface interaction will be assumed to be of the Maxwell type. The equations expressing the aerodynamics of the spinning cone at angles of attack have been obtained in analytical form in terms of the Maxwell model parameters and are given by Equations 4.20 through 4.26 in chapter 4. Since a cone-disk composite satellite is a convex body, Equations 5.12 through 5.17 for the disk with one side exposed to the flow can be applied directly. The sign of $\bar{C}_{T_{j_s'}}$ (Equation 5.14) is reversed for this application since only the "back-side" of the spinning disk is exposed to the flow.

The average properties of the cone part of the spinning cone-disk composite satellite are obtained using the numerical techniques described previously to perform the integration over α in Equation 5.11. For example,

for a cone of a half angle of 15^{o} and $\lambda = 45^{o}$ the following results were obtained numerically.

$$\bar{C}_D = \frac{1}{2\pi} \left[15.4 + .45\ \alpha_d + \alpha_d\sqrt{1-\alpha_T}\ \ (10.5 + 2.04\ K^2)\right] \qquad 5.27$$

$$\bar{C}_{T_{i_s'}} = \frac{1}{2\pi} \left[-3.12 + 3.12\ \alpha_d - \alpha_d\sqrt{1-\alpha_T}\ (1.3 + 8.7 \times 10^{-3}\ K^2)\right] \qquad 5.28$$

$$\bar{C}_{T_{j_s'}} = \frac{1}{2\pi} \left[-.402\ K\ \alpha_d - \alpha_d\sqrt{1-\alpha_T}\ (2.3 \times 10^{-2}\ K + 8.2\ K^2)\right] \qquad 5.29$$

$$\bar{C}_{T_{k_s'}} = -\frac{7.9}{2\pi}\ K\ \alpha_d \qquad 5.30$$

$$(\bar{C}_{T_o})_{x_o} = \frac{1}{2\pi} \left[-1.22 + 1.22\ \alpha_d - \alpha_d\sqrt{1-\alpha_T}\ (.85 - .38\ K^2)\right] \qquad 5.31$$

$$(\bar{C}_{T_o})_{y_o} = \frac{1}{2\pi} \left[2.76\ K\ \alpha_d - \alpha_d\sqrt{1-\alpha_T}\ (1.07\ K)\right] \qquad 5.32$$

The average properties of a cone-disk satellite are a function of the cone half angle δ and the angle λ. This functional dependence is illustrated in Figure 5.4 where the average drag coefficient is shown plotted as a function of the angle λ for various values of the angle δ.

5.4. Average Aerodynamic Properties of Tumbling Bodies

The average aerodynamic properties of a body which is tumbling in a random manner can be found using the techniques developed in this chapter. Let the orientation of the body with respect to the flow be determined by the angles α and λ. If the orientation is completely random, all values of λ between 0 and π and of α between 0 and 2π occur for an equal amount of

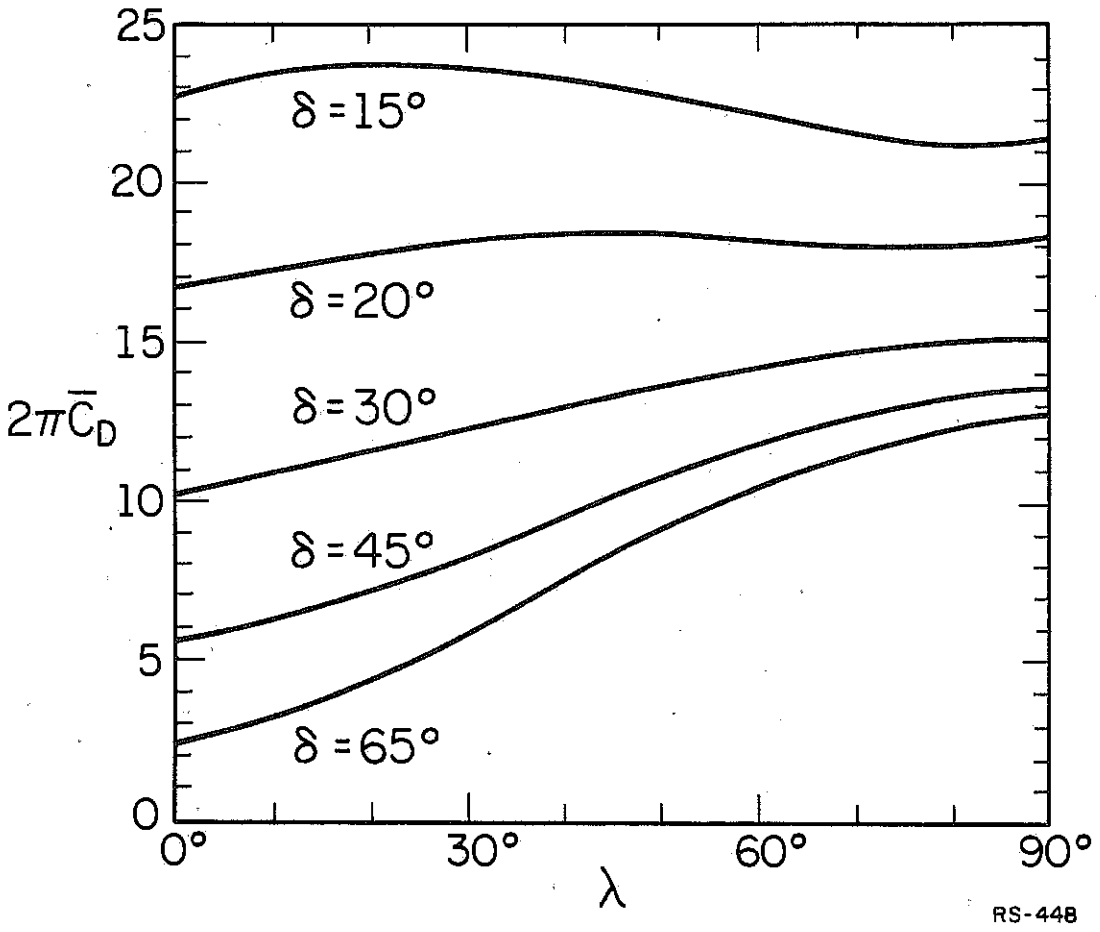

Figure 5.4. Average drag coefficient of a cone-disk shaped satellite as a function of λ and δ.

time. The average of an aerodynamic property for a random-tumbling body is expressed by

$$\bar{C} = \frac{1}{4\pi} \int_0^{2\pi} \int_0^{\pi} C \sin \lambda \, d\lambda \, d\alpha \qquad 5.33$$

where C is the aerodynamic property being averaged (see Reference 27).

A single example of the application of Equation 5.33 is given in the following for the case of a non-spinning disk.

5.4.1. Average Drag Coefficient of a Random-Tumbling Disk

The instantaneous drag coefficient of a disk in terms of the parameters of the Maxwell model is given by Equation 4.8. In terms of the angles α and λ, the instantaneous drag coefficient for zero spin rate is given by

$$(\bar{C}_D)_{disk} = 4 \cos^3 \alpha \sin^3 \lambda + \alpha_d (2 \cos \alpha \sin \lambda - 4 \cos^3 \alpha \sin^3 \lambda) + \alpha_d \sqrt{1-\alpha_T} \, 2 \cos^2 \alpha \sin^2 \lambda \qquad 5.34$$

Due to symmetry, the integration of Equation 5.33 for the disk can be obtained as eight times the integration over α from 0 to $\frac{\pi}{2}$ and λ from 0 to $\frac{\pi}{2}$. The result is

$$(\bar{C}_D)_{disk} = 1 + \frac{2}{3} \alpha_d \sqrt{1-\alpha_T} \qquad 5.35$$

The average drag coefficient of the random-tumbling disk is found to be considerably less than the maximum possible drag coefficient of four for a stationary disk normal to the flow. The average drag coefficient given in Equation 5.35 is exactly half the drag coefficient of a sphere (see Equation 4.30).

Approximation techniques have been commonly employed to determine

average drag coefficients of tumbling bodies. The results of two approximation techniques applied to the disk problem are given for comparison to the results given in Equation 5.35. Using results obtained by Schamberg (Reference 15)

$$(C_D) \approx 3 + 2\,\alpha_d\sqrt{1-\alpha_T} \qquad 5.36$$

Using techniques developed by Sentman and Neice (Reference 27)

$$(C_D) \approx .85 - .42\,\alpha_d + .42\,\alpha_d\sqrt{1-\alpha_T} \qquad 5.37$$

The approximation techniques used in Reference 15 (Equation 5.36) are seen to give a drag coefficient three times greater than that given by Equation 5.35. The approximation technique of Reference 27, on the other hand, gives slightly lower results than that given by Equation 5.35, but the percent error is considerably less than the results of Reference 15.

5.5. Discussion of Results

The results obtained in this chapter have been limited to the use of the Maxwell model because analytical expressions could be obtained in most of the cases studied. The procedures used to obtain these results are, however, equally applicable to problems using the generalized model if numerical methods are employed.

The results obtained have shown than the average aerodynamic properties of a satellite are of the same form as those obtained in chapter 4 for stationary flow conditions. The average aerodynamic properties are found also to be strongly dependent upon the parameters of the gas surface interaction model. In general, the average aerodynamic properties of

satellites can be expressed in the following form as a function of the parameters of the Maxwell model.

$$\begin{aligned}
\bar{C}_D &= A_1 + \alpha_d A_2 + \alpha_d\sqrt{1-\alpha_T}\ A_3 \\
\bar{C}_{T_{i_s}'} &= B_1 + \alpha_d B_2 + \alpha_d\sqrt{1-\alpha_T}\ B_3 \\
\bar{C}_{T_{j_s}'} &= C_1 + \alpha_d C_2 + \alpha_d\sqrt{1-\alpha_T}\ C_3 \\
\bar{C}_{T_{k_s}'} &= D\,\alpha_d
\end{aligned} \qquad 5.38$$

where the coefficients A, B, etc., are functions of the angle λ and the spin-rate parameter K, and also the half angle δ for the cone.

It is, therefore, evident that, as for bodies in a stationary flow, the possibility exists of utilizing measured, <u>average</u> satellite-aerodynamic properties to obtain <u>specific</u> information on the gas-surface interaction. The feasibility is assessed in the next chapter of performing a satellite experiment to determine gas-surface parameters by measuring the average aerodynamic properties of satellites.

6. FEASIBILITY OF A SATELLITE EXPERIMENT TO DETERMINE THE GAS-SURFACE INTERACTION PARAMETERS AND THE ATMOSPHERIC DENSITY

The results of the preceding chapter have indicated clearly the possibility of utilizing measured aerodynamic properties of satellites to obtain information on the gas-surface interaction. The feasibility of this experimental concept is discussed in this chapter.

The obvious advantage of designing a gas-surface interaction experiment using satellites is that a free molecular flow of high velocity neutral molecules is generated by the motion of the satellite in its orbit. As discussed earlier, it has not been possible to duplicate these flow conditions in the laboratory. As with all experiments, even those performed under supposedly controlled conditions, information obtained on the gas-surface interaction from the analysis of satellite aerodynamic properties would be subject to certain uncertainties associated with the experiment. For satellite experiments of the type proposed in this study, uncertainties associated with the space environment could influence the interpretation and accuracy of results. A complete discussion of the major uncertainties and their influence on the proposed experiment is given in the latter part of this chapter. However, since the uncertainty associated with the orbital gas-density is of major importance to the proposed experiment, this subject is discussed in the following.

The reason for the uncertainty in orbital gas-density can be traced to the lack of knowledge on the drag coefficient of satellites which, in turn, is related to the uncertainty in the gas-surface interaction. As an example, consider the measurement of the drag of a satellite

in which the drag is related to the density by the drag equation given by

$$\text{Drag} = \frac{1}{2} \rho U_\infty^2 \bar{A} C_D$$

In order to determine the atmospheric density ρ from the drag measurement, the drag coefficient, C_D, of the body must be known. Due to the lack of knowledge on the gas-surface interaction, an assumed value of the drag coefficient of 2.2 is commonly used to reduce drag data.[28] From the results of chapters 4 and 5, it is seen that this assumption could lead to considerable error, perhaps 50% or greater, in the determination of density depending upon the actual values of the gas-surface interaction parameters and the shape of the body.

It is apparent from the above discussion that a satellite experiment designed to obtain information on the gas-surface interaction must, also, simultaneously, obtain information on the atmospheric density. For this reason, then, the satellite experiments proposed in this study are designed to determine the value of the atmospheric density in addition to determining the values of gas-surface interaction parameters.

6.1. Gas-Surface Interaction Experiments Utilizing Satellite Aerodynamic Properties

Two criteria must be met in order to utilize measured aerodynamic properties of satellites to obtain information on the gas-surface interaction and atmospheric density. The first criteria is that the number of aerodynamic properties measured must at least equal the number of unknown quantities to be determined. The second criteria is that the equations

expressing the measured aerodynamic properties in terms of the unknowns must form an independent set of equations which can then be solved for the unknowns.

Two general classifications can be made of possible methods of utilizing satellite data which could satisfy the basic criteria given above. These classifications of possible methods are:

Method 1: Utilizing data (such as drag) from a number of differently shaped and/or differently oriented satellites.

Method 2: Utilizing data on a number of aerodynamic properties of a properly designed satellite.

The methods of analysis are similar in both classifications. In Method 1, data on past or existing satellites would be used while in Method 2 a satellite is to be designed for the specific purpose of obtaining information on the gas-surface interaction. It is not suggested, however, that either of the two methods be used exclusively. In fact, as will be pointed out later, a combination of the two methods appears desirable in terms of a long range program to obtain information on the gas–surface interaction as a function of the surface conditions and also to obtain information on the density and composition of the orbital gas environment.

The procedure, advantages, and disadvantages associated with the two methods are discussed in the following two sections. Later in this chapter the feasibility will be illustrated of using Method 2 to determine the parameters of the Maxwell model and the atmospheric density.

6.1.1. Method 1: Utilization of Data From Satellites of Different Shapes

In chapter 5 it was found that the average aerodynamic properties of satellites are dependent upon the parameters of the gas-surface interaction. In addition, the angle λ, which is the angle giving orientation of the satellite spin axis with respect to orbit, was also found to have an influence on the coefficients of the unknown parameters. These two factors are to be considered in utilizing data from satellites of different shapes and orientation in making the measurements.

To begin the discussion of Method 1, consider that, for example, drag data were available on a spinning disk, a spinning cone (with flat base) and a non-spinning sphere. Consider that each of these satellite shapes has the same surface properties, are all in the same circular orbit, and that the gas density is constant over the orbit. Under these considerations and the assumption that the gas-surface interaction is of the Maxwell type, the drag measurements of the three would provide sufficient information for the determination of the parameters α_d, α_T and ρ. The fact that the values of α_d, α_T and ρ can be determined can be verified from the equations given in chapter 5 for the spinning disk with both sides exposed (Equation 5.18) and the numerical results given for the cone-disk satellite (Equation 5.27). The average drag for a non-spinning sphere would be the same as that given in chapter 4 for stationary flow, (Equation 4.30). These three equations satisfy both criteria of the experiment, as can be easily verified. Using the same set of equations one could also verify that two spinning disks at different angles λ to the orbital plane could also provide a system of independent equations when combined with either the cone-disk

or sphere equations. One can also easily verify that measurements of drag on, for example, three different sized spheres would not lead to an independent set of equations which could be solved for α_d, α_T, and ρ.

The possible experiments discussed above concern the determination of the parameters of the Maxwell model. The same procedure would be used if instead the generalized gas-surface interaction model is used. In order to use the generalized model, numerical methods would have to be employed throughout the analysis.

The ideal conditions considered above would not occur in practice. In the actual application of Method 1 of using past drag data, assumptions, which would introduce errors into the analysis, must be made in order to use data from different satellites. One assumption that may have to be made is that the gas-surface interaction is the same on all the satellites being used in the analysis. Also, in order to analyze data from satellites in non-circular orbits, an assumed atmospheric density model must be employed. The same model would also have to be employed in order to use any data from satellites which are in different orbits. In addition, the satellites would have to be assumed to be approximated by convex shapes, since there is at present no adequate method available to analyze concave shapes.

In light of the many assumptions which must be made in the analysis of existing satellite data, it is concluded that data from a large number of satellites would have to be analyzed and correlated in order to reduce the errors introduced by the assumption. The results of such an undertaking could, however, yield a considerable amount of information not only on the gas-surface interaction, but also on the validity of the assumptions used,

such as the atmospheric density model.

6.1.2. Method 2: Utilization of Data From a Single Satellite

The design, manufacture and launching of a satellite is an expensive operation and therein is the principal disadvantage to Method 2 in comparison to the less expensive analysis of existing data of Method 1. There are, however, many advantages to a Method 2 analysis which would utilize data from a satellite which is specifically designed to obtain information on the gas-surface interaction. The principle advantage would be the accuracy of results obtained, an accuracy which in all probability, could not be obtained in an analysis of past satellites.

In order to illustrate the basis of Method 2, consider the cone-disk satellite which was analyzed in chapter 5. The average drag and torque coefficients of the cone-disk satellite were of the following form in terms of the parameters of the Maxwell model.

$$\bar{C}_D = A_1 + A_2\alpha_d + A_3\alpha_d \sqrt{1-\alpha_T} \qquad 6.1$$

$$\bar{C}_{T_p} = B_1 + B_2\alpha_d + B_3\alpha_d \sqrt{1-\alpha_T} \qquad 6.2$$

$$\bar{C}_{T_s} = \alpha_d C \qquad 6.3$$

where $\bar{C}_D$ is the average drag coefficient, $\bar{C}_{T_p}$ is the average coefficient of torque which acts perpendicular to the satellite spin axis ($\bar{C}_{T_p}$ will be interpreted later as being the coefficient of either the i'_s or j'_s component of torque), and $\bar{C}_{T_s}$ is the average coefficient of slow down torque which is in the direction of the spin axis. The coefficients A_1, A_2, A_3, B_1, B_2, B_3,

and C are functions of λ, δ, and K as discussed in chapter 5.

Consider now, that D, T_p, and T_s are measurable quantities so that the following set of equations could be obtained

$$D^* = D/\tfrac{1}{2} U_\infty^2 \bar{A} = A_1 \rho + A_2 \rho \alpha_d + A_3 \rho \alpha_d \sqrt{1-\alpha_T} \tag{6.4}$$

$$T_p^* = T_p/\tfrac{1}{2} U_\infty^2 \bar{A} \bar{r} K = B_1 \rho + B_2 \rho \alpha_d + B_3 \rho \alpha_d \sqrt{1-\alpha_T} \tag{6.5}$$

$$T_s^* = T_s/\tfrac{1}{2} U_\infty^2 \bar{A} \bar{r} K = C \rho \alpha_d \tag{6.6}$$

in which D^*, T_p^*, and T_s^* are known from measurements. These three equations satisfy the two basic criteria established previously. Solutions for ρ, α_d, and α_T can be obtained analytically in terms of the measured quantities D^*, T_p^*, and T_s^* and the coefficients A_1, A_2, etc. These results are

$$\rho = \frac{T_p^* CA_3 - D^* CB_3 + T_s^* (A_2B_3 - A_3B_2)}{CE} \tag{6.7}$$

$$\alpha_d = \frac{+T_s^* E}{T_p^* CA_3 - D^* CB_3 + (A_2B_3 - A_3B_2) T_s^*} \tag{6.8}$$

$$\sqrt{1-\alpha_T} = \frac{-T_p^* CA_1 + D^* CB_1 - T_s^* (A_2B_1 - A_1B_2)}{T_s^* E} \tag{6.9}$$

where $E = A_3B_1 - A_1B_3$.

The cone-disk satellite is one example in which the aerodynamic properties do provide equations which satisfy the basic criteria. This is not generally true of other satellite shapes. For example, the sphere equations given in chapter 5 show that $\bar{C}_{T_p}$ and $\bar{C}_{T_s}$ for the sphere are not independent. In another example, the equations for the disk with both sides exposed show that $\bar{C}_{T_p}$ is zero and therefore the first criteria is not

satisfied.

As in Method 1, the Maxwell model is used as a convenient example. The technique of analysis is, however, also applicable to the determination of the parameters of the generalized model, if numerical methods are employed.

6.2. Accuracy of a Satellite Experiment

The accuracy of determining the gas-surface interaction parameters and the atmospheric density in a satellite experiment is, of course, dependent upon the accuracy of the measurements of the average satellite aerodynamic properties. The accuracy is also dependent, however, on the shape or shapes of satellites from which data is obtained. For example, if drag measurements were made on three satellites which differed only slightly from that of a sphere, a solution would not be possible because even minor errors in drag measurements would be greatly amplified. These factors are illustrated by taking the specific example of the cone-disk satellite used in the previous section.

The accuracy of determining the unknown parameters ρ, α_d, and α_T using a cone-disk satellite is dependent upon the accuracy of measuring D^*, T_p^* and T_s^*. An estimate of the errors in the determination of ρ, α_d, and α_T can be made by taking the first partial derivatives of each of the unknown parameters with respect to D^*, T_p^*, and T_s^*. Taking the derivatives of Equation 6.7, 6.8, and 6.9, the following estimation of the errors is obtained,

$$\frac{\Delta\rho}{\rho} = -\bar{C}_D \frac{B_3}{E} \frac{\Delta D^*}{D^*} + \bar{C}_{T_p} \frac{A_3}{E} \frac{\Delta T_p^*}{T_p^*} + \alpha_d \frac{(A_2B_3 - A_3B_2)}{E} \frac{\Delta T_s^*}{T_s^*} \qquad 6.10$$

$$\frac{\Delta\alpha_d}{\alpha_d} = -\bar{C}_D \frac{B_3}{E} \frac{\Delta D^*}{D^*} + \bar{C}_{T_p} \frac{A_3}{E} \frac{\Delta T_p^*}{T_p^*} + \left[1 + \alpha_d \frac{(A_2B_3 - A_3B_2)}{E}\right] \frac{\Delta T_s^*}{T_s^*} \qquad 6.11$$

$$\frac{\Delta\alpha_T}{\sqrt{1-\alpha_T}} = \frac{1}{\alpha_d}\left[\bar{C}_B \frac{2B_1}{E} \frac{\Delta D^*}{D^*} - \bar{C}_{T_p} \frac{2A_1}{E} \frac{\Delta T_p^*}{T_p^*} \frac{(2A_1 C_{T_\perp} - 2B_1 \bar{C}_D)}{E} \frac{\Delta T_s^*}{T_s^*}\right. \qquad 6.12$$

Assume that the absolute values of the measurement errors, $|\Delta D^*/D^*|$, $|\Delta T_p^*/T_p^*|$ and $|\Delta T_s^*/T_s^*|$ are all less than or equal to some maximum possible value of $|\Delta M/M|$. Then, for the worse case, when all the errors are added, the maximum possible errors in the determination of ρ, α_d, and α_T would be given by

$$\left|\frac{\Delta\rho}{\rho}\right| \leq \frac{1}{E}\left[\left|\bar{C}_D B_3\right| + \left|\bar{C}_{T_p} A_3\right| + \left|\alpha_d (A_2B_3 - A_3B_2)\right|\right] \left|\frac{\Delta M}{M}\right| \qquad 6.13$$

$$\left|\frac{\Delta\alpha_d}{\alpha_d}\right| \leq \frac{1}{E}\left[\left|\bar{C}_D B_3\right| + \left|\bar{C}_{T_p} A_3\right| + \left|1 + \alpha_d (A_2B_3 - A_3B_2)\right|\right]\left|\frac{\Delta M}{M}\right| \qquad 6.14$$

$$\left|\frac{\Delta\alpha_T}{\sqrt{1-\alpha_T}}\right| \leq \frac{1}{\alpha_d E}\left[\left|2\bar{C}_D B_1\right| + \left|2\bar{C}_{T_p} A_1\right| + \left|2\bar{C}_{T_p} A_1 - 2\bar{C}_D B_1\right|\right]\left|\frac{\Delta M}{M}\right| \qquad 6.15$$

The quantities multiplying $\left|\frac{\Delta M}{M}\right|$ on the right hand side of the above equations represent, for a given $|\Delta M/M|$, the maximum error which is associated with the shape and orientation of the satellite. That is, these quantities vary as a function of the cone half angle δ and the orientation of the satellite spin axis with respect to the orbit which is determined by the angle λ. Using numerical methods, the term multiplying $|\Delta M/M|$ in Equation 6.15 was evaluated and the results are shown plotted in Figure 6.1 as a function of λ for various values of δ.

Figure 6.1 shows that some λ-δ combinations are definitely better

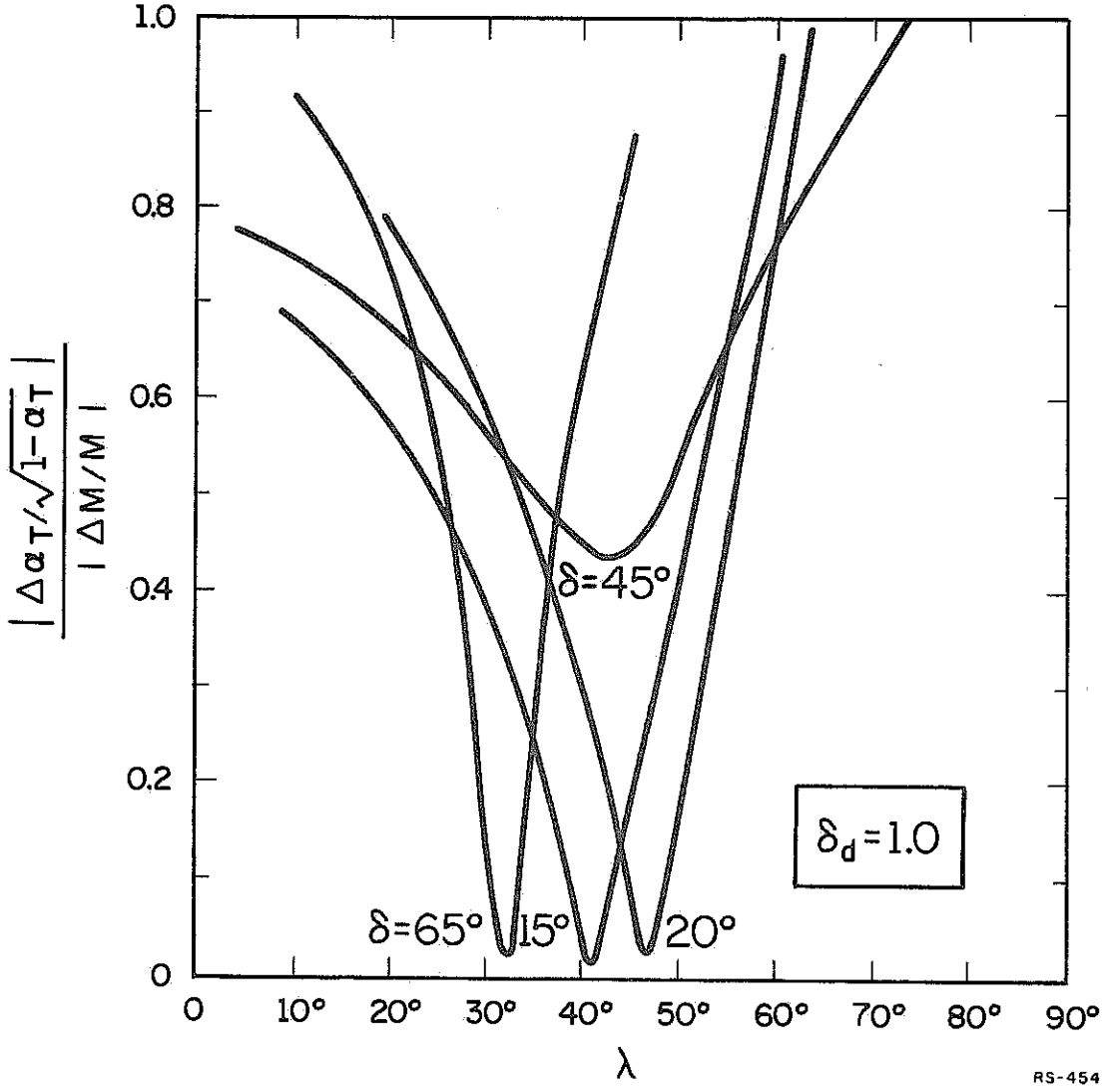

Figure 6.1. Maximum error in determining $\sqrt{1-\alpha_T}$ using a cone-disk shaped satellite as a function of λ and δ.

than others. In fact, for some combinations the coefficient of $|\Delta M/M|$ becomes large, implying that an experiment employing those λ-δ combinations would not yield acceptable results. The λ-δ combinations which give minimum possible error are, of course, the most desirable. Results similar to those shown in Figure 6.1 were also obtained for the error estimates of ρ and α_d. The error in determining α_T is directly related to the value of α_d, as seen in Equation 6.15. As α_d approaches zero, the error in the determination of α_T would become infinitely large. This is expected since for the Maxwell model the value of α_d determines the fraction of reflected force which is dependent upon the parameter α_T. Thus, as α_d becomes small, the effect of α_T on the force and torque on the satellite is greatly diminished. At $\alpha_d = 0$, the parameter α_T becomes meaningless.

The results shown in Figure 6.1 were obtained using the coefficients of the j_s' component of torque. Results were also obtained using the i_s' component of torque. Results were obtained for a wide range of δ values for both cases. These results showed the following in general

1. Utilization of measured values of the j_s' component of torque give consistently lower values of maximum possible error in the determination of ρ, α_d, and α_T, as compared to the results obtained utilizing measurements of the i_s' component of torque.
2. Values of λ greater than 45^o give lower error when the j_s' component of torque is utilized while values of λ less than 45^o give lower error when the i_s' component of torque is utilized.

3. The error in determining α_T is significantly different for using either the i_s'-or j_s'-component of torque. Use of the i_s'-component of torque was found to consistently give maximum error values of at least an order of magnitude greater than that obtained using the j_s'-component of torque.

The difference in possible accuracy between using either the i_s'-component or the j_s'-component of torque is best explained by referring to the numerical results given in Equations 5.27, 5.28, and 5.29. These equations show that the drag and the i_s'-component of torque are functionally similar in their dependence on the unknown ρ, α_d, and α_T. The j_s'-component of torque has, however, a functionally different dependence on the unknowns than either the drag or slow down torque. Therefore, even though it is possible to use either the i_s'- or j_s' - components of torque in an experiment, use of the j_s'-component of torque is more desirable in terms of the accuracy of the experiment.

The procedure just outlined can be used to find an optimum satellite design for performing a gas-surface interaction and atmospheric density experiment. In such an optimization study, factors such as size and weight requirements, orbital regression effects, and others would be considered in addition to the satellite shape. Considering only δ and λ, however, the cone-disk satellite was found to give a coefficient of $|\Delta M/M|$ in the range of 3-5 for each of the error estimates in ρ, α_d, and α_T. The inherent accuracy of this experiment is then very good since the errors in the measurements $|\Delta M/M|$ could be made small depending upon the magnitude of the measurable quantities and the measurement techniques employed. In addition, if

measurements at one altitude could be correlated with those made at other altitudes, the statistical error values could be made even lower. The correlation of measurements made at different altitudes would require the use of an assumed atmospheric density model. The magnitude of measurable quantities in a satellite experiment is discussed in the next section.

6.3. Magnitudes of Measurable Quantities in a Satellite Experiment

In a satellite experiment such as described above, the quantities D^*, T_p^*, and T_s^* would be determined from measurements made on the orbital decay rate, the satellite precession rate and the satellite spin decay rate. An estimate of the magnitudes of these rates can be determined from the example results obtained for the cone-disk satellite.

Consider first the determination of D^* which contains the drag D. For the case of circular orbits, assuming that the altitude losses due to drag effects are small, the decay rate of the orbital radius, r_o, can be approximated by the following expression given in Reference 1,

$$\frac{\Delta r_o}{rev} = - 4\pi B \rho_{av} (r_o)^2_{av} \qquad 6.16$$

where B is the ballistic coefficient $\bar{C}_D\bar{A}/2m$, m is the mass of the satellite, ρ_{av} is the average atmospheric gas density at the average orbital radius r_{av}. The mass m of the satellite is directly proportional to the density ρ_s of the material used to construct the satellite. Let the proportionality be expressed as

$$m = \rho_s r^*, \bar{A} \qquad 6.17$$

where $\bar{A}$ is the reference area of the satellite and r^*, has units of length and

measurements at one altitude could be correlated with those made at other altitudes, the statistical error values could be made even lower. The correlation of measurements made at different altitudes would require the use of an assumed atmospheric density model. The magnitude of measurable quantities in a satellite experiment is discussed in the next section.

6.3. Magnitudes of Measurable Quantities in a Satellite Experiment

In a satellite experiment such as described above, the quantities D^*, T_p^*, and T_s^* would be determined from measurements made on the orbital decay rate, the satellite precession rate and the satellite spin decay rate. An estimate of the magnitudes of these rates can be determined from the example results obtained for the cone-disk satellite.

Consider first the determination of D^* which contains the drag D. For the case of circular orbits, assuming that the altitude losses due to drag effects are small, the decay rate of the orbital radius, r_o, can be approximated by the following expression given in Reference 1,

$$\frac{\Delta r_o}{rev} = - 4\pi B \rho_{av} (r_o)^2_{av} \qquad 6.16$$

where B is the ballistic coefficient $\bar{C}_D\bar{A}/2m$, m is the mass of the satellite, ρ_{av} is the average atmospheric gas density at the average orbital radius r_{av}. The mass m of the satellite is directly proportional to the density ρ_s of the material used to construct the satellite. Let the proportionality be expressed as

$$m = \rho_s r^*, \bar{A} \qquad 6.17$$

where $\bar{A}$ is the reference area of the satellite and r^*, has units of length and

is the proportionality factor determined by the design of the satellite. Using Equation 6.17 and the definition of B, Equation 6.16 becomes, dropping the "av" subscripts on ρ and r_o,

$$\frac{\Delta r_o}{r_o}/\text{rev} = -D^* \frac{r_o}{\rho_s r^*} = -2\pi \bar{C}_D \frac{\rho\, r_o}{\rho_s r^*} \qquad 6.18$$

The convenient non-dimensional form of Equation 6.18 can also be obtained for the precession rate and slow down rate of the satellite. For high spin rates, the Euler equations for the dynamics of a spinning body under the action of external torques reduce to

$$T_{i_s'} = I_1 \Omega\, \omega_{i_s'} \qquad 6.19$$

$$T_{j_s'} = I_1 \Omega\, \omega_{i_s'} \qquad 6.20$$

$$T_{k_s'} = I_2 (\dot{\Omega} + \dot{\omega}_{k_s'}) \qquad 6.21$$

where I_1 is the moment of inertia about an axis perpendicular to the spin axis, I_2 is the moment of inertia about the spin axis, Ω is the spin rate and the terms $\omega_{j_s'}$, $\omega_{i_s'}$, and $\omega_{k_s'}$ represent the components of precession rate of the spinning body. Assume for the purposes of the present study that the satellite can be designed to be iso-inertial, $I_1 = I_2$, regardless of the external shape. In terms of the notation of the preceding chapters, the precession rate $\omega_{i_s'}$ is equal to $\dot{\lambda}$. Therefore, Equation 6.20 becomes

$$\Delta\lambda/\text{rev} = 2\pi\, \bar{T}_{i_s'}/\Omega I_1 \omega_o \qquad 6.22$$

where ω_o is the angular velocity of the orbit. The terms in Equation 6.22 can be expressed as follows

$$T_{i_s}' = C_{T_{j_s}} \frac{1}{2} \rho U_\infty^2 \bar{A} \bar{r}$$

$$\Omega = U_\infty K/\bar{r}$$

and

$$U_\infty = r_o \omega_o$$

substituting for $\bar{T}_{j_s}'$, ω_o, and Ω into Equation 6.22, the following is obtained

$$\Delta\lambda/\text{rev} = 2\pi \frac{\bar{C}_{T_{j_s}'}}{K} \rho r_o \frac{\bar{A} \bar{r}^2}{2I_1} \qquad 6.23$$

Similar to what was done for the drag case, assume that the moment of inertia is proportional to the material density of the satellite, ρ_s. Let

$$I_1 = \frac{1}{2} \rho_s \bar{A} \bar{r}^2 r_2^* \qquad 6.24$$

where r_2^* has units of length and is the proportionality factor. The quantity r_2^* may or may not be equal to the similar term r_1^* which was used for the drag equations. Substituting Equation 6.24 in Equation 6.23, the following is obtained

$$\Delta\lambda/\text{rev} = T_p^* \frac{r_o}{\rho_s r_2^*} = 2\pi \frac{\bar{C}_{T_{j_s}'}}{K} \frac{\rho r_o}{\rho_s r_2^*} \qquad 6.25$$

In a similar fashion, the satellite spin decay rate is found to be

$$\frac{\Delta\Omega}{\Omega}/\text{rev} = T_s^* \frac{r_o}{\rho_s r_3^*} = 2\pi \frac{\bar{C}_{T_{k_s}'}}{K} \frac{\rho r_o}{\rho_s r_3^*} \qquad 6.26$$

where the term r_3^* would be equal to r_2^* for an iso-inertial body.

Summarizing, the rates of change in the measurable quantities of a

satellite experiment are found expressible in the following non-dimensional forms.

$$\frac{\Delta r_o}{r_o}/\text{rev} = -2\pi \bar{C}_D \frac{\rho\, r_o}{\rho_s r_1^*} \tag{6.27}$$

$$\Delta\lambda/\text{rev} = 2\pi \frac{\bar{C}_{T_{j_s}'}}{K} \frac{\rho\, r_o}{\rho_s r_2^*} \tag{6.28}$$

$$\frac{\Delta\Omega}{\Omega}/\text{rev} = 2\pi \frac{\bar{C}_{T_{k_s}'}}{K} \frac{\rho\, r_o}{\rho_s r_3^*} \tag{6.29}$$

The products $\rho_s r_1^*$, $\rho_s r_2^*$, and $\rho_s r_3 s^*$ are quantities which may be controlled by the satellite design. In general, large solid satellites would have $\rho_s r^*$ values which are large whereas light satellites would have small values of $\rho_s r^*$. In terms of orders of magnitude, an upper limit for a large solid satellite would be in the order of 100 gm/cm^2. A lower limit for $\rho_s r^*$ could be 10^{-2} gm/cm^2 for a thin walled hollow satellite.

The product $\rho\, r_o$ varies, of course, with the orbital altitude of the satellite. Figure 6.2 shows the variation of $\rho\, r_o$ for a high, low, and medium density atmosphere versus the orbital altitude h, where $h=r_o-r_e$; r_e = (radius of Earth).

Using some representative values of $\bar{C}_D$, $\bar{C}_{T_{j_s}'}$, and $\bar{C}_{T_{k_s}'}$, which were obtained in the numerical studies of chapter 5 on the cone-disk satellite, the plots given in Figures 6.3, 6.4, and 6.5 show how the measurable quantities vary with altitude h, for $\rho_s r^* = 1$. Figure 6.3 can also be interpreted in terms of $\Delta\tau/\tau$, the rate of change in the period of the orbit. The rate of change in period is related to the altitude decay rate by the

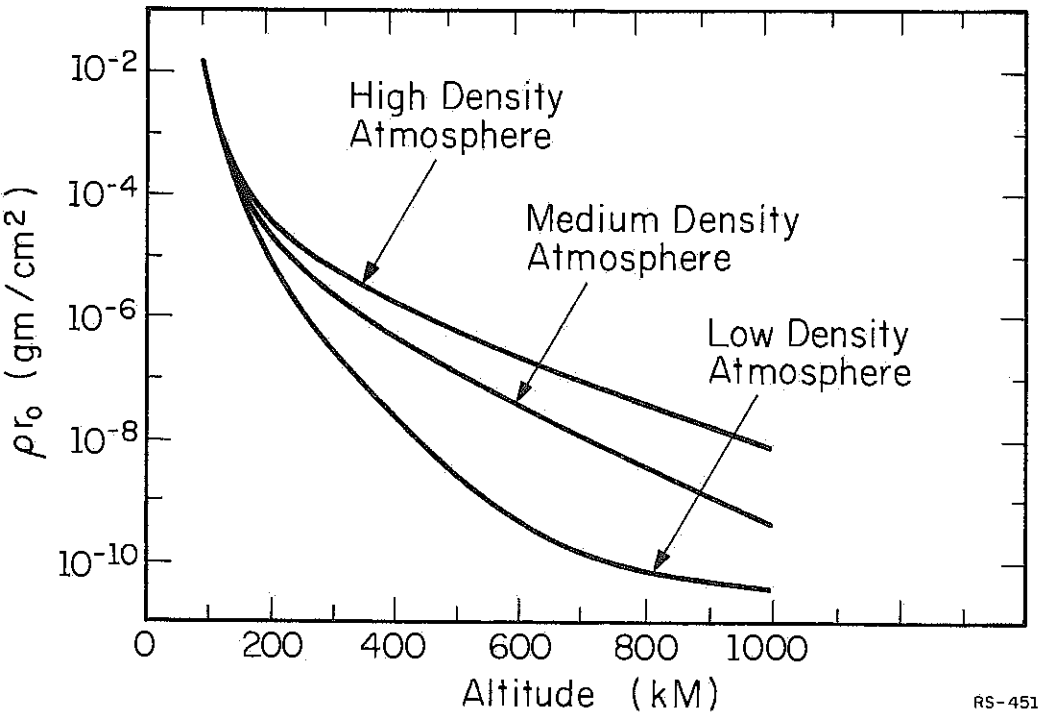

Figure 6.2. High, low, and medium atmospheric density variation with altitude (from tables in Reference 29).

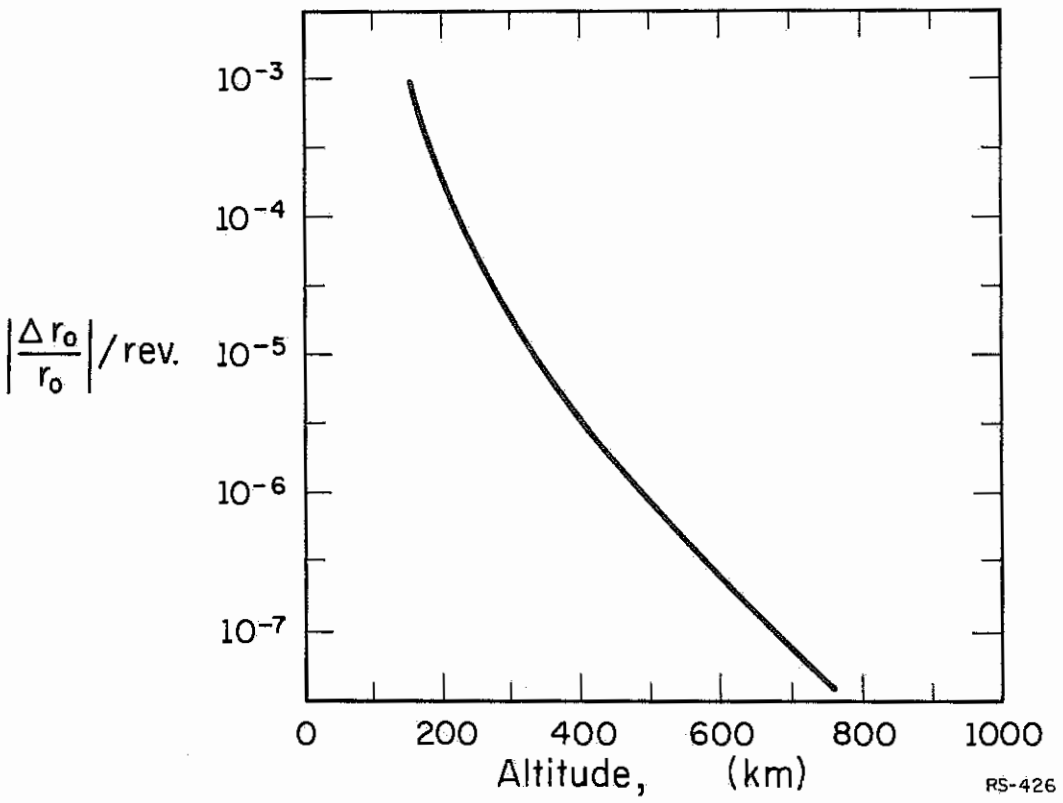

Figure 6.3. Relative average altitude loss per (circular) orbit for a cone-disk satellite.

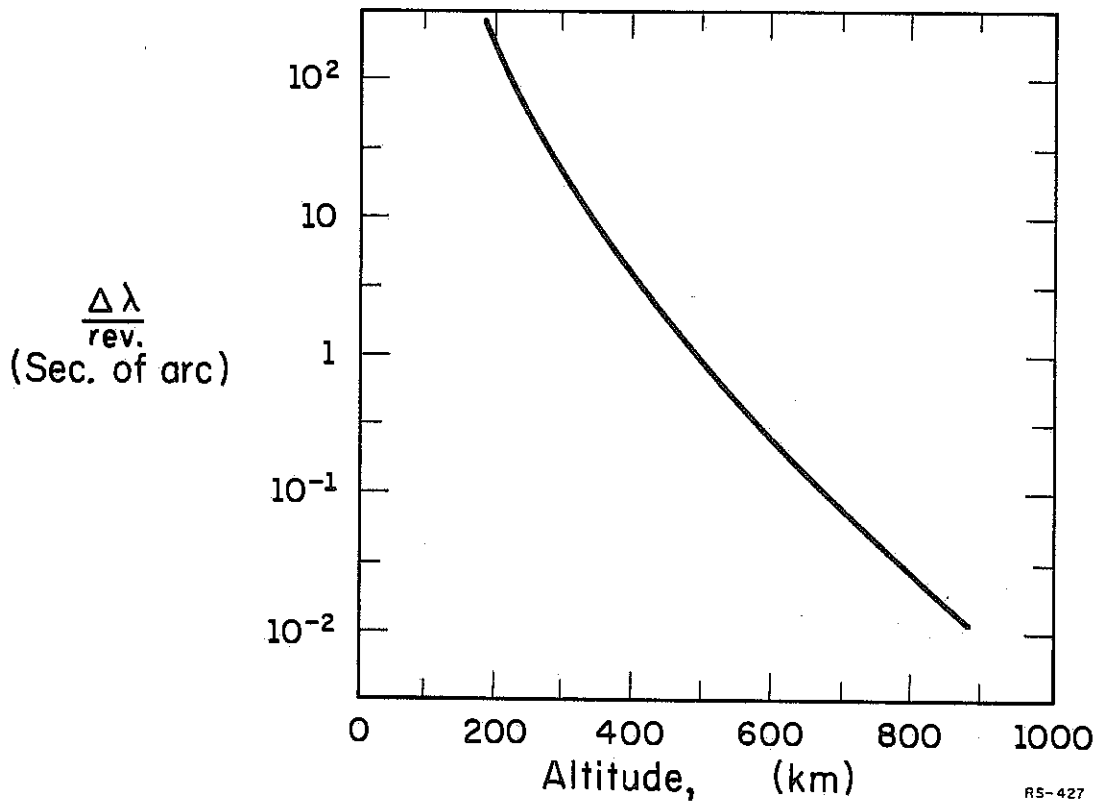

Figure 6.4. Relative average angular precession of spin-axis of a cone-disk satellite per (circular) orbit.

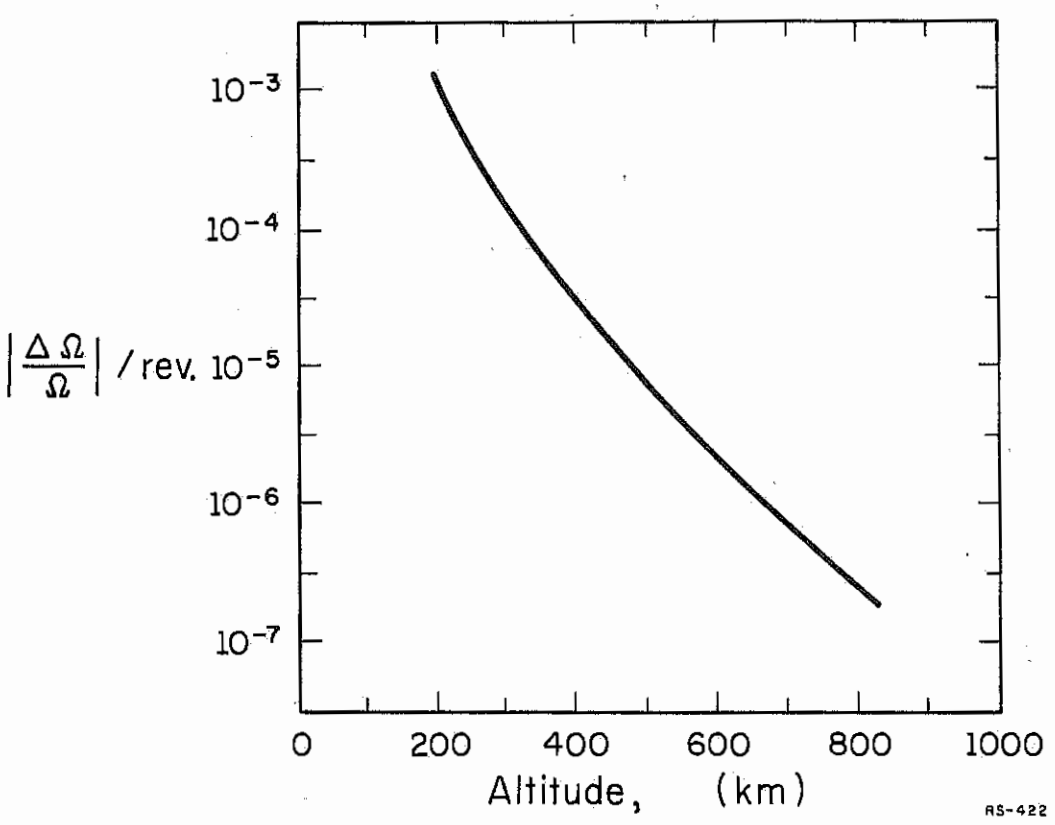

Figure 6.5. Relative average spin decay of a cone disk satellite per (circular) orbit.

following equation,

$$\frac{\Delta\tau}{\tau}/\text{rev} = \frac{3}{2}\ \frac{\Delta r_o}{r_o}/\text{rev} \qquad 6.30$$

The results shown in Figure 6.4 are given in terms of sec of arc/rev.

The results given in Figures 6.3, 6.4, and 6.5, clearly illustrate the feasibility of proposed experimental techniques in terms of the magnitude of measurable quantities. In fact, the measurements could all be made using an optical technique such as that proposed by the Coordinated Science Laboratory.[12,13] The advantage to an optical readout system is that the satellite itself could be completely passive in that sunlight reflected off the surface of the satellite can be used to determine the orientation of the spin axis and thus be able to determine the precession rate of the satellite spin axis. The technique proposed by CSL is fully described in the References 12 and 13. The results of this extensive study made by CSL of the feasibility of the optical readout technique indicate that precession rates of the order shown in Figure 6.4 would be well within the capabilities of the optical technique. Satellite spin rate data could be obtained directly from the observations of reflected sunlight from the satellite. The optical technique is, of course, a standard method of obtaining orbital drag data.

6.4. Assessment of Results Obtained From a Satellite Experiment

In the preceding discussions, a satellite experiment to determine the parameters of the Maxwell model was studied mainly to illustrate its feasibility. However, the accuracy of the interpretation of the measurements depends upon how well the assumed model approximates the actual reflection phenomena.

In order to illustrate how, for a special case, erroneous results could be obtained, take an experiment in which the measurements are interpreted in terms of the parameters of the Maxwell model. As an extreme case consider that the actual reflection process is a perfect backscatter. That is, irrespective of the angle, θ, at which the molecules impinge on the surface, the molecules are always reflected back in the same direction. Perfect backscatter is a type of reflection which cannot be approximated by the Maxwell model (or the Schamberg model either).

The procedure outlined for an experiment using a cone-disk satellite would yield values of α_d, α_T, and ρ for this extreme case of perfect backscatter; however, it can be shown that α_d and α_T would be equal to one and the gas-density would be <u>twice</u> its actual value.

The above example serves to illustrate the importance of interpreting the satellite measurements in terms of a model, such as the generalized model, which can cover a wide range of possible gas-surface interactions. In the range of possible reflections between specular and diffuse, the results of chapter 4 indicate that use of either the generalized model or the Maxwell model could be expected to yield results which could reasonably approximate the actual reflection process. For the case of backscatter or over specular reflections, however, use of either the Maxwell or the Schamberg model could not be expected to yield valid results on the gas surface interaction parameters. The Nocilla model also could give erroneous results if the actual distribution function were far from the drifting Maxwellian assumed by Nocilla.

Solutions for the unknowns when the generalized model is used

must be obtained using numerical methods since in general the resulting equations are trigometric in the parameter P_j. Trigometric equations can, however, lead to multiple solutions for a given set of measurements. If multiple solutions are obtained, then additional experiments would have to be performed which are designed to detect the correct solution. It must be concluded that, even considering the possibility of multiple solutions, the use of the generalized model in the interpretation of satellite data is to be favored over the use of a given particular model. More specific models could be employed after the analysis using the generalized model has indicated the general character of the reflection process.

In order to illustrate the application of the generalized model, consider a reflection which is assumed to be composed of <u>three</u> separate beams; beam 1 (j=1) is in the backscatter direction (P_1=2), beam 2 (j=2) is normal to the surface (P_2=1), and beam 3 (j=3) is in the specular direction (P_3=0) (see Figure 6.8). The effect on the drag of a body due to a reflection of this type can be determined from the equations given in section 4.3.1. For the values of P_j given above, the drag coefficient for a flat plate, cylinder, cone and sphere are given by,

$$(C_D)_{plate} = \sin\theta_s \left(2 + 2\sigma_1\sqrt{1-\alpha_1} + 2\sin\theta_s\,\sigma_2\sqrt{1-\alpha_2} - 2\cos 2\theta_s\,\sigma_3\sqrt{1-\alpha_3}\right) \quad 6.31$$

$$(C_D)_{cylinder} = 2 + 2\sigma_1\sqrt{1-\alpha_1} + \frac{\pi}{2}\sigma_2\sqrt{1-\alpha_2} + \frac{2}{3}\sigma_3\sqrt{1-\alpha_3} \quad 6.32$$

$$(C_D)_{cone} = 2 + 2\sigma_1\sqrt{1-\alpha_1} + 2\sin\delta\,\sigma_2\sqrt{1-\alpha_2} - 2\cos 2\delta\,\sigma_3\sqrt{1-\alpha_3} \quad 6.33$$

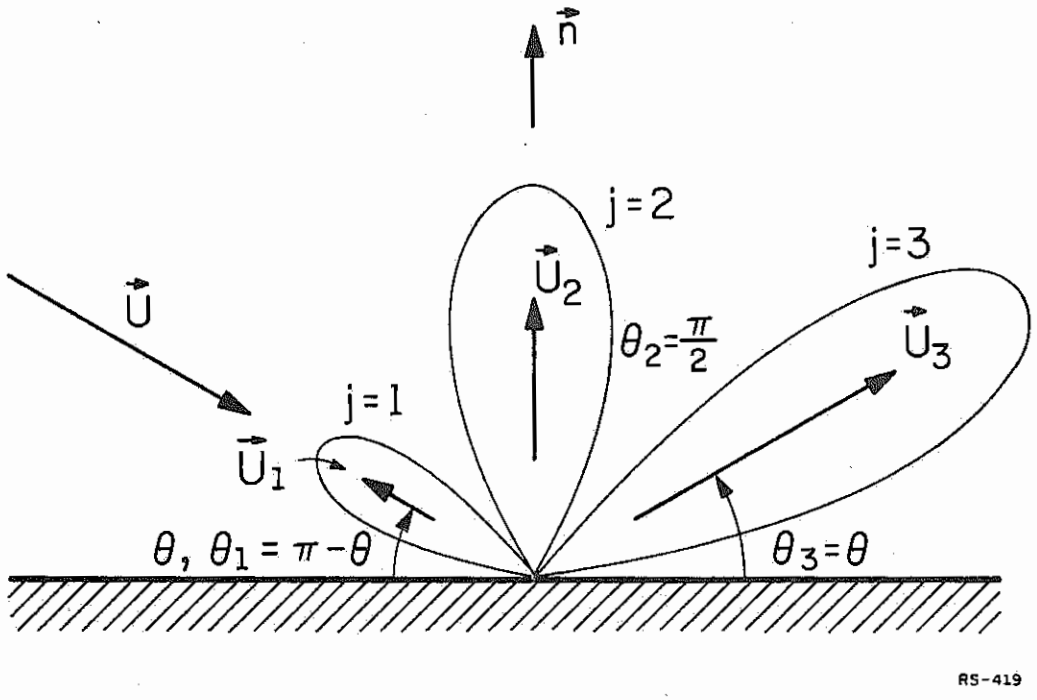

Figure 6.6. Notation for a possible three-lobed reflection.

$$(C_D)_{sphere} = 2 + 2\sigma_1\sqrt{1-\alpha_1} + \frac{4}{3}\sigma_2\sqrt{1-\alpha_2} \qquad 6.34$$

These results serve to illustrate the statement made at the end of chapter 2 that the aerodynamic properties are specified by a choice of only two quantities for each reflected beam; P_j and $\sigma_j\sqrt{1-\alpha_j}$. The above equations show that the quantities σ_j and $\sqrt{1-\alpha_j}$ always appear as the product in the expressions for aerodynamic properties and could therefore be considered as a single parameter.

The results given in Equations 6.31, 6.32, 6.33, and 6.34 also illustrate that, without prior knowledge of either σ_j or α_j, only the quantities $\sigma_j\sqrt{1-\alpha_j}$ could be determined in an experiment which utilizes measured aerodynamic properties of convex shapes. In application to satellite experiments then, if no assumptions are made on the distribution function of reflected molecules (such assumptions are made in the Maxwell, Schamberg and Nocilla models), the results of a satellite experiment using convex shapes are limited to obtaining information on the number of reflected beam components, the magnitude of each component, and the direction of each component. This information, even though limited, would be sufficient to determine the aerodynamic drag, lift, and torque properties of any convex shaped body, spinning or non-spinning. Such information would also be utilized to design future satellite experiments to obtain more refined information on the gas surface interaction. Although such shapes are not considered in this study, it is proposed that concave shapes could be utilized to obtain information on the distribution function of reflected molecules since the aerodynamic properties of these shapes are dependent upon the properties of reflected distribution.

6.5. Significance of Satellite Experiments to Determine Gas-Surface Interaction Parameters and the Atmospheric Density

The examples given in this chapter have employed idealized conditions such as circular orbits and constant density which would not be the case in an actual experiment. As mentioned in the introduction to this chapter, a number of uncertainties are associated with satellite experiments which can affect the interpretation of results. Two of the major uncertainties have already been adequately discussed; the uncertainty associated with the atmospheric density was discussed in the introduction and the uncertainties associated with the gas-surface interaction model has been discussed in the preceding section. The significance of performing a satellite experiment in light of some additional uncertainties will be discussed here. To be considered are uncertainties concerning the condition of the satellite surface (ie. degree of surface contamination by adsorbed gases, composition of surface-adsorbed gases, and roughness of surface), composition of the atmosphere, and variation of atmospheric density with altitude.

6.5.1. Consideration of Surface Conditions

The gas-surface interaction is known to depend upon the degree and composition of adsorbed surfaces (see, for example, the experimental results given in Reference 30) which, in the satellite environment, is not well known. The satellite environment in some respects acts like a cleansing environment in that the very high vacuum combined with the effects of high energy solar and cosmic rays tend to rid the surface of trapped gas molecules. On the other hand, the constant bombardment of high velocity gas

molecules as the satellite travels in its orbit causes the surface to again be contaminated with trapped gas molecules. The cleansing and contaminating processes take place continuously. The equilibrium conditions if reached have not as yet been determined. This uncertainty enters the interpretation of results when measurements made at one orbital altitude are correlated to those made at other altitudes.

Instead of treating the surface conditions as uncertainties in the experiment, it is suggested that a satellite experiment be designed to obtain information on the uncertainties. One possible approach is to first contaminate the satellite surface with a known contamination which would be expected to degas at a known rate in the relative vacuum of the orbital environment. The degassing rate could then be correlated with the measured rates of change in the aerodynamic properties of the satellite to determine the effect of contamination on the gas-surface interaction. That such an approach would be feasible is indicated first by the results obtained in this chapter on the possible accuracy of a satellite experiment. Secondly, in some preliminary studies performed by Cohen[31], it was concluded that contaminates such as water vapor on a metal surface could be expected to degas down to 1/e of the initial surface coverage in a time of about 5 to 10 weeks. This rate of change estimate combined with the expected accuracy of the satellite measurements indicates that such an experiment may be feasible.

The effects of other surface properties on the gas–surface interaction could also be studied by making accurate measurements of the aerodynamic properties as a function of time and then correlating the results

with known variations of the environmental conditions. For example, for satellites with long lifetimes, the satellite surface could be expected to become rougher with time due to the bombardment of micrometeorites, dust particles and high energy cosmic rays (see for example Reference 32). The effect of the gas-surface interaction on surface roughness could then be assessed by correlating changes in the satellite aerodynamic properties with what is known about the roughening effects of the space environment. Data from satellites which have changing, or controlled surface temperatures could be utilized in a similar manner to obtain information on the effect of surface temperature.

6.5.2. Consideration of the Composition of the Atmosphere

The composition of the earth's atmosphere is known to vary considerably with altitude and solar activity (see for example Reference 29). The average molecular weight at 1000 km. varies from 1.47 for a low-density atmosphere to a value of 15.04 for a high density atmosphere. At 300 km. the variation is from 16.89 to 22.46 for the low and high density atmospheres. (Values of molecular weight obtained from Reference 29). As a satellite orbit decays, then, the species of gas molecules which impinge on the satellite surface will change in concentration. The change in gas-species concentration with altitude enters into the interpretation of results when measurements made at one altitude are correlated to those made at other altitudes. Two uncertainties are involved; the gas-surface interaction as a function of gas-species concentration and the concentration of gas-species as a function of altitude.

As with the uncertainties in surface conditions, it is proposed here that the uncertainties in the atmospheric composition be considered unknown and be determined by satellite experiments. One possible approach is to consider each species of gas separately. That is, instead of the average density of the atmosphere, ρ, consider that the free stream density is composed of a separate density, ρ_i, for each species where $\rho = \Sigma\rho_i$. In addition, for each species of gas, i, consider the gas-surface interaction to be determined by parameters of the generalized model $(\sigma_j\sqrt{1-\alpha_j})_i$ and $(P_j)_i$. For example, the drag of a non-spinning sphere would then be given by

$$\frac{D_{sphere}}{\frac{1}{2} U_\infty^2 \bar{A}} = \sum_i \rho_i \left\{ 2 + \sum_j (\sigma_j\sqrt{1-\alpha_j})_i \left[\frac{4(1-\cos\frac{\pi}{2}(P_j)_i)}{(P_j)_i(4-(P_j)_i)} \right] \right\} \qquad 6.35$$

Expressions such as Equation 6.31 could also be developed for other satellite shapes. Then, using the same procedures as outlined earlier in this chapter, it is proposed that the unknowns ρ_i, $(P_j)_i$, and $(\sigma_j\sqrt{1-\alpha_i})_i$ could be determined from measurements made on the aerodynamic properties of satellites. Certainly for such a large number of unknowns, a single satellite experiment would not provide sufficient information for the determinations. However, a number of properly designed satellites could be utilized along with a careful re-evaluation of past drag data to obtain a considerable amount of information on the unknowns. The values of ρ_i could be correlated with models of the variation in the composition of the atmosphere to determine which model, if any, gives the most consistent results. Such an analysis would then provide information on both the atmospheric composition and the gas-surface interaction as a function of gas-species.

6.5.3. Variation of Atmospheric Density Models

In the determination of the atmospheric density, a model of the relative variation of atmospheric density with altitude must be assumed. Such a model must be utilized in the analysis of elliptic orbits and also in correlating measurements made at one altitude with those made at other altitudes. An error in the determination value of ρ is then introduced due to the uncertainty associated with the assumed model of the atmosphere.

As with the other uncertainties in a satellite experiment, it is suggested that this uncertainty could also be removed by a number of satellite experiments and re-evaluation of past drag data. The procedure would be much the same as outlined in the previous section on atmospheric composition models.

7. SUMMARY AND CONCLUSIONS

A generalized model of the gas-surface interaction was developed to cover a wide range of possible interactions. This model was incorporated into the aerodynamic equations of spinning convex bodies in a free molecule flow in order to study fully the influence of the gas-surface interaction on the aerodynamic properties of satellites in this flow regime.

Analysis of the aerodynamic properties of four spinning bodies, (disk, cylinder, cone, and sphere) at angles of attack revealed the strong influence of the gas-surface interaction, especially on the torque properties. The aerodynamic torque acting on a body in free molecular flow was found to be caused by 1) the moment of drag and lift forces about the center of mass of the body and 2) forces tangent to the surface induced by the spinning of the body. Aerodynamic torques of the first type are experienced by both spinning and non-spinning satellites and are well known. Aerodynamic torques of the second type which are spin induced have components both parallel and perpendicular to the spin axis of the body. The component of torque parallel to the spin axis would cause the expected decay in the spin rate of a spinning body. The components of torque perpendicular to the spin axis would cause a gyroscopic precession. The spin induced torque on a body was found to be more strongly dependent on the gas-surface interaction than aerodynamic torques of the first type.

Spin induced effects were also found in the aerodynamic drag and lift properties of spinning bodies at angles of attack. In general, it was found that spinning bodies experience higher values of drag and lift than do

non-spinning bodies. Also of interest is a lateral force experienced by spinning bodies in free molecular flow which is entirely spin induced. The spin induced lateral force was found to be also strongly dependent on the gas-surface interaction, as for the spin induced aerodynamic torques. The aerodynamic, spin induced lateral force is analogous, but opposite in direction, to the Magnus effect on spinning bodies in viscous flow.

The development of the generalized gas-surface interaction model and the analysis of aerodynamic properties of spinning bodies formed the basis for proposing satellite experiments to obtain information on the gas-surface interaction as well as the orbital atmospheric density. It was found that the average aerodynamic properties of spinning satellites are strongly dependent on the parameters of a given gas-surface interaction model. It is, therefore, proposed that the measured average aerodynamic properties of spinning satellites be utilized to determine precise values of the gas-surface interaction parameters and the orbital gas density. The preliminary phase of the study of the feasibility of these satellite experiments was conducted. This phase of the study covered 1) the consideration of schemes utilizing the aerodynamic properties of satellites of various shapes and orientations, 2) the assessment of the accuracy of determining the gas surface-interaction parameters and the orbital gas density, 3) the estimate of the magnitude of measurable quantitites in a satellite experiment, and 4) the investigation of the possible effects on accuracy introduced by uncertainties in the space environment and satellite surface conditions. On the basis of these results, it was established that the proposed satellite experiments are feasible and could provide significant information on both the gas-surface

interaction at satellite velocities and the near-earth atmosphere.

Due to the considerable uncertainties associated with the gas-surface interaction at satellite velocities, it was found that the generalized model of the gas-surface interaction is necessary in the interpretation of results of the proposed satellite experiments. Since the aerodynamic properties of convex bodies in a free mol. flow are not dependent on the specific form of the distribution of reflected molecules, gas-surface interaction models which incorporate a specific distribution function are not only unnecessary but also undesirable in that considerable error can be introduced in the interpretation of aerodynamic measurements by using such models. For this reason, the use of the generalized model developed in this study is preferred since no assumption was made on the distribution of reflected molecules other than the existance of an average velocity and direction. It was suggested that the generalized model could also be applied to the interpretation of results obtained from laboratory experiments in order to parameterize in a general manner the results of molecular beam studies. The parameterization of these results would facilitate the comparison of the various results and could serve as a basis for suggesting more precise gas-surface interaction models. Laboratory experiments on gas-surface interaction which measure forces and torques are particularly suitable in using the generalized model to interpret the results.

The study of feasibility of the satellite experiments proposed in this study has been supported by the National Aeronautics and Space Administration at the George Marshall Space Flight Center. The aerodynamic properties of near-earth satellites are of major importance in determining both

the lifetime of a satellite and the motion of the satellite about its center of mass. Since NASA is planning in the future to orbit satellites of larger size (such as manned space stations) and satellites requiring greater orientation stability than satellites of the past, there is an urgent need for precise knowledge of the character of the gas-surface interaction and the composition of the atmosphere in order to properly and economically design these future satellites. For this reason, NASA is considering an extensive experimental program called Project ODYSSEY[33,34] which is planned to obtain information on the gas-surface interaction and the orbital environment by a number of satellite experiments. The techniques of analysis developed and the results obtained in this study have direct application to the design of satellite experiments and the interpretation of results of these experiments, as well as the interpretation of existing satellite data, with the objective to obtain information on the gas-surface interaction and the atmospheric composition.

REFERENCES

1. National Aeronautics and Space Administration, Space Flight Handbooks, Vol. 1, Orbital Flight Handbook, NASA SP 33, Part 1, (1963).

2. Anderson, Andres, and Fenn, "High Intensity and High Energy Molecular Beams," Advances in Atomic and Molecular Physics, Vol. 1, (1965), pp. 345-389.

3. Moe, K. "Absolute Atmospheric Densities From the Spin and Orbital Decays of Explorer, VI" Planet, Space Science, Vol. 14, (1966), pp. 1062-1075.

4. Beletskii, Marov, and Zmievskaya, "On Determination of Atmosphere Parameters from Drag Data of the Satellite PROTON-2, Its Orientation Being Taken Into Account" Symposium on Satellite Dynamics - XII COSPAR Session, Prague, (1969).

5. Sentman, L. H., "Free Molecule Flow Theory and Its Application to the Determination of Aerodynamic Forces," Lockhead Missiles and Space Company, Report LMSC-448514, October (1961).

6. Hurlbut and Sherman, "Application of the Nocilla Wall Reflection Model to Free-Molecule Kinetic Theory," The Physics of Fluids, Vol. 11, No. 3, (1968) pp. 486-496.

7. Evans, W. J., "Aerodynamic and Radiation Disturbance Torques on Satellites Having Complex Geometry" Torques and Attitude Sensing in Earth Satellites, ed. by Singer, Academic Press, (1964) pp. 83-98.

8. Leon and Reiter, "Effect of Aerodynamic Moment on Spin Rate of Able-3 Payload," GM 59-802 1.2-54, Space Technology Laboratories, Inc. (Now TRW) (1959).

9. Karr and Yen, "Aerodynamic Torque on a Spinning Spherical Satellite with Application to Measurement of Accommodation Coefficients," Astronautica Acta, Vol. 14, (1969) pp. 131-142.

10. Palamara, R. D. "Some Considerations for a Simplified Orbiting General Relativity Experiment," AIAA Journal, Vol. 4, No. 6, (1966) pp. 1036-1043.

11. Nan Tum Po, "On the Rotational Motion of a Spherical Satellite Under the Action of Retarding Aerodynamical Moments," NASA TTF-9630, (1965).

12. Cooper, Karr, Myers, and Skaperdas, "A Proposed Test of the Einstein Theory of Gravitation by Means of an Unshielded Orbiting Gyro Using Passive Telemetry," Report R-378, Coordinated Science Laboratory, University of Illinois, (1968).

13. Myers, Jr., J. L., "Optimization of a Gyroscopic Satellite General-Relativity Experiment," MacDonnell Douglas Corp., Douglas Paper 10086, (1969) (presented to Symposium on Astrodynamics and Related Planatary Sciences, April, 1969, Washington, D.C.).

14. Nocilla, Silvio, "The Surface Re-Emission Law in Free Molecular Flow," Rarefied Gas Dynamics, Third Symposium, Vol. 1 (1963), pp. 327-346.

15. Schamberg, R., "A New Analytic Representation of Surface Interaction with Hypothermal Free Molecule Flow with Application to Neutral-Particle Drag Estimates of Satellites," RAND Research Memorandum, RM-2313, (1959).

16. Hurlbut and Beck, University of California, Eng. Prog. Report HE-150-166, (1959).

17. Moran, Wachman, and Trilling, "Scattering of Monoenergetic Argon from Heated Platimum: Planer Time-of-Flight Measurements," The Physics of Fluids, Vol. 12, No. 5, (1969), pp. 987-993.

18. Boring and Humphris, "Momentum Transfer to Solid Surfaces by N_2 Molecules in the Energy Range 7-200 ev." Rarefied Gas Dynamics, Sixth Symposium, Vol. II, (1969), pp. 1303-1310.

19. Becker, Introduction to Theoretical Mechanics, McGraw-Hill, (1954).

20. TRW Space Logs, published quarterly by the TRW Systems Group, Relando Beach, California.

21. Schlichting, Boundary Layer Theory, 4th ed. McGraw-Hill (1960) pp. 267-268.

22. Abramowitz and Stegun, Handbook of Mathematical Functions, Dover Publications (1965).

23. Cook, G. E., "Drag Coefficients of Spherical Satellites," Royal Aircraft Establishment Technical Report No. 65218, Ministry of Aviation, Farnborough Hants, (1965).

24. Moulton, F. R., Celestial Mechanics, 2nd ed., MacMillan Co., (1914).

25. Danby, J. M. A., Fundamentals of Celestial Mechanics, MacMillian Co., (1962).

26. Sterne, T. E., An Introduction to Celestial Mechanics, Interscience Pub. (1960).

27. Sentman and Neice, "Drag Coefficients for Tumbling Satellites," Journal of Spacecraft, Vol. 4, No. 9, (1967), pp. 1270-1272.

28. King-Hele and Quinn, "Upper-Atmosphere Density, Determined From the Orbits of Cosmos Rockets," Planetary and Space Sciences, Vol. 14, (1966), pp. 1023-1033.

29. Johnson, F. S., "Structure of the Upper Atmosphere," Satellite Environment Handbook, Stanford University Press, Stanford, (1961).

30. O'Keefe and French, "High Energy Scattering of Inert Gases from Well Characterized Surfaces I Experimental," Rarefied Gas Dynamics, Sixth Symposium, Vol. II, (1969), pp. 1279-1296.

31. Coordinated Science Laboratory, Progress Report for September 1968, through June 1969, CSL, University of Illinois, Urbana, pp. 141-144.

32. McKeown, D., "Surface Erosion in Space," Rarefied Gas Dynamics, Third Symposium, Vol I., (1963), pp. 315-326.

33. Youngblood and Walters, in Proc. 3rd. Natl. Conf. Aerospace Meteorology, Am. Met. Society, Boston, 1968.

34. Reiter and Moe, "Surface Particle-Interaction Measurement Using Paddlewheel Satellites," Rarefied Gas Dynamics, Sixth Symposium, Vol. II, (1969), pp. 1543-1555, (Project ODYSSEY is discussed on pp. 1547-1549).

VITA

Gerald Ray Karr was born on June 28, 1942, in Gibson City, Illinois. He entered the University of Illinois in 1960 where he received a financial scholarship and the Air Foundation Scholarship in 1964. He received the Bachelor of Science degree in Aeronautical and Astronautical Engineering in 1964 from the University of Illinois at Urbana. He was then appointed, and has since remained, a graduate research assistant in the Coordinated Science Laboratory at the University of Illinois. In 1966, he received the Master of Science degree in Aeronautical and Astronautical Engineering from the University of Illinois. In the spring semester of 1968 he was a teaching assistant for the Aeronautical and Astronautical Engineering Department.

Gerald R. Karr is co-author of a paper entitled "Aerodynamic Torque on a Spinning Spherical Satellite with Application to Measurement of Accommodation Coefficients," which was published in Astronautica Acta, Vol. 14, pp. 131-142, 1969.

Gerald R. Karr is a member of Sigma Gamma Tau, an associate member of Sigmi Xi, and a student member of the American Institute of Aeronautics and Astronautics.

Distribution List as of 1 September, 1969

Dr A.A. Dougal
Asst Director (Research)
Ofc of Defense Res & Eng
Department of Defense
Washington, D.C. 20301

Office of Deputy Director
(Research and Information, Rm 3D1037)
Department of Defense
The Pentagon
Washington, D.C. 20301

Director, Advanced Research Projects
Agency
Department of Defense
Washington, D.C. 20301

Director for Materials Sciences
Advanced Research Projects Agency
Department of Defense
Washington, D.C. 20301

Headquarters
Defense Communications Agency (340)
Washington, D.C. 20305

Defense Documentation Center
Attn: DDC-TCA
Cameron Station
Alexandria, Virginia 22314 (50 Copies)

Director
National Security Agency
Attn: TDL
Fort George G. Meade, Maryland 20755

Weapons Systems Evaluation Group
Attn: Colonel Blaine G. Vogt
400 Army-Navy Drive
Arlington, Virginia 22202

Central Intelligence Agency
Attn: OCR/DD Publications
Washington, D.C. 20505

Hq USAF (AFRDD)
The Pentagon
Washington, D.C. 20330

Hq USAF (AFRDDE)
The Pentagon
Washington, D.C. 20330

Hq USAF (AFRDSD)
The Pentagon
Washington, D.C. 20330

Colonel E.F. Gaines, Jr.
ACDA/FO
1901 Pennsylvania Ave N.W.
Washington, D.C. 20451

Lt Col R.B. Kalisch (SREE)
Chief, Electronics Division
Directorate of Engineering Sciences
Air Force Office of Scientific Research
Arlington, Virginia 22209

Dr I.R. Mirman
AFSC (SCT)
Andrews Air Force Base, Maryland 20331

AFSC (SCTSE)
Andrews Air Force Base, Maryland 20331

Mr Merton H. Pavane, Chief
AFSC Scientific and Technical Liaison Office
26 Federal Plaza, Suite 1313
New York, New York 10007

Rome Air Development Center
Attn: Documents Library (EMTLD)
Griffiss Air Force Base, New York 13440

Mr H.E. Webb (EMMIS)
Rome Air Development Center
Griffiss Air Force Base, New York 13440

Dr L.M. Hollingsworth
AFCRL (CRW)
L.G. Hanscom Field
Bedford, Massachusetts 01730

AFCRL (CRMPLR), Stop 29
AFCRL Research Library
L.G. Hanscom Field
Bedford, Massachusetts 01730

Hq ESD (ESTI)
L.G. Hanscom Field
Bedford, Massachusetts 01730 (2 copies)

Professor J. J. D'Azzo
Dept of Electrical Engineering
Air Force Institute of Technology
Wright-Patterson AFB, Ohio 45433

Dr H.V. Noble (CAVT)
Air Force Avionics Laboratory
Wright-Patterson AFB, Ohio 45433

Director
Air Force Avionics Laboratory
Wright-Patterson AFB, Ohio 45433

AFAL (AVTA/R.D. Larson
Wright-Patterson AFB, Ohio 45433

Director of Faculty Research
Department of the Air Force
U.S. Air Force Academy
Colorado Springs, Colorado 80840

Academy Library (DFSLB)
USAF Academy
Colorado Springs, Colorado 80840

Director
Aerospace Mechanics Division
Frank J. Seiler Research Laboratory (OAR)
USAF Academy
Colorado Springs Colorado 80840

Director, USAF PROJECT RAND
Via: Air Force Liaison Office
The RAND Corporation
Attn: Library D
1700 Main Street
Santa Monica, California 90045

Hq SAMSO (SMTTA/Lt Nelson)
AF Unit Post Office
Los Angeles, California 90045

Det 6, Hq OAR
Air Force Unit Post Office
Los Angeles, California 90045

ACLIT-9663
Maxwell AFB, Alabama 36112

AFSTC Technical Library
(ETV,MU-135)
Patrick AFB,Florida 32925

AHSC (AHSPS-12)
Eglin AFB, Florida 32542

Mr B.R. Locke
Technical Adviser, Requirements
USAF Security Service
Kelly Air Force Base, Texas 78241

Hq AMD (AMR)
Brooks AFB, Texas 78235

USAFSAM (SMKOR)
Brooks AFB, Texas 78235

Commanding General
Attn: STEWS-RE-L, Technical Library
White Sands Missile Range
New Mexico 88002 (2 copies)

Hq AEDC (AETS)
Attn: Library/Documents
Arnold AFS, Tennessee 37389

European Office of Aerospace Research
APO New York 09667

Physical & Engineering Sciences Division
U.S. Army Research Office
3045 Columbia Pike
Arlington, Virginia 22204

Commanding General
U.S. Army Security Agency
Attn: IARD-T
Arlington Hall Station
Arlington, Virginia 22212

Commanding General
U.S. Army Materiel Command
Attn: AMCRD-TP
Washington, D.C. 20315

Technical Director (SMUFA-A2600-107-1)
Frankford Arsenal
Philadelphia, Pennsylvania 19137

Redstone Scientific Information Center
Attn: Chief, Document Section
U.S. Army Missile Command
Redstone Arsenal, Alabama 35809

Commanding General
U.S. Army Missile Command
Attn: AMSMI-REX
Redstone Arsenal, Alabama 35809

Commanding General
U.S. Army Strategic Communications Command
Attn: SCC-CG-SAE
Fort Huachuca, Arizona 85613

Commanding Officer
Army Materials and Mechanics Res. Center
Attn: Dr H. Priest
Watertown Arsenal
Watertown, Massachusetts 02172

Commandant
U.S. Army Air Defense School
Attn: Missile Science Division, C&S Dept
P.O. Box 9390
Fort Bliss, Texas 79916

Commandant
U.S. Army Command & General Staff College
Attn: Acquisitions, Library Division
Fort Leavenworth, Kansas 66027

Commanding Officer
U.S. Army Electronics R&D Activity
White Sands Missile Range, New Mexico 88002

Mr Norman J. Field, AMSEL-RD-S
Chief, Office of Science & Technology
Research and Development Directorate
U.S. Army Electronics Command
Fort Monmouth, New Jersey 07703

Commanding Officer
Harry Diamond Laboratories
Attn: Dr Berthold Altman (AMXDO-TI)
Connecticut Avenue and Van Ness St N.W.
Washington, D.C. 20438

Director
Walter Reed Army Institute of Research
Walter Reed Army Medical Center
Washington, D.C. 20012

Commanding Officer (AMXRD-BAT)
U.S. Army Ballistics Research Laboratory
Aberdeen Proving Ground
Aberdeen, Maryland 21005

Technical Director
U.S. Army Limited War Laboratory
Aberdeen Proving Ground
Aberdeen, Maryland 21005

Commanding Officer
Human Engineering Laboratories
Aberdeen Proving Ground
Aberdeen, Maryland 21005

U.S. Army Munitions Command
Attn: Science & Technology Br. Bldg 59
Picatinny Arsenal, SMUFA-VA6
Dover, New Jersey 07801

U.S. Army Mobility Equipment Research
and Development Center
Attn: Technical Document Center, Bldg 315
Fort Belvoir, Virginia 22060

Director
U.S. Army Engineer Geodesy,
Intelligence & Mapping
Research and Development Agency
Fort Belvoir, Virginia 22060

Dr Herman Robl
Deputy Chief Scientist
U.S. Army Research Office (Durham)
Box CM, Duke Station
Durham, North Carolina 27706

Richard O. Ulsh (CRDARD-IPO)
U.S. Army Research Office (Durham)
Box CM, Duke Station
Durham, North Carolina 27706

Mr Robert O. Parker, AMSEL-RD-S
Executive Secretary, JSTAC
U.S. Army Electronics Command
Fort Monmouth, New Jersey 07703

Commanding General
U.S. Army Electronics Command
Fort Monmouth, New Jersey 07703
Attention: AMSEL-SC
RD-GF
RD-MI
XL-D
XL-E
XL-C
XL-S (Dr R. Buser)
HL-CT-DD
HL-CT-R
HL-CT-L (Dr W.S. McAfee)
HL-CT-O
HL-CT-I
HL-CT-A
SL-D
NL-A
NL-P
NL-P-2 (Mr D. Haratz)
NL-R (Mr R. Kulinyi)
NL-S
EL-D
KL-E
KL-S (Dr H. Jacobs)
KL-SM (Drs Schiel/Hieslmair)
KL-T
VL-D
VL-F (Mr R.J. Hieronymi)
WL-D
(1 copy to each symbol listed individually addressed)

Dr A.D. Schnitzler, AMSEL-NL-NVOI
Night Vision Laboratory, USAECOM
Fort Belvoir, Virginia 22060

Dr G.M. Janney, AMSEL-NL-NVOR
Night Vison Laboratory, USAECOM
Fort Belvoir, Virginia 22060

Atmospheric Sciences Office
Atmospheric Sciences Laboratory
White Sands Missile Range
New Mexico 88002

Missile Electronic Warfare,
Technical Area, AMSEL-WT-MI
White Sands Missile Range
New Mexico 88002

Project Manager
Common Positioning & Navigation Systems
Attn: Harold M. Bahr (AMCPM-NS-TM), Bldg 439
U.S. Army Electronics Command
Fort Monmouth, New Jersey 07703

Director, Electronic Program
Attn: Code 427
Department of the Navy
Washington, D.C. 20360

Commander
U.S. Naval Security Group Command
Attn: G43
3801 Nebraska Avenue
Washington, D.C. 20390

Director
Naval Research Laboratory
Washington, D.C. 20390
Attn: Code 2027 6 copies
Dr W.C. Hall, Code 7000 1 copy
Dr A. Brodzinsky, Sup. Elec Div. 1 copy

Dr G.M.R. Winkler
Director, Time Service Division
U.S. Naval Observatory
Washington, D.C. 20390

Naval Air Systems Command
AIR 03
Washington, D.C. 20360 2 copies

Naval Ship Systems Command
Ship 031
Washington, D.C. 20360

Naval Ship Systems Command
Ship 035
Washington, D.C. 20360

U.S. Naval Weapons Laboratory
Dahlgren, Virginia 22448

Naval Electronic Systems Command
ELEX 03, Room 2046 Munitions Building
Department of the Navy
Washington, D.C. 20360 (2 copies)

Commander
Naval Electronics Laboratory Center
Attn: Library
San Diego, California 92152 (2 copies)

Deputy Director and Chief Scientist
Office of Naval Research Branch Office
1030 East Green Street
Pasadena, California 91101

Library (Code2124)
Technical Report Section
Naval Postgraduate School
Monterey, California 93940

Glen A. Myers (Code 52Mv)
Assoc Professor of Elec. Engineering
Naval Postgraduate School
Monterey, California 93940

Commanding Officer and Director
U.S. Naval Underwater Sound Laboratory
Fort Trumbull
New London, Connecticut 06840

Commanding Officer
Naval Avionics Facility
Indianapolis, Indiana 46241

Dr H. Harrison, Code RRE
Chief, Electrophysics Branch
National Aeronautics & Space Admin.
Washington, D.C. 20546

NASA Lewis Research Center
Attn: Library
21000 Brookpark Road
Cleveland, Ohio 44135

Los Alamos Scientific Laboratory
Attn: Report Library
P.O. Box 1663
Los Alamos, New Mexico 87544

Federal Aviation Administration
Attn: Admin Stds Div (MS-110)
800 Independence Ave S.W.
Washington, D.C. 20590

Head, Technical Services Division
Naval Investigative Service Headquarters
4420 North Fairfax Drive
Arlington, Virginia 22203

Commander
U.S. Naval Ordnance Laboratory
Attn: Librarian
White Oak, Maryland 21502 (2 copies)

Commanding Officer
Office of Naval Research Branch Office
Box 39 FPO
New York, New York 09510

Commanding Officer
Office of Naval Research Branch Office
219 South Dearborn Street
Chicago, Illinois 60604

Commanding Officer
Office of Naval Research Branch Office
495 Summer Street
Boston, Massachusetts 02210

Commander (AEL)
Naval Air Development Center
Johnsville, Warminster, Pa 18974

Commanding Officer
Naval Training Device Center
Orlando, Florida 32813

Commander (Code 753)
Naval Weapons Center
Attn: Technical Library
China Lake, California 93555

Commanding Officer
Naval Weapons Center
Corona Laboratories
Attn: Library
Corona, California 91720

Commander, U.S. Naval Missile Center
Point Mugu, California 93041

W.A. Eberspacher, Associate Head
Systems Integration Division
Code 5340A, Box 15
U.S. Naval Missile Center
Point Mugu, California 93041

Mr M. Zane Thornton, Chief
Network Engineering, Communications
and Operations Branch
Lister Hill National Center for
Biomedical Communications
8600 Rockville Pike
Bethesda, Maryland 20014

U.S. Post Office Department
Library - Room 1012
12th & Pennsylvania Ave, N.W.
Washington, D.C. 20260

Director
Research Laboratory of Electronics
Massachusetts Institute of Technology
Cambridge, Massachusetts 02139

Mr Jerome Fox, Research Coordinator
Polytechnic Institute of Brooklyn
35 Johnson Street
Brooklyn, New York 11201

Director
Columbia Radiation Laboratory
Columbia University
538 West 120th Street
New York, New York 10027

Director
Coordinated Science Laboratory
University of Illinois
Urbana, Illinois 61801

Director
Stanford Electronics Laboratories
Stanford University
Stanford, California 94305

Director
Microwave Physics Laboratory
Stanford University
Stanford, California 94305

Director, Electronics Research Laboratory
University of California
Berkeley, California 94720

Director
Electronic Sciences Laboratory
University of Southern California
Los Angeles, California 90007

Director
Electronics Research Center
The University of Texas at Austin
Austin Texas 78712

Division of Engineering and Applied Physics
210 Pierce Hall
Harvard University
Cambridge, Massachusetts 02138

Dr G.J. Murphy
The Technological Institute
Northwestern University
Evanston, Illinois 60201

Dr John C. Hancock, Head
School of Electrical Engineering
Purdue University
Lafayette, Indiana 47907

Dept of Electrical Engineering
Texas Technological College
Lubbock, Texas 79409

Aerospace Corporation
P.O. Box 95085
Los Angeles, California 90045
Attn: Library Acquisitions Group

Professor Nicholas George
California Inst of Technology
Pasadena, California 91109

Aeronautics Library
Graduat Aeronautical Laboratories
California Institute of Technology
1201 E. California Blvd
Pasadena, California 91109

The John Hopkins University
Applied Physics Laboratory
Attn: Document Librarian
8621 Georgia Avenue
Silver Spring, Maryland 20910

Raytheon Company
Attn: Librarian
Bedford, Massachusetts 01730

Raytheon Company
Research Division Library
28 Seyon Street
Waltham, Massachusetts 02154

Dr Sheldon J. Wells
Electronic Properties Information Center
Mail Station E-175
Hughes Aircraft Company
Culver City, California 90230

Dr Robert E. Fontana
Systems Research Laboratories Inc.
7001 Indian Ripple Road
Dayton, Ohio 45440

Nuclear Instrumentation Group
Bldg 29, Room 101
Lawrence Radiation Laboratory
University of California
Berkeley, California 94720

Sylvania Electronic Systems
Applied Research Laboratory
Attn: Documents Librarian
40 Sylvan Road
Waltham, Massachusetts 02154

Hollander Associates
P.O. Box 2276
Fullerton, California 92633

Illinois Institute of Technology
Dept of Electrical Engineering
Chicago, Illinois 60616

The University of Arizona
Dept of Electrical Engineering
Tucson, Arizona 85721

Utah State University
Dept Of Electrical Engineering
Logan, Utah 84321

Case Institute of Technology
Engineering Division
University Circle
Cleveland, Ohio 44106

Hunt Library
Carnegie-Mellon University
Schenley Park
Pittsburgh, Pennsylvania 15213

Dr Leo Young
Stanford Research Institute
Menlo Park, California 94025

School of Engineering Sciences
Arizona State University
Tempe, Arizona 85281

Engineering & Mathematical Sciences Library
University of California at Los Angeles
405 Hilgred Avenue
Los Angeles, California 90024

The Library
Government Publications Section
University of California
Santa Barbara, California 93106

Carnegie Institute of Technology
Electrical Engineering Department
Pittsburgh, Pennsylvania 15213

Professor Joseph E. Rowe
Chairman, Dept of Electrical Engineering
The University of Michigan
Ann Arbor, Michigan 48104

New York University
College of Engineering
New York, New York 10019

Syracuse University
Dept of Electrical Engineering
Syracuse, New York 13210

Yale University
Engineering Department
New Haven, Connecticut 06520

Airborne Instruments Laboratory
Deerpark, New York 11729

Raytheon Company
Attn: Librarian
Bedford, Massachusetts 01730

Lincoln Laboratory
Massachusetts Institute of Technology
Lexington, Massachusetts 02173

The University of Iowa
The University Libraries
Iowa City, Iowa 52240

Lenkurt Electric Co,Inc
1105 County Road
San Carlos, California 94070
Attn: Mr E.K. Peterson

Philco Ford Corporation
Communications & Electronics Div.
Union Meeting and Jolly Rods
Blue Bell, Pennsylvania 19422

Union Carbide Corporation
Electronic Division
P.O. Box 1209
Mountain View, California 94041

Electromagnetic Compatibility Analysis Center
(ECAC), Attn: ACLP
North Severn
Annapolis, Maryland 21402

Director
U. S. Army Advanced Materiel Concepts Agency
Washington, D.C. 20315

ADDENDUM

Dept of Electrical Engineering
Rice University
Houston, Texas 77001

Research Laboratories for the Eng Sc.
School of Engineering & Applied Science
University of Virginia
Charlottesville, Virginia 22903

Dept of Electrical Engineering
College of Engineering & Technology
Ohio University
Athens, Ohio 45701

Project Mac
Document Room
Massachusetts Institute of Technology
545 Technology Square
Cambridge, Massachusetts 02139

Lehigh University
Dept of Electrical Engineering
Bethelem, Pennsylvania 18015

Commander Test Command (TCDT-)
Defense Atomic Support Agency
Sandia Base
Albuquerque, New Mexico 87115

Materials Center Reading Room 13-2137
Massachusetts Institute of Technology
Cambridge, Massachusetts 02139

Professor James A. Cadzow
Department of Electrical Engineering
State University of New York at Buffalo
Buffalo, New York 14214

ERRATUM

Mr Jerome Fox, Research Coordinator
Polytechnic Institute of Brooklyn
55 Johnson St (Shouldbe 333 Jay St)
Brooklyn, N.Y. 11201

OMIT

Mr Morton M. Pavane, Chief
AFSC Scientific & Tech. Liaison Office
26 Federal Plaza, Suite 1313
New York, New York 10007

Commanding Officer
Office of Naval Research Branch Office
Box 39 FPO
New York, N.Y. 09510

Security Classification

DOCUMENT CONTROL DATA - R & D

(Security classification of title, body of abstract and indexing annotation must be entered when the overall report is classified)

ORIGINATING ACTIVITY (Corporate author)	2a. REPORT SECURITY CLASSIFICATION
University of Illinois Coordinated Science Laboratory Urbana, Illinois 61801	Unclassified
	2b. GROUP

3. REPORT TITLE

A STUDY OF EFFECTS OF THE GAS-SURFACE INTERACTION ON SPINNING CONVEX BODIES WITH APPLICATION TO SATELLITE EXPERIMENTS

4. DESCRIPTIVE NOTES *(Type of report and inclusive dates)*

5. AUTHOR(S) *(First name, middle initial, last name)*

KARR, Gerald Ray

6. REPORT DATE	7a. TOTAL NO. OF PAGES	7b. NO. OF REFS
September, 1969	153	34

8a. CONTRACT OR GRANT NO.	9a. ORIGINATOR'S REPORT NUMBER(S)
DAAB 07-67-C-0199; also in part NAS 8-21442. b. PROJECT NO.	R-435
c.	9b. OTHER REPORT NO(S) *(Any other numbers that may be assigned this report)*
d.	

10. DISTRIBUTION STATEMENT

This document has been approved for public release and sale; its distribution is unlimited.

11. SUPPLEMENTARY NOTES	12. SPONSORING MILITARY ACTIVITY
	Joint Services Electronics Program thru U.S. Army Electronics Command Fort Monmouth, New Jersey 07703

13. ABSTRACT

In rarefied gas flow problems there are two effects which influence the flow; (1) collisions of gas molecules with other gas molecules, and (2) collisions of gas molecules with solid surfaces (the gas-surface interaction). This study deals with free molecular flow in which the effect of gas-gas collision can be neglected and the gas-surface interaction has the dominate influence on the flow. The results of this study have application to satellites since free molecular flow conditions occur at orbital altitudes above 120km.

Knowledge of the gas-surface interaction is required in order to determine the aerodynamic properties of satellites. At satellite velocities (7-8km/sec) the interaction of neutral atmospheric gas molecules with the satellite surface occurs at energies in the 1 to 10 ev range. It is just this energy range which has not been satisfactorily duplicated in the laboratory; therefore, at present, laboratory gas-surface interaction data can not be applied directly to the determination of the aerodynamics properties of satellites. It is proposed in this study that satellite experiments be performed to obtain the needed information from measurements of the aerodynamics properties of satellites. In order to interpret the satellite data, a generalized gas-surface interaction model was developed and used in the analysis of this study.

DD FORM 1 NOV 65 1473

Security Classification

14 KEY WORDS	LINK A		LINK B		LINK
	ROLE	WT	ROLE	WT	ROLE
Gas-Surface Interaction					
Aerodynamic Properties					
Free-Molecular Flow					
Spinning Bodies					
Convex Bodies					
Satellites					
Satellite Experiments					
Random Tumbling					
Aerodynamic Torque					
Aerodynamic Lift					
Aerodynamic Drag					
Orbital Gas Density					
Gas-Surface Interaction Models					